THÈSE

Présentée pour obtenir le grade de

DOCTEUR DE L'ECOLE POLYTECHNIQUE

Spécialité : Physique.

Roelene BOTHA

Deposition of thin films in a high-density low-pressure plasma system: the influence of the SiH_4 injection on the deposition kinetics and material properties of SiO_2

Dépôt de couches minces par plasma haute densité à basse pression : influence de l'injection de silane sur la cinétique du dépôt et les propriétés de la silice.

T. BELMONTE	**Rapporteur**
P. BERGONZO	
P. BULKIN	**Co-directeur**
B. DRÉVILLON	**Président, directeur de thèse**
J. PELLETIER	
Y. SÉGUI	**Rapporteur**

LABORATOIRE DE PHYSIQUE DES INTERFACES ET COUCHES MINCES, CNRS UMR 7647
ÉCOLE POLYTECHNIQUE

Acknowledgements

I would like to thank the following people, without whom this work would not have been possible:

Prof. Bernard Drévillon, for the opportunity to do my PhD under his supervision.
Pavel Bulkin, the co-supervisor of my PhD, for his enthusiastic guidance and advice during every step of the project.
Tatiana Novikova, for adapting the DSMC code to the reactor chamber's dimensions and her patient explanations when I went off track.
Bicher Haj Ibrahim, the previous PhD student working on Venus, for instructing me how to operate the system and always being there to offer good advice.
Dmitri Daineka, for preparing the samples for the electrical measurements.
Jacqueline Samson and *Sanjay Ram,* for their friendly assistance with the AFM measurements.
Shaïma Enouz for the TEM images.
Eric Johnson, for etching a series of deposited samples.
Marc Chatelet, Jean Eric Bourée, Laurent Philippe and *Nans Pham,* for their help in correcting the French of my presentation.
Laurence Corbel and *Chantal Geneste*, who always made time to help with any administrative problems.
Claude Hamel-Guigues (from LOB) for her assistance with the transmission measurements.
Christian Longeaud (from LGEP) for the usage of their FTIR spectrometer.
Garry Rose Kitchner, *Frédéric Liège* and *Eric Paillassa* for ensuring that things always run smoothly.
A special thanks to all my other colleagues in the LPICM that made it a great place to work: *Alexei Abramov, Dmitry Aldakov, Pierre-Jean Alet, Makrina Anastasiadou, Maria-Rosaria Antonelli, Laurent Baraton, Sami Ben-Hatit, Céline Bernon, Yvan Bonnassieux, Quentin Brulin, Jérôme Charliac, Antonello De Martino, Yassine Djeridane, Gregoriy Dolgonos, Enric Garcia-Caurel, Olivier Godde, Cyril Jadaud, Laurent Kroely, Martin Labrune, Marc Lamy de la Chapelle, Gowtham Manoharan, Bernd Marquardt, Oumkelthoum Mint Moustapha, Jean-Luc Moncel, Mario Moreno Moreno, Tran Thuat Nguyen, Razvan Negru, Razvigor Ossikovski, Maher Oudwan, Jean-Yves Parey, Gennaro Picardi, Didier Pribat, Patricia Prodhomme, Pere Roca I Cabarrocas, Antoine Salomon, Ingrid Stenger, Denis Tondelier, Holger Vach, Hiroshi Yano, Linwei Yu.*

Introduction

1. Overview

Silicon oxides, nitrides and oxynitrides are used in a variety of applications, such as optical, protective, corrosion resistant and passivation layers, diffusion barriers, coatings for photovoltaic applications and most importantly, dielectric (isolating) thin films. While SiO_2 remains the pillar of optical and electronic technology as the main material for optical fibers, filters and gate and interlayer dielectric in ultra-large scale integration (ULSI) circuits, the search for materials that have higher or lower dielectric constants, better chemical stability and hardness continues[1,2]. Silicon oxide and nitride films and multi-layers of these materials have also received a lot of attention recently as transparent encapsulating films to improve the barrier properties of various polymers against water and gas permeation [3-6].

For the manufacturing of dielectric, optical, functional and protective thin films and especially for roll-to-roll applications, there is an increasing demand for high rate low-temperature deposition technology. Planar optical waveguides or scratch resistant coatings require growth rates exceeding 10 nm per second, for example [7]. These thin films can be deposited by almost all coating techniques currently in use, such as: Thermal and e-beam evaporation, triode and magnetron sputtering, ion plating and ion beam sputtering and Chemical Vapour Deposition (CVD) techniques such as atmospheric pressure CVD (APCVD), Low Pressure CVD (LPCVD) and Plasma Enhanced CVD (PECVD) including Radio Frequency, Dual frequency and Electron Cyclotron Resonance (ECR) PECVD, though not all of these techniques are capable of providing the required deposition rates [8-10]. The

latter is a microwave-based PECVD technique operating at low pressures, which forms part of the group of the so-called High Density Plasma (HDP) techniques.

Regardless of the plasma conditions, silica films will all have an amorphous structure with an oxygen atom to silicon atom ratio close to 2. The quality of the film material does however differ between the different deposition techniques in terms of hydroxyl (OH) content in the film and void fraction (density) which in turn influence the optical, electrical and mechanical properties of the films[11,12]. The density (2.27 g·cm^{-3}), refractive index (1.457 at 2 eV) and p-etch rate (1.5 Å/s) of thermal silica [13,14] can be used as benchmarks for assessing the quality of silicon oxide films manufactured using other CVD techniques. Table 1 contains a summary of some material properties of silicon dioxide films fabricated using different CVD techniques [12,15-18].

Film parameter	APCVD	PECVD	Dual frequency PECVD	HDP (ECR-PECVD)
Refractive index	1.45	1.45-1.46	1.45-1.46	1.46
Hydrogen content Form	1-2 % Si-H	1-2% Si-H	1% Si-H	<1% Si-OH
Dielectric Strength (MV/cm)	6-7	6-7	6-7	11

Table 1. Properties of SiO_2 films deposited using different CVD techniques.

Silicon dioxide films deposited using various PECVD techniques have been studied extensively during the last two decades. This research has made significant contributions to the fundamental understanding of the deposition processes in different PECVD systems [19-28]. In general, HDP techniques are

able to provide higher quality thin film materials than their counterparts which operate at higher pressure. This is in part due to the possibility of de-coupling the creation and sustaining of the plasma from the control over the ion flux onto the substrate, and secondly in part due to changes in the plasma chemistry. The higher plasma density and lower pressure leads to a non-collisional sheath with a reduced width and a larger flux of ions of which the energy can be controlled, that facilitate the removal of reaction byproducts from the surface [8, 9]. The use of low pressure also increases the mean free path and suppresses most of the secondary volume reactions [11, 29]. In addition to this, an increased ion bombardment in HDP systems can be achieved by applying an RF bias to the substrate holder. As the electrons in the plasma have a higher mobility than the ions, a negative potential (DC self-bias) will form at the sample surface with respect to the plasma potential and result in a greater flux of positive ions onto it[30]. This ensures excellent step coverage of highly complex surface structures due to the partial re-sputtering of the film. This will both lead to densification of the film [13,14,16] and also assists in the removal of reaction by-products, for example hydroxyl groups that affect the optical properties of the materials [31, 32].

HDP systems have become increasingly popular in the micro electronics industry, due to the high quality of the films deposited at moderate and low wafer temperatures [33, 19]. They are however expensive and have a high cost of ownership, due to the expensive high-throughput pumping system. Increasing the process uniformity over larger surfaces is considered a crucial issue in HDP systems [34]. The possibility of very high deposition rates could however make HDP systems a competitive technology for “low-tech” coating applications, if the pumping requirements can be reduced [35] or the throughput can be substantially increased. Additional studies are however required in order to clarify the

mechanisms responsible for the decrease in the quality of the films that is in general observed when the process is done at high deposition rates, and to obtain a clear understanding of the influence the process conditions have on the material properties. The industrial objective is clearly to deposit the highest quality silica layer at the highest possible deposition rate, while avoiding damaging any structures that are already present on the substrate. The majority of academic studies however make use of noble gas diluted SiH_4 precursors injected through a gas ring. This dilution, that in some cases is as low as 0.1 percent, has an adverse effect on the deposition rate.

In order to explain this statement, the deposition of a silica layer from an undiluted SiH_4 and O_2 gas mixture can be considered [36]. For a 1 cm^2 surface with a deposition rate of 10 nm/sec the necessary minimal silane and oxygen flow rates are 0.057 sccm and 0.114 sccm respectively. This assumes that all the precursors are consumed during the deposition, by the balanced reaction:

$$SiH_4(g) + 2O_2(g) \rightarrow SiO_2(s) + 2H_2O(g).$$

For a 300 mm diameter wafer, these flows scale to 42 sccm and 84 sccm respectively. At an operating pressure of 2 mTorr, which is typical for the HDP system used in this study, a pumping speed at the substrate plane of 800 l/s will be needed. Taking into account that the precursors are not entirely consumed and that deposition may take place on all surfaces in the system, it is clear that the required pumping speed is in fact much higher. Add to this the effect of diluting the silane in a noble gas and the required pumping system will be entirely unrealistic. All of this places an extreme importance on the choice of the precursor gases and the silane injection system's design [1,37-39].

A large amount of work has been done in recent years to understand the complex nature of HDP CVD processes. The correct comparison and interpretation of data is however complicated, if not made entirely impossible, by differences in either the deposition systems themselves or the deposition conditions used. In addition to this, descriptions of specific installations and their designs are mostly withheld due to intellectual property (IP) issues. For the same reason, research done inside companies is frequently not fully reported. Moreover, industrial systems are usually not designed with the same objectives in mind as experimental setups in research laboratories, and do not allow the use of complex diagnostic equipment in the best configurations possible. Research consequently needs to be done not only in system conditions ideally adapted to the diagnostic techniques, but also in conditions appropriate to industrial applications, for both the process and reactor configuration.

Comparisons of the gas flow simulations of the precursor injection with experimental deposition thickness profiles also offer a method to improve the precursor distribution and consumption at the substrate level. The modeling of HDP systems have usually considered them to be well-mixed, assuming that the gas composition is uniform across the system due to the low pressures used and the resulting large mean free path of the species [40,41]. The precursor consumption at the substrate level and on the walls are sometimes neglected [42]. Other studies have concentrated on radical and ion densities, neglecting the directionality of the primary precursor injection [43-45]. Thus far, there have been only a few studies that have taken into account the effect of the real geometry of the high density plasma vessel and the injection of the precursor [42,44,46]. Due to the low pressures used in HDP systems, the local characteristic dimensions of the reactors are mostly smaller than the mean free path of the precursor gas and

areas with sharp density gradients exist near the gas injection points. Continuum models* are not entirely applicable in these cases as the Knudsen† number approaches unity, though they do sometimes provide meaningful results. A statistical method is consequently the technique the best adapted to simulate these systems.

The Direct Simulation Monte Carlo (DSMC) method [47] can be used if a system falls in the transition flow regime, defined as having a Knudsen number between 0.1 and 10. This method allows one to simulate dilute gases using a probabilistic approach [48], by tracking a number of statistically representative particles. It has proven very interesting for investigating free jets injecting gas into vacuum [49, 50] or to study the precursor flow from a showerhead injection system into a portion of the reactor over a wide range of Knudsen numbers [51] and has found good accuracy when compared to experimental results [52].

* Which model gas flows at the macroscopic level and make use of the Navier-Stokes equations.
† The Knudsen number is a dimensionless number defined as the ratio of the molecular mean free path λ, to a physical length scale L, representative of the system. Dimensions of local features are sometimes taken as the value L to calculate the local Knudsen number.

2. Research objectives

The primary goal of this project is to couple research on large area plasma sources and the physics and chemistry of the plasma and the material properties, to ensure a better understanding of the oxygen and silane deposition plasma, and especially the role of water in the deposition process. The gas phase composition in a High Density Plasma (HDP) source is investigated using Optical Emission Spectroscopy (OES) and differentially pumped Quadrupole Mass Spectrometry (QMS). Films are investigated using phase modulated spectroscopic ellipsometry, Fourier Transform Infrared (FTIR) spectroscopy, transmission spectroscopy and electrical measurements in order to characterize them in terms of deposition rate, refractive index, hydroxyl content and breakdown voltage.

The obtained OES and QMS results are then compared with each other, as well as with the FTIR and SE results in order to validate the experimental findings, to increase the understanding of the relationship between the deposition rate, layer properties and the plasma conditions and to ultimately optimize the deposition process. Though the primary focus of the study is silicon oxide, silicon nitride and oxynitride are also studied. Silicon oxide and nitride films used as water barrier coatings for polyethylene terephthalate (PET) are also investigated.

In order to study and improve the precursor's consumption at the substrate level, various sets of experiments are performed. The precursor delivery to the substrate surface for the deposition of SiO_2 is investigated for both the SiH_4 and

O_2 precursors. In order to remove any possible ambiguity about the uniformity of the plasma and the active oxygen flux onto the surface, the ashing of photoresist in a pure oxygen plasma is studied over a broad range of plasma conditions and thus the uniformity of the ion and radical flux onto the substrate surface is verified. The positioning and design of the silane gas injection system are investigated using a capillary jet injection system and a uniform gas injection ring. The influence the precursor delivery to the substrate surface has on the deposition rate and material properties of silicon oxide films, with special emphasis placed on the Si-OH content, is then studied experimentally. These results are then used to prove that HDP systems can not be considered as well mixed reactors, as the growth is highly dependant on the positioning of the injection point and the direction of the primary precursor flux.

In order to gain further insight into how the precursor utilization at the substrate level can be improved and what the fluxes towards the substrate surface consist of, a Direct Simulation Monte Carlo (DSMC) method is employed to calculate the flux of precursors onto the substrate plane. These results are then compared to the experimental results to verify the physical model presented for the deposition process.

3. Structure of the thesis

The thesis is organized as follows:

Chapter I will give an overview of PECVD systems currently in use, before focusing on the advantages and different types of HDP systems. The MDECR-PECVD reactor used during this thesis, *Venus*, is also presented. The various film characterization techniques employed during the course of the thesis will also be reviewed. The influence of various process parameters, such as the microwave power, RF substrate bias, gas flows and pressure, on the plasma and material properties in a Matrix Distributed ECR-PECVD system are investigated in Chapter II. The study of the gas injection in the MDECR-PECVD system, for both pure oxygen plasmas as well as deposition plasmas containing silane/oxygen gas mixtures are presented in Chapter III. The hydroxyl content of silicon oxide films deposited using the different injection systems and process parameters are also presented in this chapter. Chapter IV starts by giving an overview of the Direct Simulation Monte-Carlo method used to simulate the flux of precursors onto the substrate surface. The modeled structures and simulation parameters are then presented, followed by the obtained results. Chapter V recapitulates what has been accomplished in the thesis and correlates it with the set research objectives. The chapter concludes with some recommendations for future work and improvements.

For the purpose of being unambiguous and concise, the author has placed any further information she considers relevant to the study in the appendices.

References

[1] T.P. Ma, IEEE Trans. Electron Devices, 45 (1998) 680.

[2] M.H. Francombe, Ed., *Handbook of Thin Film Devices Volume 1: Heterostructures for High Performance Devices*, Academic, San Diego, CA, (2000).

[3] J. Ubrig, S. Martin, S. Cros, J.-E. Bourée, J. Physics : Conf. Series, 100 (2008) 082030.

[4] D.G. Howells, B.M. Henry, Y. Leterrier, J._A.E. Manson, J. Madocks, H.E. Assender, Surf. Coat. Technol., 202 (2008) 3529.

[5] M. Deilmann, H. Halfmann, N. Bibinov, P. Awakowicz, Surf. Coat. Technol., 202 (2008) 1911.

[6] Bieder, A. Gruniger, Ph. Rudolf von Rohr, Surf. Coat. Technol., 200 (2005) 928.

[7] T. Schmauder, K.-D. Nauenburg, K. Kruse, G. Ickes, Thin Solid Films, 502 (2006) 270.

[8] L. Martinu, D. Poitras, J. Vac. Sci. Technol. A, 18 (2000) 2619.

[9] A.J. Flewitt, A.P. Dyson, J. Robertson, W.I. Milne, Thin Solid Films, 383 (2001) 172.

[10] G.I. Isai, J. Holleman, H. Wallinga, P.H. Woerlee, J. Electrochem. Soc., 151 (2004) C649.

[11] A. Granier, *Deposition of thin films by PECVD*, CIP'2007 Short courses, 16th international colloquium on plasma processes, Toulouse, France (2007).

[12] J. Foggiato, *Chemical Vapor Deposition of Silicon Dioxide Films, Chapter 3 of the Handbook of thin film deposition techniques: principles, methods, equipment and applications*, second edition, edited by Krishna Seshan, William Andrew Inc., Austin (2002).

[13] K. L. Seaward, J.E. Turner, K. Nauka, A.M.E. Nel, J. Vac. Sci. Technol. B, 13 (1995) 118.

[14] D. Goghero, A. Goullet, G. Borvon, G. Turban, Thin Solid Films, 471 (2005) 123.

[15] J.A. Dobrowolski, *Optical properties of films and coatings, in Handbook of Optics, Vol. I*, Edited by M. Bass, E. W. van Stryland, D. R. Williams, and W. L. Wolfe, McGraw-Hill, New York (1995).

[16] M. Ohring, *Materials science of thin films: Deposition and structure, second edition*, Elsevier Academic Press, Hoboken, New Jersey (2002) 337.

[17] F. Plais, B. Aguis, F. Abel, J. Siejka, Puech, G. Ravel, P. Alnot, N. Proust, J. Electrochem. Soc., 139 (1992) 1492.

[18] A.Y. Kovalgin, G. Isai, J. Holleman, J. Schmitz, J. Electrochem. Soc., 155 (2008) G21.

[19] S.V. Nguyen, IBM J. Res. Develop., 43 (1999) 109.

[20] G. Lucovsky, P.D. Richard, D.V. Tsu, S.Y. Lin, R.J. Markunas, J. Vac. Sci. Technol. A, 4 (1986) 681.

[21] G. Lucovsky, D.V. Tsu, J. Vac. Sci. Technol. A, 5 (1987) 2231.

[22] S.M. Han, E.S. Aydil, J. Vac. Sci. Technol. A, 14 (1996) 2062.

[23] S.M. Han, E.S. Audil, J. Electrochem. Soc., 144 (1997) 3963.

[24] S.M. Han, E.S. Aydil, Thin Solid Films, 290-291 (1996) 427.

[25] S.P. Shufflebotham, M. Weise, D. Pirkle, D. Denison, Materials Sci. Forum, 140-142 (1993) 255.

[26] S.E. Lassig, J.D. Tucker, Microelectr. J., 26 (1995) xi.

[27] N. Jiang, M.-C. Hugon, B. Aguis, T. Kretz, F. Plais, D. Pribat, T. Carriere, M. Puech, Jpn. J. Appl. Phys., 31 (1992) L1404.

[28] S. Matsuo, M. Kiuchi, Jpn. J. Appl. Phys. 22 (1983) L210.

[29] S. T. Picraux, E. Chason, T. M. Mayer, MRS Bulletin, XVII (June, 1992) 52.

[30] N Jiang, B. Aguis, M.C. Hugon, J. Olivier, M. Puech, Journal of Applied Physics, 76 (1994) 1847.

[31] S.A. Moshkalyov, J.A. Diniz, J.W. Swart, P.J. Tatsch, M. Machida, J. Vac. Sci. Technol. B, 15 (1997) 2682.

[32] B.S. Sahu, O.P. Agnihotri, S.C. Jain, R. Mertens, I. Kato, Semicond. Sci.Technol., 15 (2000) L11.

[33] O. Humbach, H. Fabian, U. Grzesik, U. Haken, W. Heitmann, J. Non-Cryst. Solids, 203 (1996) 19.

[34] A. Bogaerts, E. Neyts, R. Gijbels, J. van der Mullen, Spectrochimica Acta Part B 57 (2002) 609.

[35] M.A. Lieberman, A.J. Lichtenberg, *Principles of Plasma Discharges and Materials Processing second edition*, John Wiley & Sons Inc., Hoboken, New Jersey (2005) 20.

[36] R. Botha, B. Haj Ibrahim, P. Bulkin, B. Drévillon, J. Vac. Sci. Technol. A, 26 (2008) 1115.

[37] J.A. Theil, J. Vac. Sci. Technol. A, 13 (1995) 442.

[38] T.C. Paulick, J. Vac. Sci. Technol. A, 21 (1982) 1032.

[39] A.Y. Kovalgin, G.I. Isai, J. Holleman, J. Schmitz, J. Electrochem. Soc., 155 (2008) G21.

[40] E. Meeks, R.S. Larson, P. Ho, C. Apblett, S.M. Han E. Edelberg, E.S. Aydil, J. Vac. Sci. Technol. A, 16 (1998) 544.

[41] A.Y. Kovalgin, A. Boogaard, I. Brunets, J. Holleman, J. Schmitz, Surf. Coat. Technol., 201 (2007) 8849.

[42] L.A. Gochberg, R.L. Kinder, *Low Pressure Deposition in a High Density Plasma CVD reactor*, Rarefied Gas Dynamics: 25th International Symposium, ed. M.S. Ivanov and A.K. Rebrov, Novosibirsk (2007) 1029.

[43] T. Kim, S.-M. Suh, S.L. Girshick, M.R. Zachariah, P.H. McMurry, R.M. Rassel, Z. Shen, S.A. Campbell, J. Vac. Sci. Technol. A, 20 (2002) 413.

[44] K. Takechi, S. Otsuki, IEEE Trans. Semicond. Manufact., 19 (2006) 286.

[45] S.-M. Suh, .R. Zachariah, S.L. Girshick, J. Vac. Sci. Technol. A, 19 (2001) 940.

[46] D.J. Economou, Thin Solid Films, 365 (2000) 348.

[47] G.A. Bird, *Molecular Gas Dynamics and the Direct Simulation of Gas Flows*, Clarendon Press, Oxford (1994).

[48] E.S. Oran, C.K. Oh, B.Z. Cybyk, Ann. Rev. Fluid Mech., 30 (1998) 403.

[49] S. Varoutis, D. Valougeorgis, O. Sazhin, F. Sharipov, J. Vac. Sci. Technol. A, 26 (2008) 228.

[50] A.K. Rebrov, J. Vac. Sci. Technol. A, 19 (2001) 1679.

[51] D.B. Hash, T. Mihopoulos, T.R. Govindan, M. Meyyappen, J. Vac. Sci. Technol. B, 18 (2000) 2808.

[52] P.K. Shufflebotham, T.J. Bartel, B. Berney, J. Vac. Sci. Technol. B, 13 (1995) 1862.

Chapter I

Theoretical background and experimental techniques

I-1 HDP systems for the deposition of dielectrics

I-1.1 Chemical vapour deposition

Chemical vapour deposition (CVD) is the process of depositing a solid film from gaseous precursors [1,2]. CVD processes can be divided into two groups [1,3,4]. Thermal CVD processes include hot-wire and laser techniques, metalorganic CVD (MOCVD) processes and atmospheric-pressure CVD. Plasma enhanced CVD (PECVD) processes make use of glow-discharge plasmas and gaseous precursors to attain the chemical reactions necessary for film deposition to take place. A plasma discharge is created by supplying energy to the free electrons in a neutral gas. The electric field imposed across the volume of the gas will cause these electrons to be accelerated. If an electron has accelerated to a high enough velocity and collides with a neutral gas atom or molecule in the feed gas, it may cause electron-impact ionisation and dissociation and in the process release a new electron. These electrons are then again accelerated due to the electric field and will generate more ions and electrons. This effect leads to an avalanche current and a consequent breakdown of the gas.

Plasmas used for PECVD are not in thermal equilibrium, as the temperatures of the electrons are much higher than the temperatures of the ions and neutrals. They can thus cause chemical reactions to occur at lower temperatures than with thermal activation and were initially developed for encapsulation and passivation of microelectronic devices [1]. Different PECVD reactor configurations exist. They are classified by the frequency of the electric field (DC, RF or microwave

frequencies), whether the energy is coupled directly, capacitively or inductively to the plasma, where the substrate is placed with respect to the plasma volume, etc. The latter refers to the difference between a direct process, where the injected gas mixture, by-products, plasma and substrate are in close proximity, and a remote or downstream process, where the substrate is placed a distance away from the plasma generation zone[1,5]. PECVD techniques can use pressures in the range of 1 mTorr to 100 Torr, with substrate temperatures from 100 up to 900°C. PECVD-deposited films such as silicon oxide, silicon nitride and silicon oxynitride are used in various applications, ranging from optical filters and coatings, permeability coatings and scratch-resistant coatings to gate dielectrics in ULSI MOSFETs and thin film transistors (TFTs). The broad variety of applications makes it clear that the exact PECVD system design will depend on the application it will be used for. For instance, deposition on plastic substrates will require a technique that provides good quality films at a substrate temperature less than its glass transition temperature (~70°C for PET, for example), while applications which require a low concentration of bonded hydrogen incorporation, like waveguides, will benefit from using a high temperature and downstream process configuration.

Changes in the various deposition parameters such as the choice of precursor gases, the ratio and dilution of the gases, the pressure, power and temperature, can also be used to change the film properties. This flexibility in depositing films with tailored properties is a major advantage of plasma deposition techniques [6].

I-1.2 Advantages of HDP systems

The charge densities of plasmas [2,7] used in manufacturing technology are in the range of 10^8 to 10^{12} cm^{-3}. HDP CVD systems are usually classified as those that have densities higher than 10^{10} cm^{-3}, but what really set them apart are their very low pressures of operation. The increase in charge densities coupled with the low pressure operation of HDP systems, which is typically between 1 and 80 mTorr, lead to a greatly increased ratio of activated-to-background state fluxes of species arriving at the substrate surface. In this range of pressures, the charged-particle recombination is slower than the gas diffusion. The high electron densities will in turn lead to high levels of dissociation and fractional ionisation*. The reduced pressure leads to an increase in the mean free path (MFP) that suppresses most of the volume reactions. Since the sheath has a width which is much smaller than the MFP, the low pressure operation will also lead to the sheath becoming non-collisional and results in a highly directional flux of ions onto the substrate, with a narrow energy distribution.

I-1.3 Different HDP systems

Inductively coupled plasma (ICP) systems, helicon resonator systems and electron cyclotron resonance (ECR) plasma systems are the main types of HDP sources currently in use. These systems have certain features in common.

* Dissociation can approach 100%, while fractional ionisation can be up to 10%.

All three operate at pressures in the millitorr range and consequently have a non-collisional sheath. They also typically use two power sources. The purpose of this is to have one power source sustaining the plasma and controlling the plasma density, and another controlling the energy of the ions striking the substrate surface [2,8]. ICP and helicon reactors make use of radio frequencies in the MHz range to create the plasma, either via inductive coupling or helicon (whistler) waves. ECR systems use 2.45 GHz microwave frequency in the presence of a strong magnetic field to achieve resonant coupling.

I-1.3.1 ICP sources

Figure I-1 depicts an inductive driven source with a planar geometry. Contrary to helicon and ECR systems, inductive discharges (also referred to as transformer coupled plasmas) do not require a magnetic field, which makes them the simplest design.

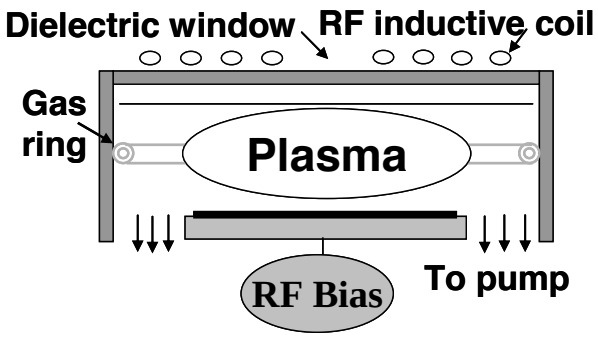

Figure I-1. Schematic of an inductive coupled plasma source.

I-1.3.2 Helicon sources

Helicon sources combine a DC axial magnetic field of 50 to 200 G with an RF antenna placed around a dielectric cylinder, as shown in Figure I-2 [2]. The magnetic field increases the skin depth in order to ensure that the inductive field can penetrate the entire plasma, as well as to confine the electrons. By varying the magnetic field the operator can also ensure a uniform plasma density distribution [7].

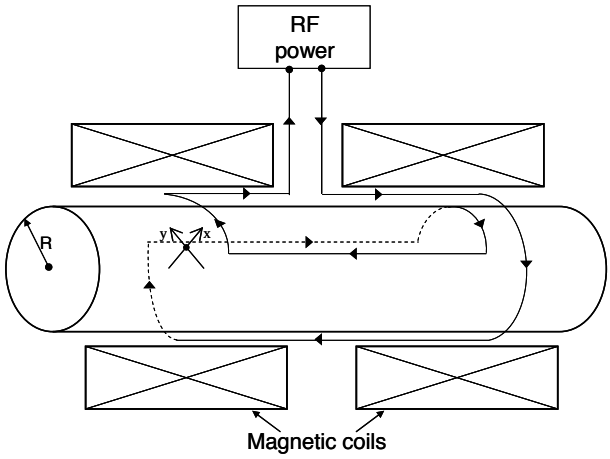

Figure I-2. A schematic example of a remote helicon source [2].

The energy from the wave launched by the antenna† is transferred to the plasma by propagating along the magnetic field lines, leading to high ionisation and high electron densities.

† Also referred to as a helicon wave.

I-1.3.3 ECR PECVD systems

By applying a static magnetic field the plasma can be confined. In the presence of a constant magnetic field *B*, a charged particle will gyrate at a cyclotron frequency ω_c defined by [2,7]

$$\omega_c = \frac{|qB|}{m} \qquad (I\text{-}1)$$

For electrons, the cyclotron frequency equals‡

$$f_c = \omega_c / 2\pi \approx 2.8 MHz / G \qquad (I\text{-}2)$$

The Larmor radius, also called the gyration radius, r_L is the radius of the circle of gyration of the charged particle in such a constant magnetic field, and is given by§

$$r_L = \frac{v_{\perp 0}}{\omega_c} \qquad (I\text{-}3)$$

If a microwave field with a frequency equal to the Larmor frequency is applied [2], microwave energy can be coupled to the plasma electrons. The electrons will then undergo one orbit during one period of the microwave field [1].

A linearly polarized electromagnetic wave launched into a vacuum chamber can be decomposed into its constituent right-hand and left-hand circularly polarized waves. For a wave polarized linearly in the x-direction, this is given by

‡ Where $1G = 10^{-4} Tesla$.

§ Where $v_{\perp 0}$ denotes the velocity component perpendicular to the magnetic field.

$$E(r,t) = \mathrm{Re}\left(\hat{x}E_x(r)e^{j\omega t}\right) \qquad (I\text{-}4)$$

$$\hat{x}E_x = (\hat{x} - j\hat{y})E_r + (\hat{x} + j\hat{y})E_l$$

An electron will be accelerated along its orbit throughout the entire period of the RHP wave field, while there will be no energy gain for the LHP wave field. This effect is shown in Figure I-3 [9]. Figure I-4 shows a schematic representation of an ECR-PECVD system.

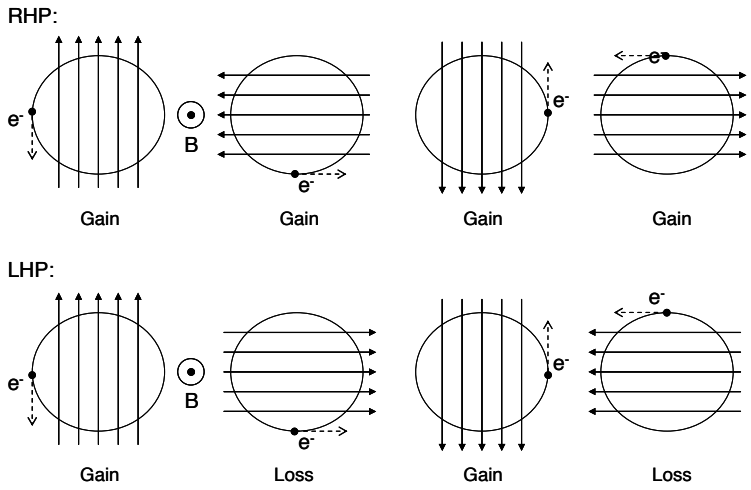

Figure I-3. The ECR heating principle, for RHP and LHP waves.

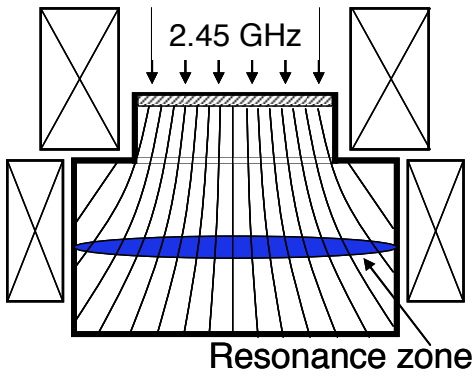

Figure I-4. A schematic representation of a divergent ECR-PECVD system.

The common microwave frequency of 2.45 GHz is used with a magnetic field of 875 Gauss to produce electron cyclotron resonance conditions. The low pressure operation of these systems is essential to ensure that the electrons will undergo resonant heating due to efficient absorption of the microwave field, and will not suffer elastic collisions with other particles, contributing to the ohmic heating of electrons.

I-1.4 The MDECR PECVD reactor Venus

The MDECR-PECVD system *Venus*, shown in Figure I-5, was used in this thesis and is an example of a HDP CVD system. The concept of an MDECR plasma source was originally developed by the group of Jacques Pelletier[10] in INP, Grenoble, France.

The MDECR-PECVD reactor consists of a 50 litre cylindrical vacuum chamber, placed above an Alcatel ATP 1600 l/s turbomolecular pump. Two 2 kW continuous wave magnetron generators each supply the 2.45 GHz microwave power to eight-way waveguide-to-coaxial splitters. These are connected by coaxial lines to 16 water-cooled microwave antenna applicators, each with an integrated $SmCo_5$ magnet, arranged in a matrix configuration. Sixteen circulators equipped with water cooled dummy loads protect the microwave circuitry from the power that may be reflected from the antennas. A substrate holder with a 22 cm diameter is placed horizontally inside the chamber. It is equipped with a 13.56 MHz RF substrate bias source and can also be heated to 300°C.

The distance from the antennas to the substrate holder is approximately 12 cm. The different components of the system are depicted schematically in Figure I-6.

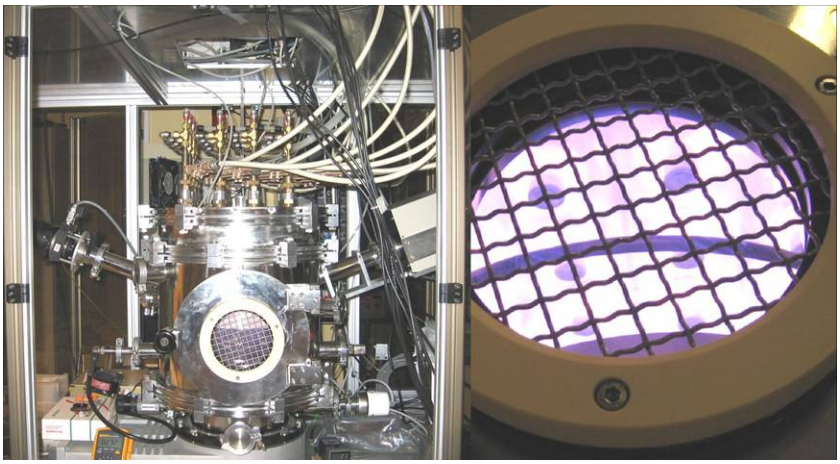

Figure I-5. Left: The MDECR-PECVD system, Venus. Right: An argon plasma with the resonant zones formed around some of the integrated magnets of the microwave antennas.

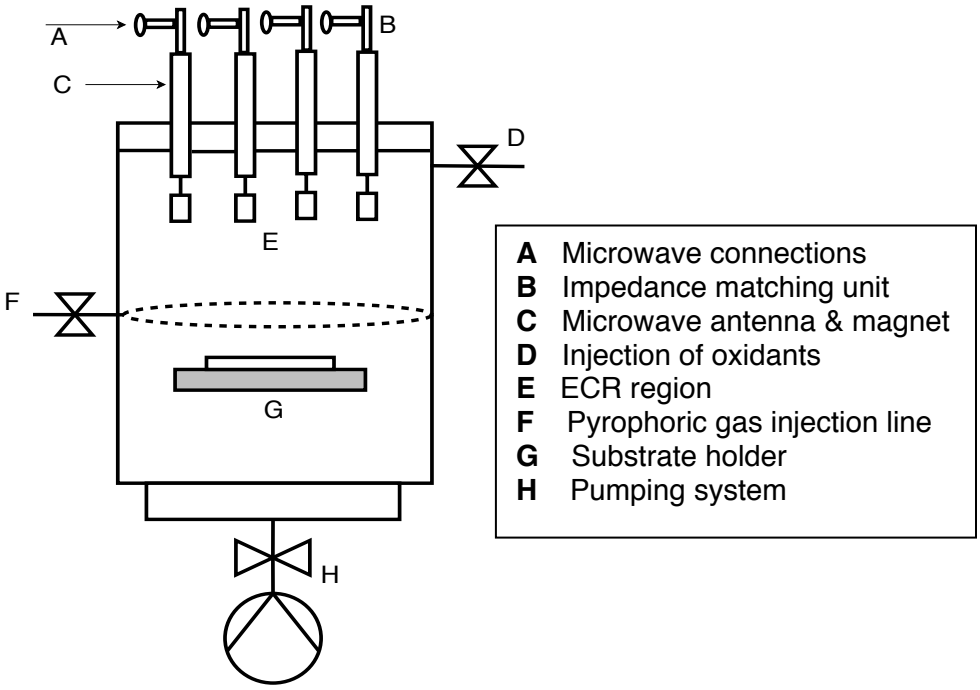

Figure I-6. Schematic of the MDECR-PECVD system.

I-1.4.1 The microwave antenna matrix configuration

As mentioned above, the deposition system used in the experiments has a 4 x 4 magnet matrix configuration of the microwave injection antennas. Of the 16 antennas, the integrated magnets have different polarities, as shown in Figure I-7. Initially a configuration such as shown in Figure I-7 *(a)* was used, where 4 similar polarities were placed on the corners of the 4 x 4 matrix. This configuration was later changed to the configuration shown in Figure I-7 *(b)*, with one polarity being placed along the diagonal of the matrix[11].

The distance between the centres of two antennas is 8 cm, meaning that a 200 mm Si-wafer can fit entirely under the four central antennas of the matrix configuration, as indicated in light grey on the figure.

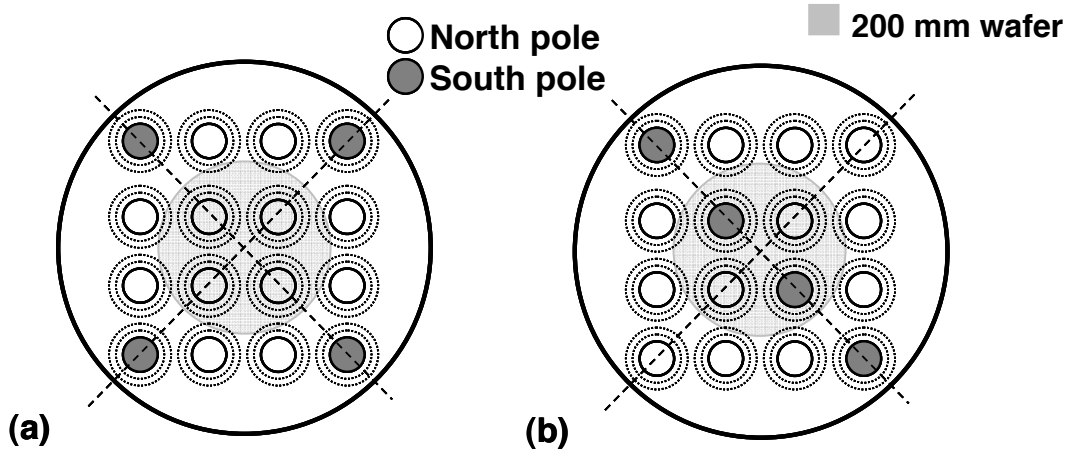

Figure I-7. Two arrangements of the ECR magnet matrix configuration.

Mappings of the thickness of SiO_2 layers deposited onto 200 mm diameter wafers can be seen in Figure I-8. They show the uniformity of the deposition in the different antenna configurations shown in Figure I-7. The arrangement of the antennas in Figure I-7 *(a)* resulted in a uniformity of ± 10.4%. The changed configuration in Figure I-7 *(b)* improved the uniformity of the deposition to ± 3.3% across the 200 mm diameter wafer.

The multi-polar confinement due to the extension of the magnetic field lines between the neighbouring antennas thus considerably improves the uniformity of the ion flux onto the surface. The uniformity could probably be improved even further if 8 of each magnet polarity were to be used, which is unfortunately not available to us at present.

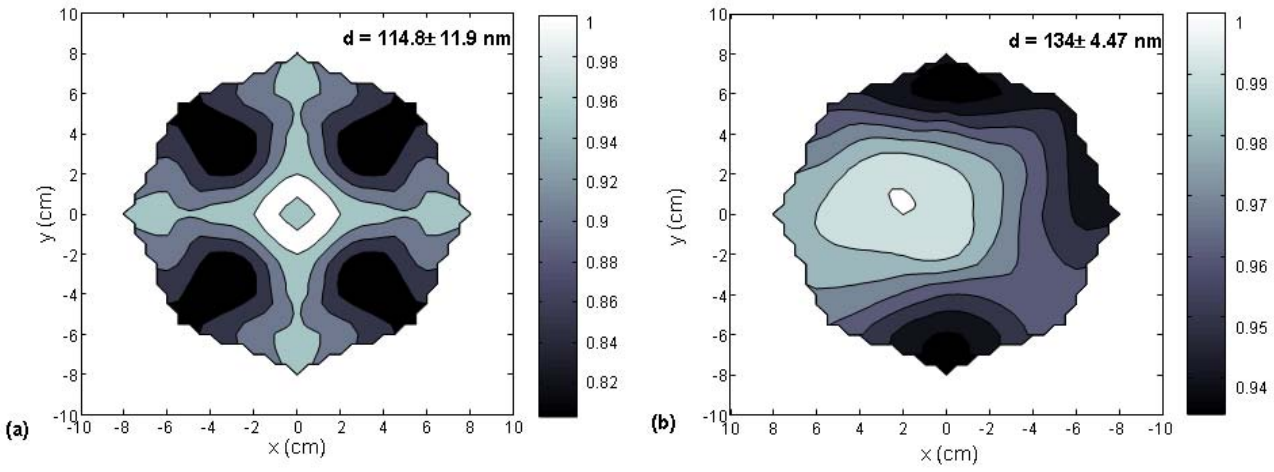

Figure I-8. Uniformity contours of thickness normalized SiOx depositions onto 200 mm diameter wafers. *(a)* corresponds to the layout shown in Figure I-7*(a)*, while *(b)* is the result of the arrangement in Figure I-7*(b)*.

I-2. Film characterization techniques

I-2.1 Phase modulated spectroscopic ellipsometry

Ellipsometry is the method of choice for calculating the thickness and optical constants of thin transparent or absorbing films, semiconductor and dielectric films [1,12,13]. The technique is based on measuring the change in polarization state of a light beam after its reflection from a film surface.

Consider the case shown in Figure I-9, where linearly polarized light is incident at an angle of ϕ on a film with refractive index n_1 and then reflected. The reflected light in the general case will be elliptically polarized.

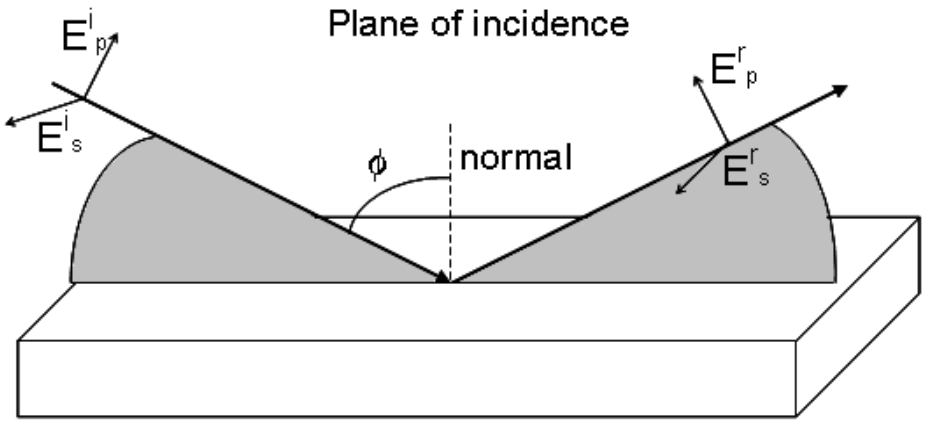

Figure I-9. Reflection of a linearly polarized light beam from a surface.

The fundamental equation of standard ellipsometry defines ρ as the ratio of the complex Fresnel reflection coefficients r_s and r_p, and is given by

$$\rho = \frac{r_p}{r_s} = \frac{E^r{}_p / E^i{}_p}{E^r{}_s / E^i{}_s} = \tan\psi e^{i\Delta} \qquad (I\text{-}5)$$

Where Δ and ψ are the ellipsometric angles and E_p and E_s the parallel and perpendicular components of the electromagnetic wave. In a phase modulated spectroscopic ellipsometer [14] such as the Uvisel (Jobin-Yvon Horiba) shown in Figure I-10 and used for the purpose of this study, a silica bar fused to a quartz transducer works as a photoelastic phase modulator at an operating frequency of 50 kHz.

Measurements are taken in the wavelength range from either 1700 nm (0.73 eV) or 826.6 nm (1.5 eV) to 248 nm (5 eV) with a spectral resolution specified by the user. The polarizer and analyzer angles are in most cases set to 0 and 45 degrees respectively.

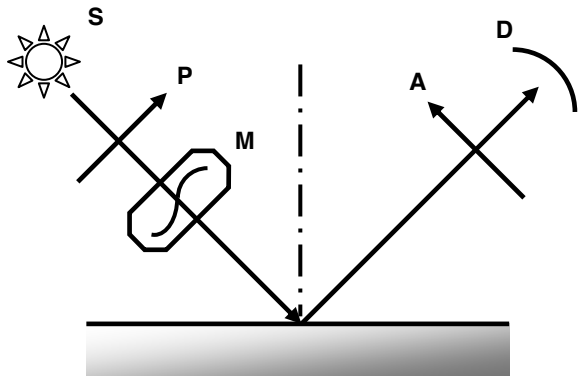

Figure I-10. Schematic view of a phase modulated ellipsometer: S: source, P: polarizer, M: modulator, A: analyzer, D: detector.

If the modulated phase is given by $\delta(t) = A\sin(\omega t)$ then the measured intensity at the detector is given by

$$I(t) \propto I_0 + I_s \sin\delta(t) + I_c \cos\delta(t) \qquad \textit{(I-6)}$$

The DC component I_0, first and second harmonics of the modulation frequency, I_s and I_c, are recorded during phase modulated spectroscopic measurements. Phase modulated ellipsometry determines the values of the ellipsometric angles ψ and Δ from the harmonics values through the complex Fresnel reflection coefficients as follows:

$$I_s = 2\,\mathrm{Im}\left(\frac{r_s r_p^{\,*}}{r_s r_s^{\,*} + r_p r_p^{\,*}}\right) = \sin 2\psi \sin\Delta$$
$$I_c = 2\,\mathrm{Re}\left(\frac{r_s r_p^{\,*}}{r_s r_s^{\,*} + r_p r_p^{\,*}}\right) = \sin 2\psi \cos\Delta \qquad \textit{(I-7)}$$

The measured ellipsometric data were interpreted by comparing them to a calculated response of an optical model based on an Abelès matrix approach [15], specific dispersion relation** and the Bruggeman Effective Medium Approximation[16]. The model of the structure was developed using the DeltaPsi II software package supplied by the ellipsometer manufacturer and consists of a substrate (either with a specified or semi-infinite thickness), a film (or stacks of films) and a surface roughness layer. The surface roughness was taken into account by adding a layer consisting of a 50% material and 50% void mixture and fitting on its thickness.

** Appendix A discusses the classical Lorentz-oscillator and Tauc-Lorentz models.

I-2.2 Fourier Transform Infrared Spectroscopy

Infrared (IR) spectroscopy is a widely used, non-destructive technique supplying information about the chemical composition and bonding in thin films [17]. The vibrational excitation of molecules usually cause absorption in the IR region, as shown in Table I-1 for some chemical bonds of interest in this study [18-20]. If the radiation incident on a sample thus has the frequency corresponding to the resonance frequency of a specific chemical bond found in the sample, the molecular bonds will vibrate. This vibration can take many forms, such as a stretching, bending or rocking action. If the vibration causes a change in the dipole moment of the molecule, in other words causes a charge imbalance, it is said to be IR active and will absorb the incident radiation[17].

A FTIR spectrometer consists of a light source, interferometer, movable and stationary mirrors and a detector, as shown in Figure I-11. The light is split into two beams, after which one beam is reflected from a stationary mirror and the other is reflected from a movable mirror, which introduces a time delay. The light is then recombined and traverses the sample. This interference signal gives the temporal coherence, which is then recorded by the detector at different positions of the movable mirror, thus at different time delays. The Fourier transform is then taken of the temporal coherence at these different time delays, which enables us to reconstruct the spectrum.

Chemical bond	Wavenumber (cm^{-1})
Si-O-Si (Rocking)	450
Si-O-Si (Bending)	800
Si-O-Si (Stretching)	1075
Si-N (Stretching)	~880
N-H (Bending)	1175
N-H (Stretching)	~3200
Si-OH	950
Si-OH (water symmetric feature)	3350 band
Si-OH (asymmetric feature)	3650 band
Si-H	~2300

Table I-1. Absorption bands of different chemical bonds in the IR range.

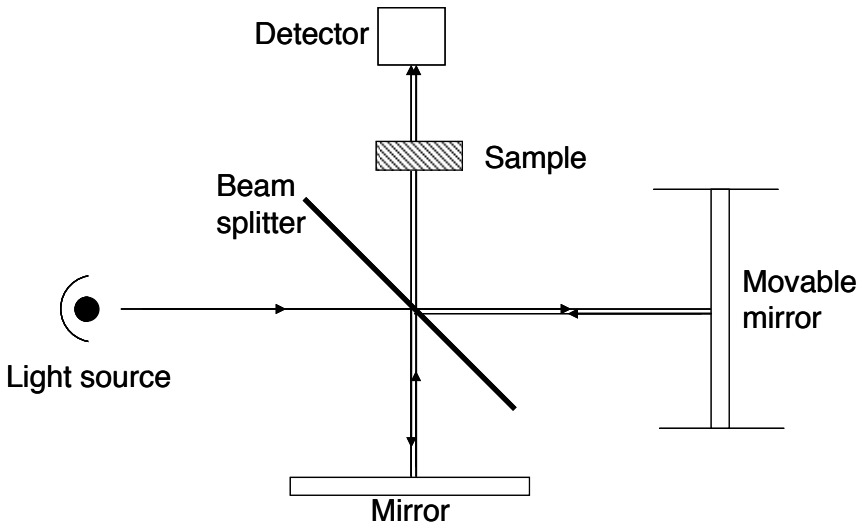

Figure I-11. The operation of an FTIR spectrometer.

The detection limit of the instrument, which is usually specified in absorption, depends on the path length and the signal to noise ratio and is usually in the vicinity of 1 percent. A thicker film will allow a lower concentration of a specific bond to be quantified; however interference effects in the film-substrate system will severely complicate the analysis at larger thicknesses.

FTIR measurements were taken using a Bruker Equinox 55 spectrometer with a resolution of 4 cm^{-1} in the 400 to 4000 cm^{-1} wavenumber range. The device was purged with dry nitrogen before and during each measurement to remove absorption peaks due to atmospheric water. During analysis of the recorded signal the baseline and absorption of the crystalline silicon substrate are subtracted and the samples are thickness normalized using the thickness calculated from spectroscopic ellipsometry measurements.

I-2.3 Transmission spectroscopy

As the OH content in the films deposited during the experiments was typically less than the FTIR detection limit mentioned above, transmission measurements were performed on thick SiO_2 layers deposited onto Infrasil fused quartz substrates with dimensions of 72 mm x 24 mm x 1 mm. In transmission spectroscopy measurements a monochromator is used instead of an interferometer, as used in an FTIR spectrometer.

For the purpose of this study a Varian Cary 500 UV/visible/NIR spectrophotometer was used. Baseline corrected measurements were taken

between 3040 and 4000 cm^{-1} with a data interval of 4.10 cm^{-1}. During analysis of the transmission measurements the transmission of the substrate is subtracted and the samples are thickness normalized to make comparison between the different samples possible.

In both FTIR and transmission spectroscopy, information can be obtained from the chemical bond's peak position, width and integrated peak intensity. The first two parameters supply qualitative information of the film, concerning the identification of the chemical bonds shown in Table I-1, the possible stresses in the film, defects and bond strain, while the latter directly relates to the concentration[††] of a specific chemical bond [17,21].

I-2.4 Atomic Force Microscopy

Atomic Force Microscopy (AFM) supplies information on feature dimensions and the roughness of a surface. This technique traces the topography of a surface by detecting the Van der Waals force interaction between a probe tip and the surface. Since it detects a force, it can be used on metal, semiconductor and insulator surfaces [1]. A sharp tip is mounted on a cantilever spring which has a spring constant[‡‡] *k* that is smaller than the spring constant between the atoms.

[††] For quantitative values the Beer-Lambert law, that relates the absorbance A_w to the transmittance T_w, needs to be used . It is given by $Aw = -\log Tw = (\varepsilon w)(bc)$ with ε_w referring to a proportionality constant, *b* the sample thickness and *c* the chemical bond concentration.

[‡‡] Where Hooke's law defines the spring constant *k* by: $F=kx$. *F* is the restoring force exerted by the material and *x* is the quantity by which the spring has been stretched or compressed. The atomic spring constant *k* is defined in terms of the atomic spacing *a*, the atom's mass *m*, the bulk modulus *K* and the density ρ as $\sqrt{\frac{K}{\rho}} = a\sqrt{\frac{k}{m}}$.

The applied force is also kept small enough to avoid displacement of the surface atoms. The nanometre-sized tip is usually made of silicon or silicon nitride. The cantilever deflection is detected using a laser spot reflected from the cantilever onto photodiodes, as shown in Figure I-12.

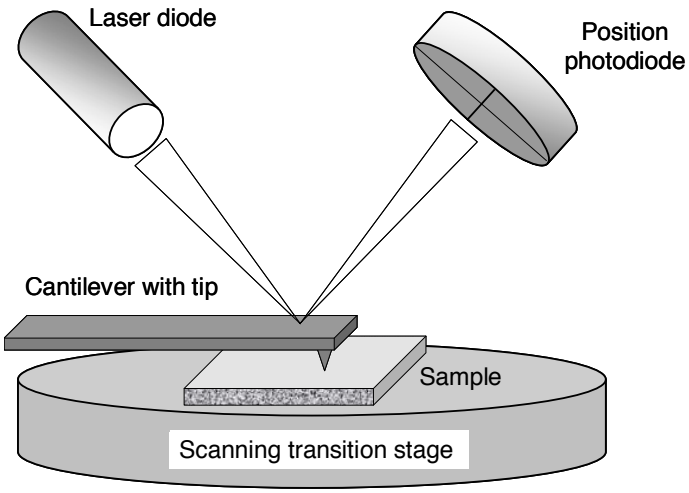

Figure I-12. The cantilever tip, laser diode and detector photodiodes of an atomic force microscope.

Measuring in tapping (or non-contact) mode entails vibrating the cantilever with a piezoelectric element at a frequency close to its resonance frequency. Close to the surface the Van der Waal forces will reduce the oscillation's amplitude. These changes in the vibrational amplitude due to the topography are consequently detected and recorded as surface images.

I-3. Plasma characterization techniques

I-3.1 Optical emission spectroscopy

During an electrical discharge, electron impact may lead to a subsequent transfer of energy to the atoms or molecules and consequent excitation or ionization of the particles. This will lead to a population of the electronic, rotational and vibrational excited states of the atoms or molecules. A decay from these excited states can either take place through the radiative emission of photons at different wavelengths or by the molecule breaking up [2]. The vibrational spectra form a series of bands in the infrared wavelength range. The rotational spectra are grouped as a set of lines in bands of rotation in the microwave range. The emission spectra for a SiH_4 and N_2 plasma is shown in Figure I-13, with the different electronic excited state bands of nitrogen in the UV clearly visible. Figure I-14 shows the UV-Vis-NIR emission spectra of a SiH_4 and O_2 deposition plasma, with a small quantity of Ar added.

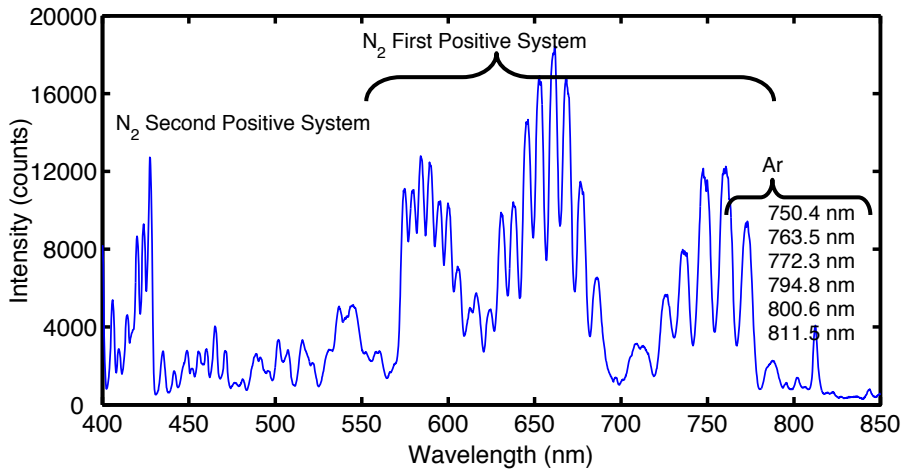

Figure I-13. Optical emission spectra of a silane, nitrogen and argon plasma.

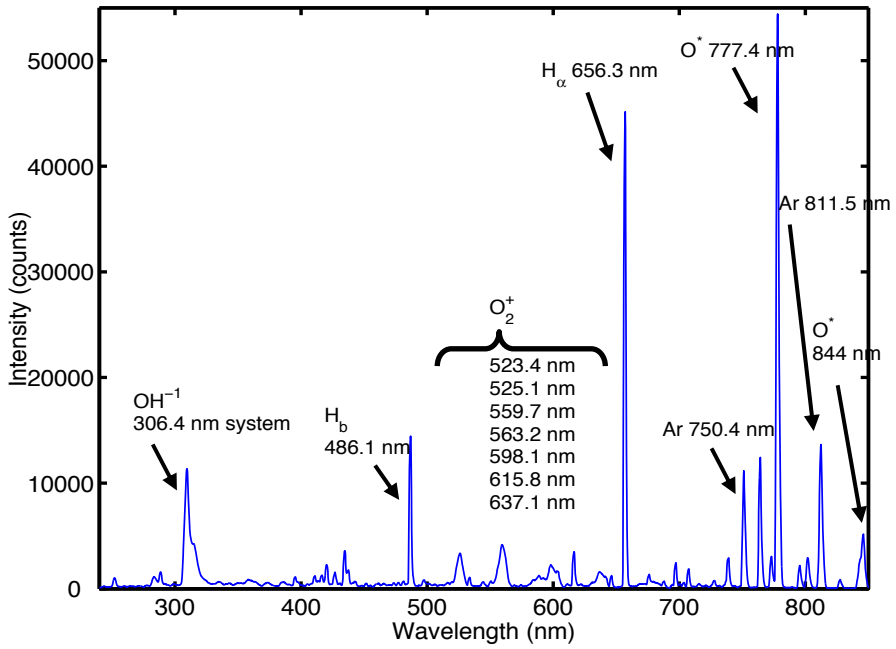

Figure I-14. Optical emission spectra of a silane, oxygen and argon plasma.

Optical spectroscopy offers several advantages[2,21,22]. It is a non-invase technique, meaning that it doesn't influence the process, and is robust. Compared to techniques such as quadrupole mass spectrometry, it is relatively easy to implement, though sometimes difficult to interpret. As shown in Figure I-13 the spectra of a diatomic molecule such as nitrogen is however very complicated due to the large quantity of vibrational and rotational states, making the identification of emission lines difficult when using an optical spectrometer with an inadequate optical resolution.

Collisional excitation and de-exciation of atoms can be represented by the following equation:

$$A + e^- + \Delta E \Leftrightarrow A^* + e^- \qquad \textit{(I-8)}$$

where ΔE represents the transferred kinetic energy. The excitation can only take place if the electron kinetic energy is higher than the separation between the energy levels, meaning that there is a threshold energy E_{th} (and thus a corresponding threshold velocity v_{thr}) for excitation. The excitation cross section $\sigma(v)$ will have a zero value below the threshold velocity, then increase with increased velocity and start to decrease again due to the interaction time between the particle and the electron being too small for the efficient transfer of energy to take place.

Figure I-15*(a)* shows the excitation cross section's overlap with the Maxwellian electron velocity distribution $f(v)$. The product $f(v)\cdot v\cdot\sigma(v)$ represents the probability of a collision transition per atom and per electron with a specific velocity v, as shown in figure I-15*(b)*. Taking the area under this curve results in the rate coefficient, in other words the total collision probability per atom and per electron.

Optical emission spectrometry can be used for qualitative measurements, where the emission lines for the electronically excited state of the precursors are identified. In order to obtain quantitative values of the density of a specific radical in the plasma, a technique called actinometry can be used if emission is due to excitation of the ground state of the atom or molecule. It involves adding a small quantity of an inert gas to the plasma. If the excitation threshold for a specific excited state of the inert gas at wavelength λ' is close to that of an excited state of the radical at wavelength λ, they will have a similar overlap with the electron velocity distribution function, as shown in Figure I-15.

The cross sections are then approximated with values close to the threshold, $\sigma_{\lambda'Ar}$ and $\sigma_{\lambda rad}$, using proportionality constants[2]:

$$\sigma_{\lambda' Ar} \approx C_{\lambda' Ar}\left(\nu - \nu_{thr}\right)$$
$$\sigma_{\lambda rad} \approx C_{\lambda rad}\left(\nu - \nu_{thr}\right) \qquad \text{(I-9)}$$

From the ratio of these quantities the density of the radical under investigation can be extracted:

$$n_{rad} = Cn_{Ar}\frac{I_{\lambda}}{I_{\lambda'}} \qquad \text{(I-10)}$$

Even if the proportionality constant *C* is unknown, the trend in the radical's density with changing plasma parameters can be seen[2].

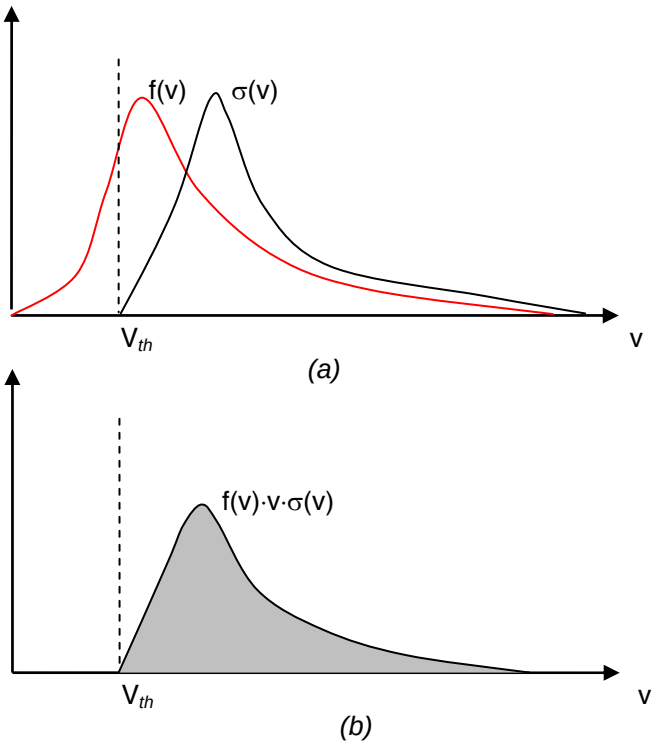

Figure I-15. ***(a)*** **Overlap of the excitation cross section** ***σ(v)*** **with the Maxwellian electron velocity distribution** ***f(v)*****.** ***(b)*** **The product** ***f(v)·v·σ(v)*** **is the rate coefficient.**

I-3.1.1 Experimental setup

For the purpose of this study, an *Ocean Optics* USB4000 fibre-optic optical emission spectrometer was used. Measurements were taken at the level of the substrate holder, as indicated on Figure I-16 and Figure I-17. The device allows measurements in the range of 200 to 850 nm with an optical resolution of 2 nm. The emission lines of the radicals investigated in this study are summarized in Table I-2 [24 – 30].

A small quantity of argon, less than 5 % of the gas mixture, was added in order to perform actinometry. The threshold energy for the argon emission line is 13.47 eV, while it is 10.98 eV for the oxygen emission line at 844 nm and 12.06 eV for the atomic hydrogen Balmer line at 656.6 nm.

Species	Wavelength (nm)
OH	306.4 system
O	844
Ar	750.4
H_α	656.6

Table I-2. Emission wavelengths of radicals investigated.

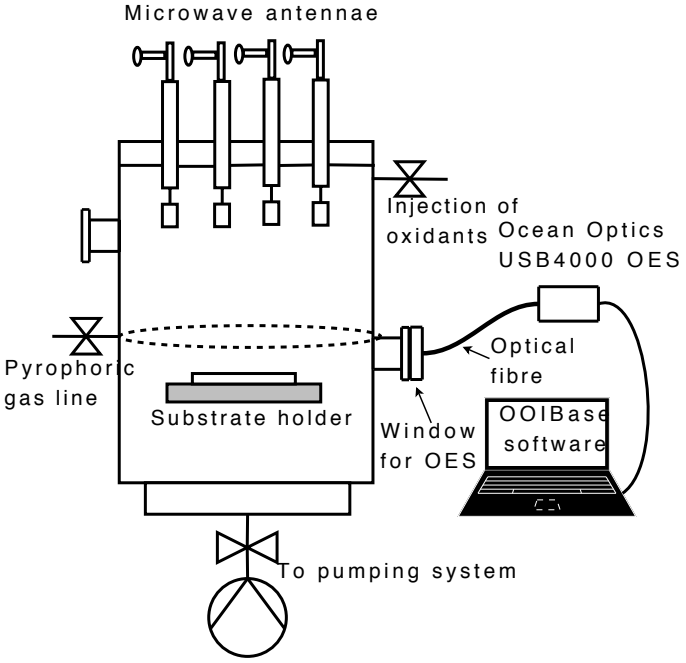

Figure I-16. System setup for OES measurements.

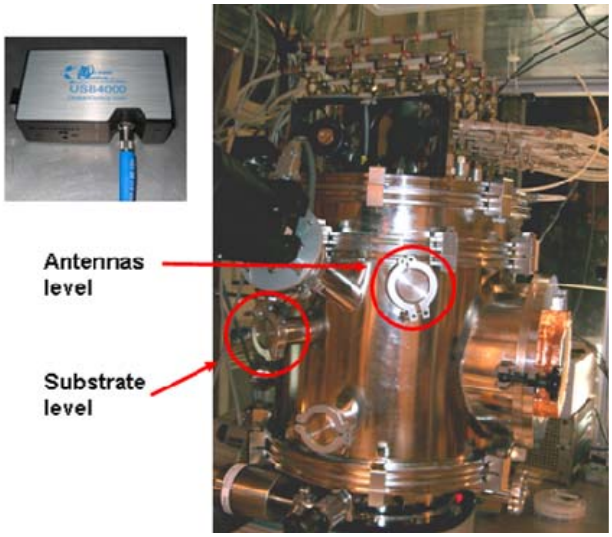

Figure I-17. OES device and positions where measurements were taken.

I-3.2 Differentially pumped quadrupole mass spectrometry

Mass spectrometry is a technique that allows us to detect all the plasma produced radicals, ions, neutral atoms and molecules. Two methods can be used to detect these species [31]:

1. In *electron impact ionisation* of neutral species electrons are produced by thermo-ionic emission from a hot filament, such as a Tungsten or thoriated iridium wire. These electrons are then accelerated to the chosen electron energy, which is typically 70 eV. This is higher than the maximum ionisation efficiency curve for most atoms and molecules.
2. *Ion mass spectrometry* involves measuring the ions created within a discharge by switching off the electron impact source in the QMS head. This technique is less reliable as the low concentrations of the created species can be very difficult to detect.

In both of these cases the effect of mass dependent sampling efficiencies needs to be taken into consideration, as higher mass particles will usually have a lower detection. The different ionisation cross-sections of the various species and the pressure differences between the plasma chamber and the QMS should also be taken into account.

The most common mass spectrometry technique used in plasma processing and in most residual gas analysis applications is quadrupole mass spectrometry (QMS) [32]. It consists of 4 symmetrically arranged parallel cylindrical rod electrodes, arranged as shown in Figure I-18. The filament is usually made from thoriated iridium wire, though tungsten can also be used. By using this

configuration, together with specific DC and AC voltages, an ionisation source and a detector, ions can be identified by their mass. As the DC and AC voltages are superimposed, an ion with a specific mass to charge (m/z) ratio will pass along the central axis of the quadrupole until it reaches the detector. Lighter or heavier ions will not reach the detector, as they will be deviated from the central axis towards the electrodes and be neutralized. Changing the AC and DC voltages or frequency makes it possible to detect different ions. A mass spectrum is simply a plot of the detector output as a function of m/z. For a specific molecule there also exists a cracking pattern that defines which ions are more likely to form. Mass spectrums and cracking patterns may vary if measured by different spectrometers with different settings and can also change with time.

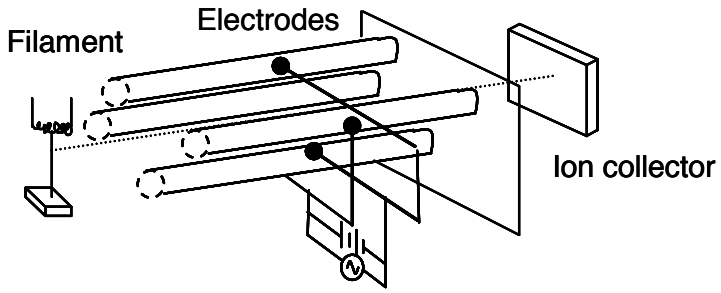

Figure I-18. Quadrupole mass spectrometer operation.

To get accurate data of the basic chemistry in the plasma, the mass spectrometer must be kept as sensitive as possible. A gas such as silane can for example react on the hot filament surface and create a silicon layer, which will change the work function and consequently the electron emission from the filament.

Another factor that needs to be taken into account when using electron impact ionisation, is that the electron energy is usually high enough to ionise the atom or molecule, as well as cause dissociative ionisation. It is thus better to operate the ion source at a lower electron energy, which is still above the ionisation potential (IP) of the specific atom or molecule, but not high enough to lead to dissociative ionisation.

I-3.2.1 Experimental setup

For the purpose of this study, a *Thermco* VGQ Residual Gas Analyser (RGA) system was used. It was placed behind the turbo-molecular pump of the deposition system, as shown in Figure I-19. A large pressure differential exists between the reactor chamber which operates in the millitorr range[§§] and the pressure necessary for the QMS's operation, which is smaller than $1e^{-5}$ mbar. To achieve this, the mass spectrometer samples the exhaust gas flow of the system through a 100 μm knife-edge orifice, and is differentially pumped with a 1000 l/sec turbo-molecular pump and rotary vane backing pump. Though orifice sampling is difficult to implement, it is the method of choice for quantitative in-situ measurements[32]. A photograph of the *Thermco* mass spectrometer used in this study can be seen in figure I-20. The QMS was differentially pumped to a pressure of less than 2×10^{-6} mbar before use. A thoriated iridium filament and emission current of 1.6 A was used to perform the electron impact ionisation measurements [33].

[§§] Where 0.750 torr = 1 mbar = 100 Pa and 760 torr = 1 standard atmosphere

Electron energy was set to 70 eV which is, as mentioned before, higher than the maximum ionisation energy for most atoms and molecules. It can however also create doubly charged ions [31]. A repeller voltage of -110 V, applied to the outside cage of the QMS, ensures that most of the electrons in the ionisation chamber are kept inside. Resolution was set by the DC offset, which was kept at -0.2593V in this study. A pole bias voltage of 2V retards the ions and ensures a uniform peak shape and efficient ion extraction [33].

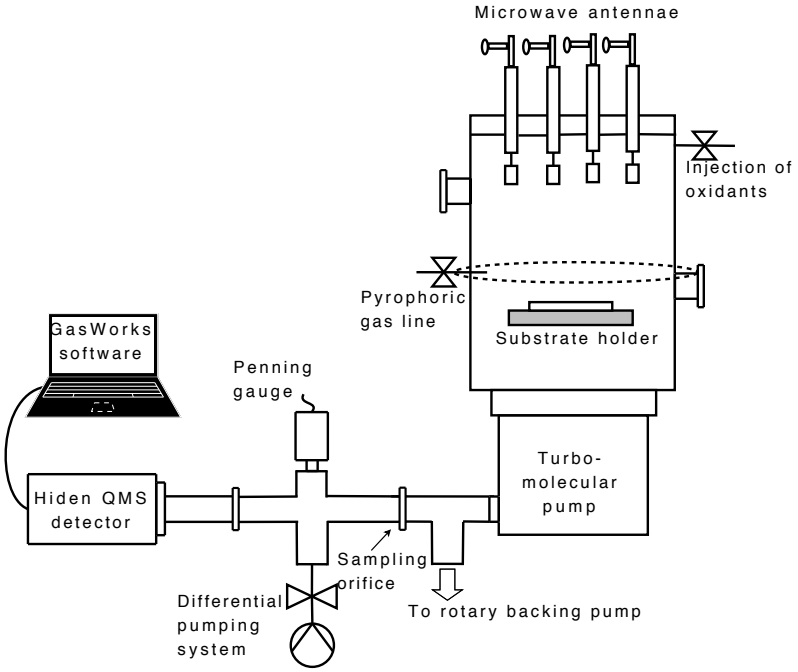

Figure I-19. System setup for QMS measurements.

Figure I-21 shows an example of a QMS mass spectrum of air which forms the background when the system is pumped. Table I-3 contains a summary of ions

that were looked at during this study, together with their corresponding mass values [34-38].

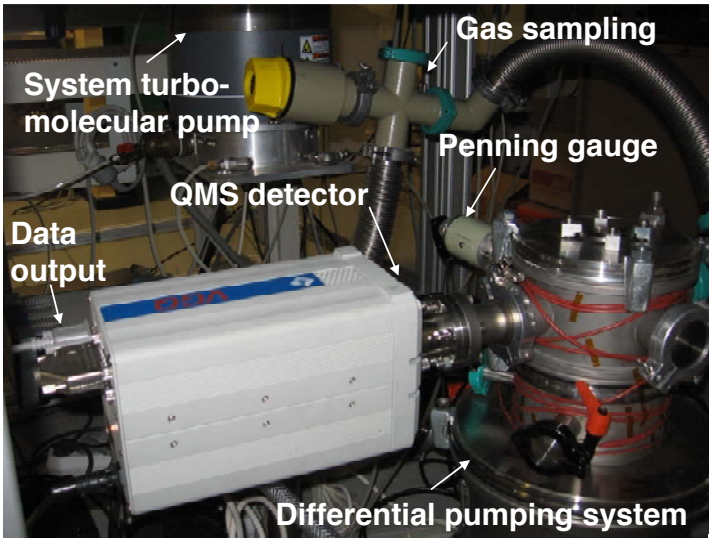

Figure I-20. Experimental setup of differentially pumped QMS system.

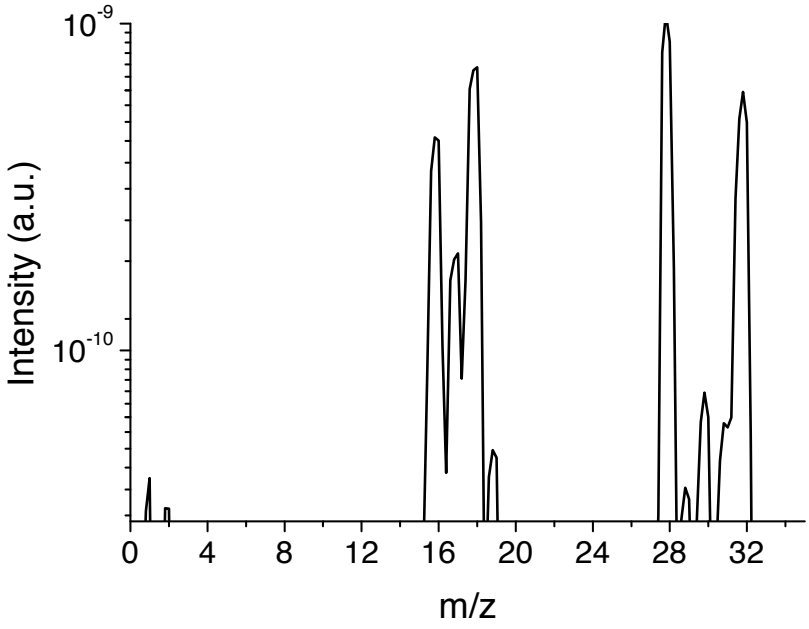

Figure I-21. Example of a QMS mass spectra taken in air.

Ion	m/z	Source gas
H_2O^+	18	H_2O
N_2^+	28	N_2
O_2^+	32	O_2
SiH_2^+	30	SiH_4
Ar^+	40	Ar

Table I-3. QMS ions monitored during this study.

I-4 Conclusion

The aim of this chapter was to provide the reader with background concerning the high density plasma system *Venus* employed in this study, its design and capabilities and to present the key characterization techniques used. In Section I-1 a brief introduction to chemical vapour deposition (CVD) and plasma assisted techniques, focussing on high density plasma (HDP) sources, was given. The operation of an electron cyclotron resonance plasma enhanced chemical vapour deposition (ECR-PECVD) system was discussed, with specific emphasis placed on the matrix distribution configuration. The major film characterization techniques used during the study were shown in Section I-2. The chapter concludes in Section I-3 with a discussion of the optical emission spectroscopy and differentially pumped quadrupole mass spectrometry plasma characterization techniques, together with an overview of their implementation in the MDECR-PECVD system.

References

[1] M. Ohring, *Materials science of thin films: Deposition and structure, second edition*, Elsevier Academic Press, Hoboken, New Jersey (2002) 337.

[2] M.A. Lieberman, A.J. Lichtenberg, *Principles of Plasma Discharges and Materials Processing second edition*, John Wiley & Sons Inc., Hoboken, New Jersey (2005) 621.

[3] H. Conrads, M. Schmidt, Plasma Sci. Technol., 9 (2000) 44.

[4] A. Bogaerts, E. Neyts, R. Gijbels, J. van der Mullen, Spectrochimica Acta Part B, 57 (2002) 609.

[5] D.R. Cote, S.V. Nguyen, A.K. Stamper, D.S. Armbrust, D. Többen, R.A. Conti, G.Y. Lee, IBM J. Res. Develop., 43(1/2) (1999).

[6] S.V. Nguyen, IBM J. Res. Develop., 43 (1999) 109.

[7] F.F. Chen, J.P. Chang, *Lecture notes on principles of plasma processing*, Springer, Los Angelos (2003).

[8] D. Graves, IEEE Trans. Plasma Sci., 22 (1994) 31.

[9] M.A. Lieberman and R.A. Gottscho, *Design of High-Density Plasma Sources for Materials Processing, Physics of Thin Films*, edited by M. Francombe and J. Vossen, Academic Press, New York, 18 (1994) 1.

[10] A. Lacoste, T. Lagarde, S. Béchu, Y. Arnal, J. Pelletier, Plasma Sources Sci. Technol., 11 (2002) 407.

[11] R. Botha, B. haj Ibrahim, P. Bulkin, B. Drévillon, Thin Solid Films, 515 (2007) 7594.

[12] B. Drévillon, Prog. Cryst. Growth Char. Mat., 27 (1993) 1.

[13] R. Azzam, N. Bashara, *Ellipsometry and polarized light*, North Holland Personal Library (1970).

[14] S.N. Jasperson, D.K. Burge, R.C. O'Handley, Surface Science, 27 (1973) 548.

[15] F. Abelès, Annales de Physique, 5 (1950) 596 (706).

[16] D.A.G. Bruggeman, Ann. Physik, Leipzig, Germany, 24 (1935) 636.

[17] J.N. Cox, *Fourier Transform Infrared Spectroscopy, Section 8.1 in Encyclopaedia of materials characterization*, Edited by C.R. Brundle, C.A. Evans Jr., S. Wilson, Butterworth-Heinemann, Stoneham MA (1992).

[18] S. Dreer, P. Wilhartitz, Pure and Applied Chemistry, 76 (2004) 1161.

[19] G. Lucovsky, P.D. Richard, D.V. Tsu, S.Y. Lin, R.J. Markunas, J. Vac. Sci. Technol. A, 4 (1986) 681.

[20] A. Canillas, A. Pinyol, J. Sancho-Parramon, J. Ferré-Borrull, E. Bertran, Thin Solid Films, 455 (2004) 167.

[21] W.A. Lanford, M.J. Rand, J. Appl. Phys., 49 (1978) 2473.

[22] J.R. Roberts, J. Res. Nat. Inst. Std & Technol., 100 (1995) 353.

[23] U. Fantz, Plasma Sources Sci. Technol, 15 (2006) 137.

[24] A. Granier, M. Vervloet, K. Aumaille, C. Vallée, Plasma Sources Sci. Technol., 12 (2003) 89.

[25] K. Aumaille, A. Granier, M. Schmidt, B. Grolleau, C. Vallée, Plasma Sources Sci. Technol., 9 (2000) 331.

[26] J.C. Thomaz, J. Amorim, C.F. Souza, J. Phys. D: Appl. Phys., 32 (1999) 3208.

[27] S.F. Yoon, K.H. Tan, Q. Zhang, M. Rusli, J. Ahn, L. Valeri, Vacuum, 61 (2001) 29.

[28] T.T. Chau, K.C. Kao, J. Vac. Sci. Technol. B, 14 (1996) 527.

[29] A.J. Flewitt, A.P. Dyson, J. Robertson, W.I. Milne, Thin Solid Films, 383 (2001) 172.

[30] M. Tadokoro, A. Itoh, N. Nakano, Z. Lj. Petrovic, T. Makabe, IEEE Transactions on Plasma Science, 26 (1998) 1724.

[31] W. Stoffels, *Plasma diagnostics: Absorption and mass spectrometry*, European summer school on Low Temperature Plasma Physics, Bad Honnef, Germany (October 2006).

[32] P.H. Dawson, *Quadrupole mass spectrometry and its applications*, American Institute of Physics, New York, (1997).

[33] VGQ operations manual, Onix systems Inc., (1998).

[34] R. Robertson, D. Hils, H. Chatham, A. Gallagher, Appl. Phys. Lett., 43 (1983) 544.

[35] H. M. Rosenstock, K. Draxl, B. W. Steiner, J. T. Herron, J. Phys. Chem. Ref. Data, Suppl. 1, 6 (1977) 1.

[36] J. Jolly, *Spectrométrie de masse des plasmas réactifs*, DEA Physique des Plasmas (2003).

[37] Leybold Vacuum, *Mass spectrometry, Products and reference book* (2001/2002).

[38] P. Kae-Nune, J. Perrin, J. Guillon, J. Jolly, Plasma Sources Sci. Technol., 4 (1995) 250.

Chapter II

The influence of the process parameters on the plasma and material properties

II-1 Introduction

In this Chapter, the characterization of the MDECR-PECVD system for the deposition of SiO_2, SiN_x and SiO_xN_y thin films is reported. The influence that changes in the gas flow ratios and other process parameters, such as the pressure, microwave power and RF biasing of the substrate holder, have on the films composition, deposition rate and optical properties are discussed. The plasma breakdown products are investigated by studying the plasma's optical emission and taking quadrupole mass spectrometer measurements. The Chapter concludes with a brief review of the applications these films were used for during the course of this thesis.

II-2 Changing the gas flow ratio

II-2.1 Silicon dioxide

To study what would be the ideal deposition conditions for silicon dioxide, a series of films were deposited at different silane gas flows, while initially keeping the pressure and microwave power constant at 1.5 mTorr and 1 kW, respectively. The system was pumped to a base pressure of less than $1 \cdot 10^{-6}$ mBar before all depositions. The substrate was not intentionally heated, nor was an RF bias applied to the substrate holder for the purpose of investigating the influence of

the silane flow. An O_2 flow of 40 sccm was used as it ensures that there is not an excess of silane (though this question requires a separate discussion and will be delt with later), even at the highest flow used in this study, as this may lead to non-stoichiometric films or porous films [1]. In order to achieve the highest possible deposition rate, the precursors are not diluted. Stoichiometric silicon dioxide films with index values matching that of thermal silica (~1.46 at 2 eV) were deposited with rates exceeding 2 nm/s[2]. Figure II-1 *(a)* and *(b)* shows TEM images of a SiO_2 film grown in the reactor *Venus*.

(a)

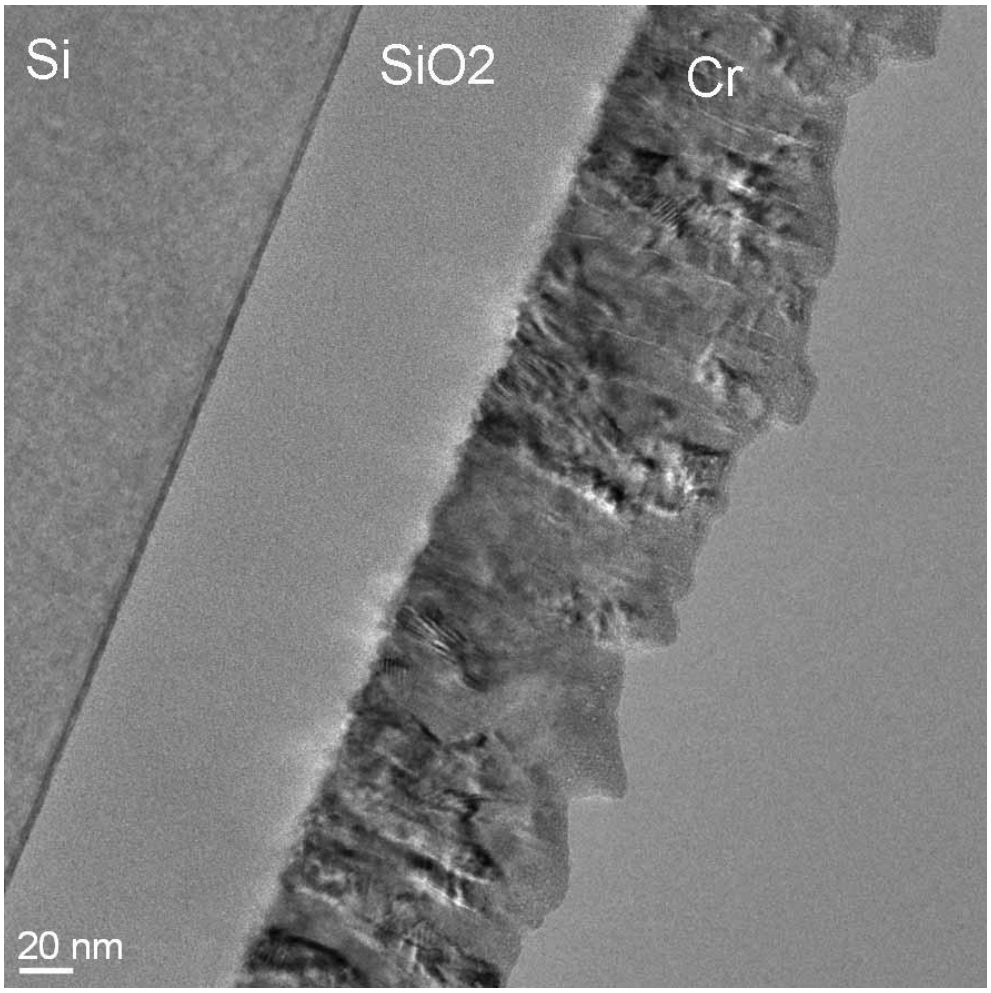

(b)

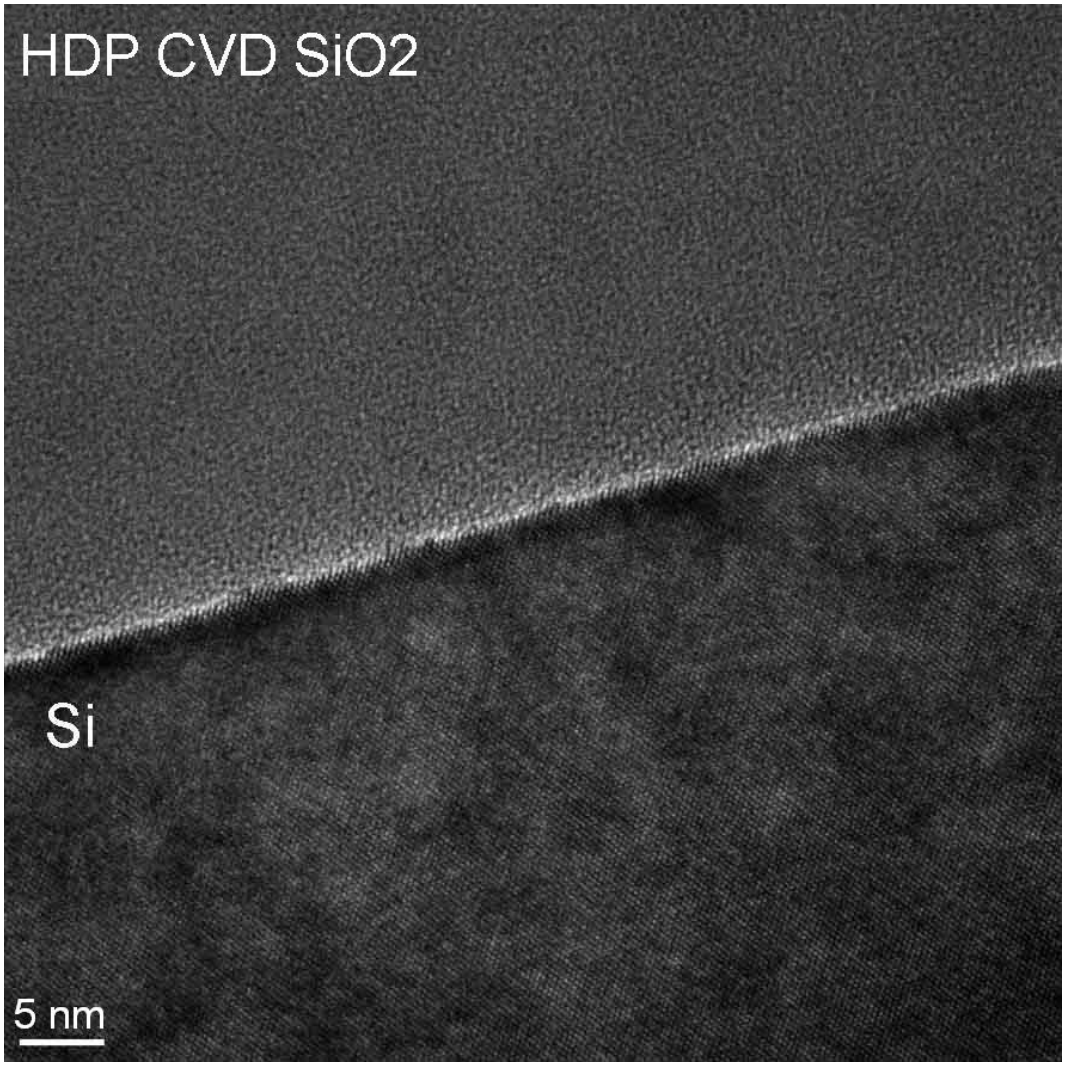

Figure II-1. TEM images of an MDECR PECVD deposited 100 nm SiO_2 film, with an enlargement of *(a)* 60 000 times and *(b)* 360 000 times.

The deposition was done using a 10 sccm SiH_4 and 40 sccm O_2 gas mixture with 1 kW microwave power and a pressure of 2 mTorr. No RF substrate bias was applied during the deposition. The images show the perfect glassy amorphous structure of the film, with no evidence of a columnar structure or phase separation.

The refractive index and deposition rate of the samples deposited at different silane flow rates were obtained from the spectroscopic ellipsometry measurements and are shown in Table II-1. As the silane flow increases, the deposition rate increases, as the process is limited by the silicon precursor delivery [3,4].

The density of silica films can be estimated using the Lorentz-Lorentz formula [5-8] if the composition of the sample is considered to be basically constant. It is given by

$$\rho = K \frac{\left(n^2 - 1\right)}{\left(n^2 + 2\right)} \qquad \textit{(II-1)}$$

For thermal oxide grown at 920 °C the constant *K* is equal to 8.1145 [5,6], where the material's refractive index taken at 1.96 eV is 1.465 and the density ρ is equal to 2.25 g·cm^{-3}. As can be seen from Table II-1 the films deposited with different silane gas flows have refractive indices at 1.96 eV that are all close to that of the thermal silica value quoted above.

SiH_4 gas flow [sccm]	$SiH_4/(O_2+ SiH_4)$ flow ratio	Refractive index at 1.96 eV	Deposition rate [Å/s]
3	0.070	1.464	1.5
5	0.111	1.460	2.7
7	0.149	1.456	3.9
10	0.2	1.456	5.6

Table II-1. Refractive index and deposition rate of silica depositions done at different silane flows.

FTIR measurements were made on the different silane flow samples, as shown in Figure II-2. The Si-H absorption bands in the 650 cm^{-1} (wagging) and 2100 cm^{-1} (stretching) vicinity, the OH band peaks at 950 cm^{-1} and in the 3200 – 3700 cm^{-1} region that has been observed in silica films deposited from argon diluted precursors[9] or nitrous-oxide instead of oxygen[10] and H-O-H band at 1650 cm^{-1} could not be observed in any of the films deposited in this study, leading us to conclude that the hydrogen impurity is below the detection limit[11] discussed in chapter I. There is thus a low level of silanol incorporated into the films. A large quantity of silanol can cause films to be porous and can lower the refractive index[12]. As the hydrogen impurity level in the films is thus very low and the refractive index value is close to the thermal silica value, it can be concluded that the deposited silica films have densities comparable to values shown in literature[13] of 2.2 g/cm^3, for the investigated silane flow regime.

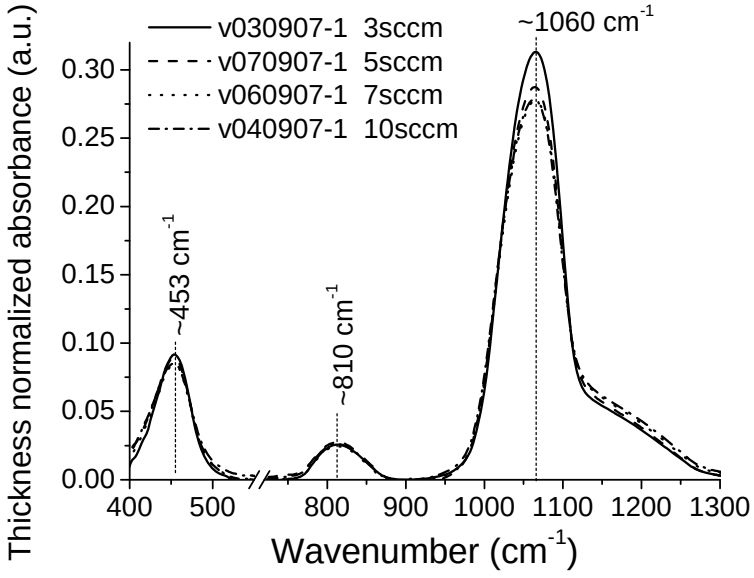

Figure II-2. Thickness normalized IR spectra showing the Si-O rocking, bending and stretching peaks, for depositions done with different SiH_4 flows.

The IR spectra seen in Figure II-2 were deconvoluted into their constituent absorption bands, as shown in Figure II-3. Table II-2 contains the peak frequencies extracted from the deconvoluted spectra of the different depositions. The positioning of the absorption bands remain constant with changes in the SiH_4 flow rate, with the exception of the 1180 cm^{-1} stretching peak that undergoes a slight shift to lower wavenumbers with increased silane flow. Thermal silica has a Si-O asymmetric stretching peak frequency in the vicinity of of 1075 cm^{-1} [14,15]. Shifts or deformation of the stretching peak from the thermal silica value are due to the variations of the Si-O-Si bond angle, and the composition of SiO_x deposition is also directly related to the stretching frequency. The shift to lower wavenumbers can also indicate a slightly less dense material than thermal silica.

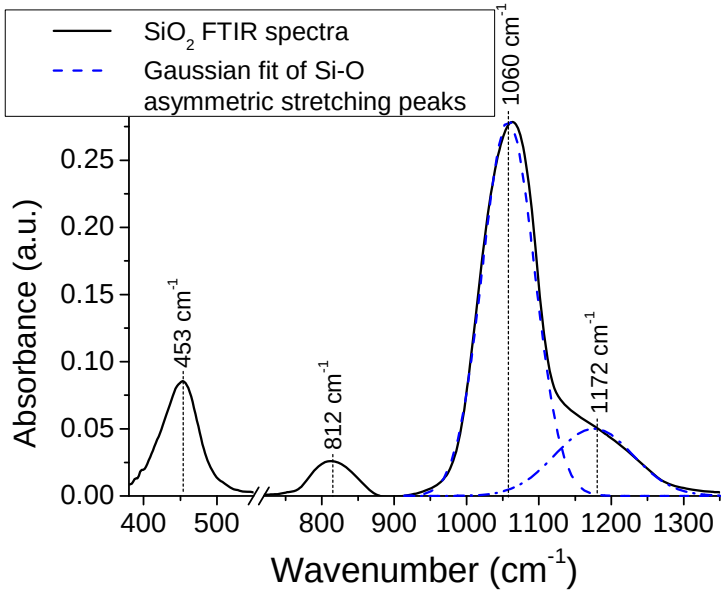

Figure II-3. Positioning of the rocking, bending and deconvoluted Si-O stretching peaks.

Vibration type	Peak frequency [cm^{-1}]				
	3 sccm	5 sccm	7 sccm	10 sccm	Thermal SiO_2 [15]
Si-O (Rocking)	453	453	453	453	450
Si-O (Bending)	814	813	814	812	800
Si-O (Stretching)	1060	1059	1059	1060	1075
Si-O (Stretching)	1180	1177	1176	1172	1180

Table II-2. Changes in the peak frequencies of silica films deposited at different silane flows and 40 sccm oxygen flow.

Table II-3 contains the peak amplitude and full width at half maximum values for the main Si-O stretching peak in the 1075 cm^{-1}. A slightly narrower peak at low silane flows can be seen, which indicates a marginally better ordering in the film[16]. Increasing the silane flow reduces the Si-O peak amplitude. This is due to a slight decrease in the Si-O-Si bond angle and thus a slight decrease in the density of the films [5]. The density thus decreases as the silane flow rises, which is confirmed by the lowering in refractive index which was shown in Table II-1.

SiH_4 flow [sccm]	Peak amplitude [a.u.] (± 0.2)	FWHM [cm^{-1}] (± 0.5)
3	31.2	69
5	29.1	71
7	27.9	71.6
10	27.8	72

Table II-3. Changes in the Si-O asymmetric stretching peak amplitude and FWHM values of SiO_2 films deposited at different SIH_4 flows.

The film composition discussed above can be linked to the plasma properties and the gas phase composition observed during similar plasma conditions as the silane gas flow series that was deposited. Figure II-4 and II-5 shows the OES and QMS measured data. The intensity of the hydrogen Balmer line, H_α, rises with increasing silane flux, as it is a silane and water fragmentation product [17], as shown in Figure II-4. The production of water also increases as it is the main by-product during the deposition of SiO_x from a silane and oxygen gas mixture.

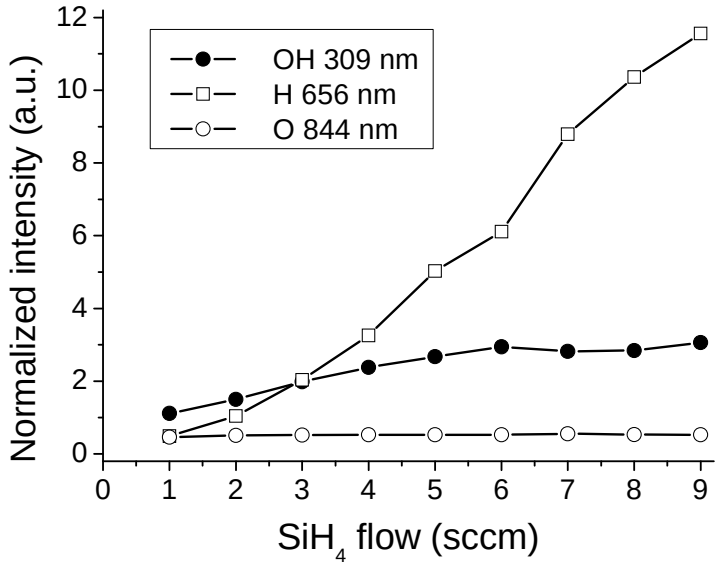

Figure II-4. OH, O and H_α Optical emission intensities for varying silane gas flows, at 1 kW microwave power, 1.5 mTorr pressure, 40 sccm O_2, 3sccm Ar.

The mass spectrometry measurements shown in Figure II-5 depict the increase in the fraction of silane and oxygen used during deposition, with increasing silane flow. The normalized intensity here refers to the ratio of the O_2^+ or SiH_2^+ ion intensity when a deposition plasma exists in the reactor chamber, to its intensity

without a plasma (in other words, when no silane or oxygen consumption is taking place).

The O_2^+ intensity shows an almost linear decrease with rising silane flow, due to a greater availability of silicon bonding sites and higher water production [18]. The decrease in SiH_2^+ normalized intensity start to saturate at higher flow rates. At the moment no explanation for the high consumption of SiH_4 at high SiH_4 flow rates can be given. A distinct difference in the scales of the O_2^+ and SiH_2^+ intensities can be seen, due to the fact that the silane is almost entirely consumed while the excessive oxygen is fed to the chamber in order to guarantee stoichiometric SiO_2 deposition.

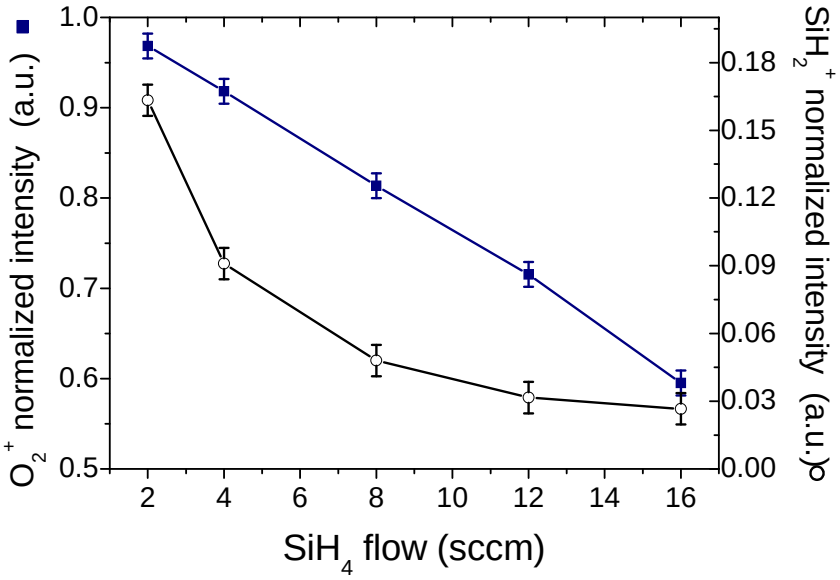

Figure II-5. Mass spectrometry measurements of O_2^+ and SiH_2^+ intensities during a plasma discharge, normalized with respect to measurements taken without a discharge, at different silane flows.

II-2.2 Silicon nitride

A series of SiN_X films were deposited at different silane flows and ellipsometric measurements used to determine the refractive index and deposition rates, as can be seen in Table II-4. As was the case with the silicon oxide films, the deposition rate increases as the silane flow is increased, again due to the process being limited by the silicon precursor delivery [20,21]. The decrease in refractive index of the SiN_x films when raising the silane flow is not reported in studies using NH_3 or He diluted N_2 as oxidizing precursor [21,22]. The SiH_4/N_2 mixture used here, results in a larger quantity of hydrogen being incorporated into the growing film as the silane flow is increased. This statement will be discussed together with the FTIR results shown in Figure II-4 for the different SiN_x films.

SiH_4 gas flow [sccm]	Refractive index at 2 eV	Deposition rate [Å/s]
3	1.855	1.2
5	1.790	2.1
7	1.767	3.1
10	1.735	4.7

Table II-4. Refractive index and deposition rate of SiN_x depositions done at different silane flows.

The IR spectra seen in Figure II-6 were deconvoluted into their constituent absorption bands that were discussed in Chapter I, as shown in Figure II-7. The main absorption in the 700 to 1200 cm^{-1} wavenumber range, consists of the Si-N

stretching vibrations and the Si-NH-Si bending vibration. A Si-H_2 stretching mode at 2090 cm^{-1} that has been seen in ECR-PECVD SiN_x films deposited using He dilution[21] was not be observed in this study. The absence of the Si-H peak at 2100 cm^{-1} is due to the nitrogen rich conditions used during all the deposition, leading to a preferred creation of the N-H bonds at ~3300cm^{-1} [23].

The presence of Si-O bonds is not excluded, as depositions are done at room temperature and some oxygen present in the system due to the history of depositions could be incorporated. The system was however pumped for at least two hours before each SiN_x deposition to reduce the oxygen contamination.

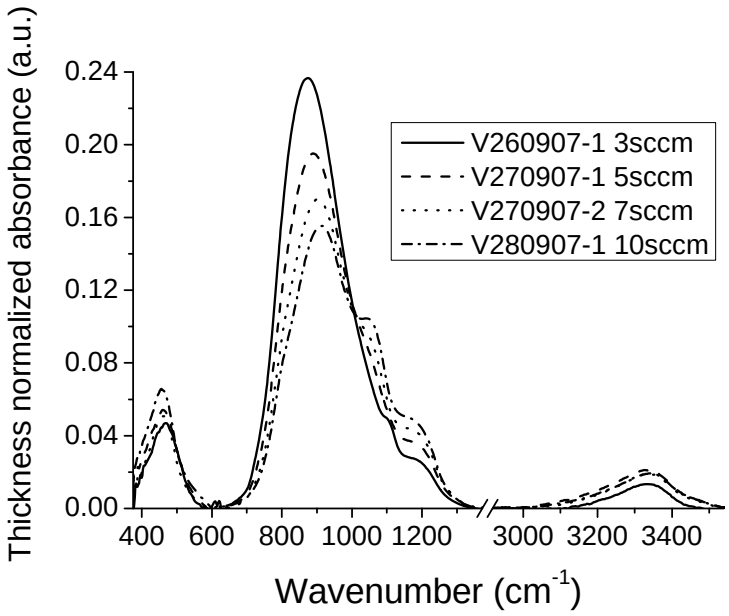

Figure II-6. Thickness normalized IR absorbance spectra for depositions done at different SiH_4 flows.

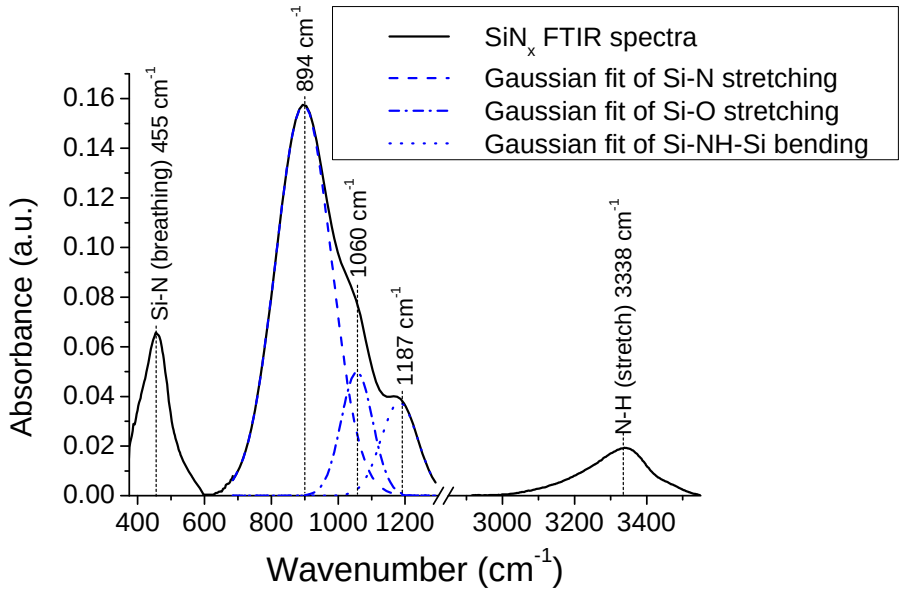

Figure II-7. Deconvoluted FTIR spectra of a silicon nitride deposition.

Table II-5 contains the Si-N stretching peak frequencies, amplitudes and FWHM values extracted from the deconvoluted spectra of the different SiN_x depositions. An increase in the FWHM values of the films deposited at higher silane flows is due to less ordering in the films.

The lowering in peak amplitude of the Si-N stretching peak and a simultaneous increase in the NH bonds as shown in Figure II-6, indicate a higher hydrogen content in the films deposited at higher silane flows. This confirms the statement made earlier that a decrease in the refractive index values with higher silane flows indicates an increase in the hydrogen incorporation. The shift in the peak frequency of the Si-N absorption band and the strengthening of the Si-NH-Si peak on Figure II-6 also confirm that the quantity of hydrogen incorporated into the silicon nitride films is dependent on the silane gas flow, and that the hydrogen

is preferentially bonded to nitrogen, as the Si-H peak is absent. Other researchers consider this preferential bonding to be due to hydrogen bonding to nitrogen in the gas phase [21]. It is more probable that hydrogen is removed from the growing surface via the creation of NH_3 molecules, which form strong physisorption bonds* that have a bonding energy of 0.63 eV [24].

SiH4 flow [sccm]	Peak amplitude [a.u.] (± 0.6)	FWHM [cm^{-1}] (± 2)	Peak frequency [cm^{-1}]
3	21.2	113	858
5	17.8	141	870
7	16.0	162	894
10	15.5	166	896

Table II-5. Changes in the peak frequencies, amplitude and FWHM of Si-N peaks in SiN_x films deposited at different silane flows.

In Figure II-8 QMS measurements of the N_2^+ and SiH_2^+ ions can be seen. Similar to the SiO_2 case, an increase in the fraction of silane and nitrogen used during deposition can be observed when increasing the silane flow. The silane precursor consumption is however very high over the entire gas flow range investigated, though still less than when depositing SiO_2. This is logical due to the higher reactivity of oxygen. The N_2^+ normalized intensity shows the fraction of nitrogen consumed changing much more drastically as larger silane flows are added.

* A strong smell of ammonia can also be perceived in the system after depositing silicon nitride, amd even after pumping the system to below 1e-6 mBar after deposition.

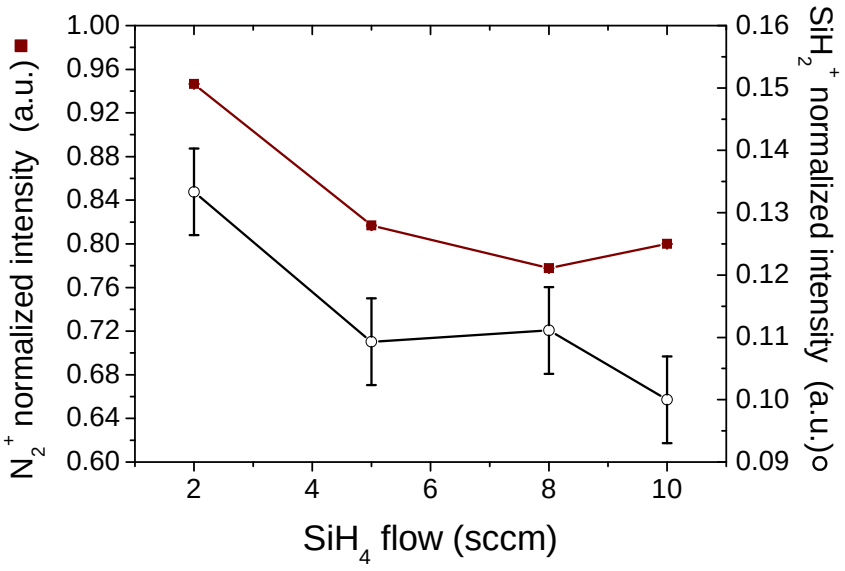

Figure II-8. Mass spectrometry measurements of N_2^+ and SiH_2^+ intensities during a plasma discharge, normalized with respect to measurements taken without a discharge, at different silane flows.

II-2.3 Silicon oxynitride

Figure II-9 shows the optical index dispersion curves of a series of SiO_xN_y films deposited using 5 sccm SiH_4 and an 80 sccm O_2+N_2 gas flow. The ratio $O_2/(O_2+N_2)$ was varied from 0 (pure SiN_x) to 0.25, which constitutes an oxygen rich SiO_xN_y. 1 kW microwave power and 2 mTorr pressure were used in all depositions.

Figure II-10 shows the refractive index and deposition rate data as a function of the $O_2/(O_2+N_2)$ gas ratio, for both 5 sccm and 10 sccm SiH_4 gas flows [25]. The refractive index can be varied precisely by varying the precursors ratio over a

broad range of values, from SiO_x to SiN_x, which makes these films ideal for depositing optical filters [26].

Since the oxidizing potential of oxygen is higher than nitrogen, a ratio of 0.1 for a 5 sccm silane flow is enough to produce an oxynitride with a refractive index and deposition rate close to that of pure silicon dioxide. The 10 sccm silane flow leads to a silicon nitride film with a refractive index that is lower than the 5 sccm case due to higher hydrogen content.

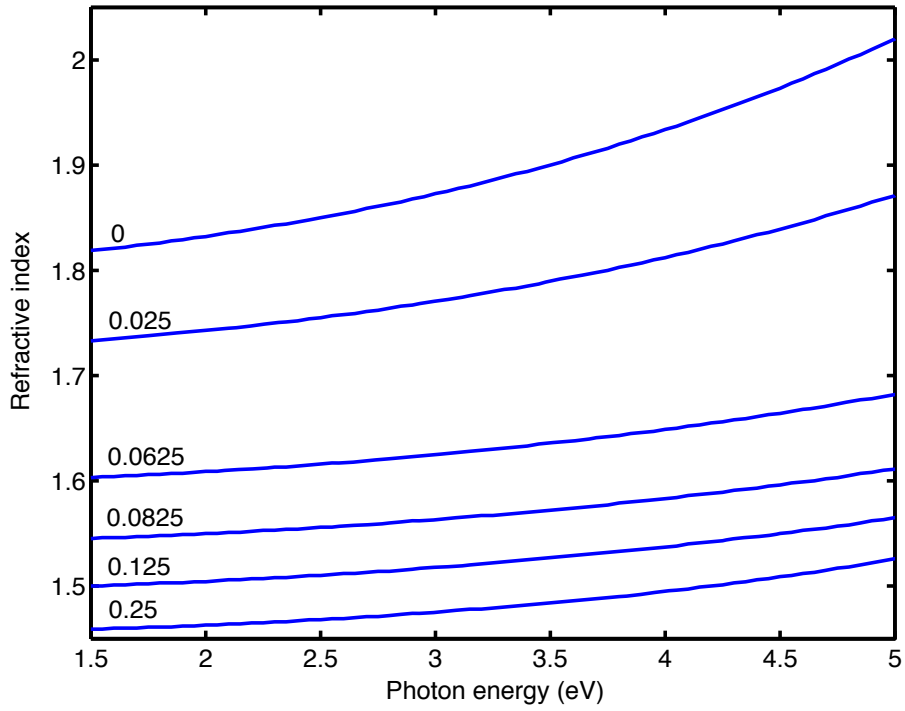

Figure II-9. Optical dispersion curves for SiO_xN_y films deposited at different $O_2/(O_2+N_2)$ flow ratios.

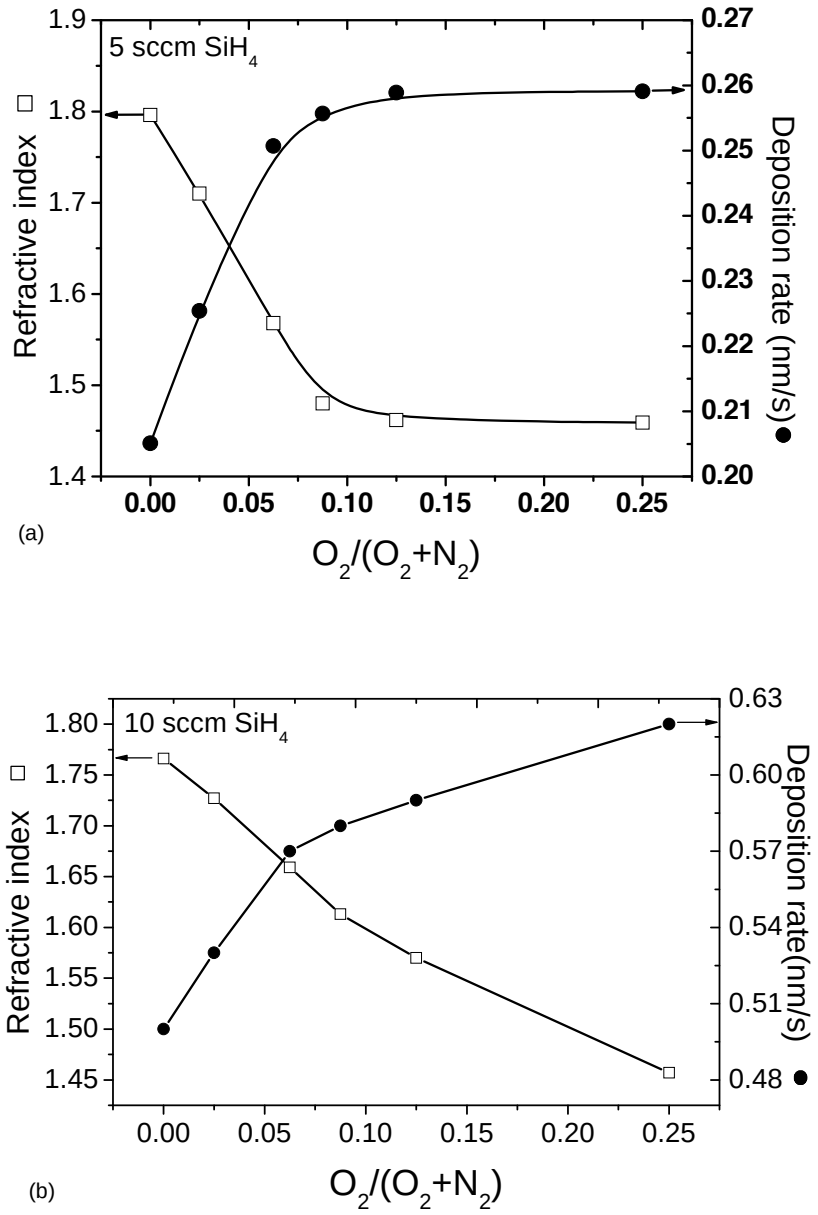

Figure II-10. Refractive index and deposition rate as a function of the oxidants flow ratio, for *(a)* 5 sccm SiH_4 and *(b)* 10 sccm SiH_4 gas flows.

FTIR measurements of the various oxidant ratio films shown in Figure II-10 *(a)* can be seen in Figure II-11. The shift from the Si-N stretching peak at an oxidants ratio of 0 to the Si-O stretching peak at the oxidants ratio 0.25 is apparent.

It is interesting to observe that at a 0.25 oxidants ratio the material already exhibits almost the same FTIR spectra and refractive index as the silicon oxide material shown in Section II-2.1. As the oxygen molecules have a lower dissociation energy than the nitrogen molecules, more atomic oxygen than nitrogen will link with the silicon atoms at the growing surface[10,14,27].

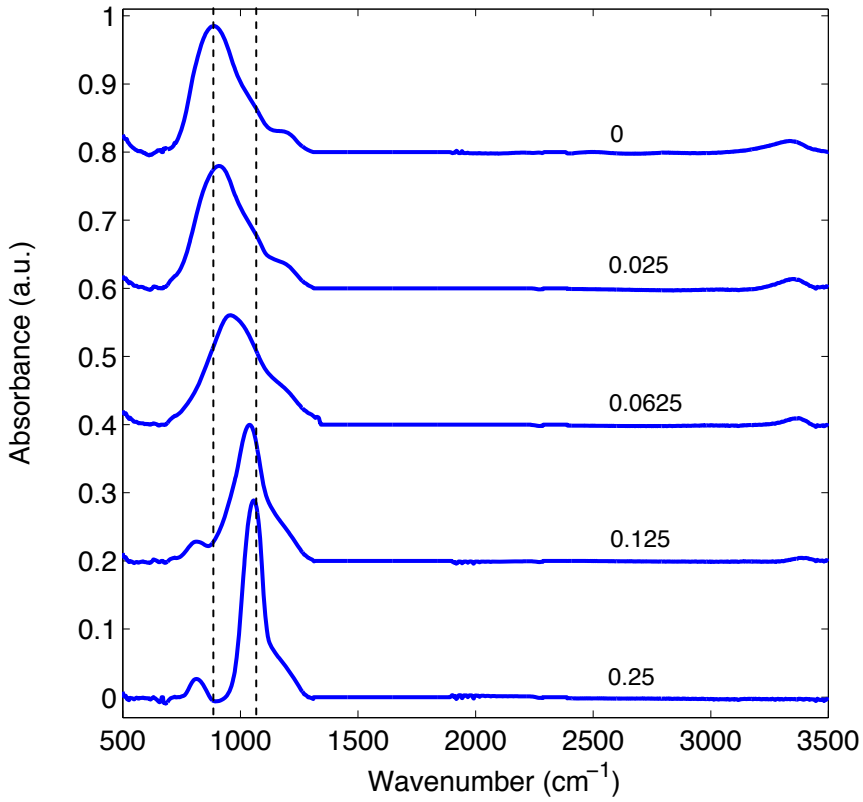

Figure II-11. FTIR absorption spectra for SiOxNy filmd deposited at different $O_2/(O_2+N_2)$ flow ratios with 5 sccm SiH_4, 1 kW microwave power and 2 mTorr pressure.

II-3 The influence of the applied microwave power

A series of depositions were done in order to study the influence of the microwave power on the quality of the silicon oxide films[28]. Gas flows of 5 sccm SiH_4 and 40 sccm O_2 were used, with 3 sccm Ar added for actinometry purposes. The process pressure was set to 2 mTorr for all depositions, and no RF biasing or intentional heating of the substrate holder was used. Figure II-12 shows the FTIR measurements of films deposited with the microwave power varied from 500 W to 1500 W, while the OES measurements of the plasma emission and the QMS residual gas measurements results can be seen in Figures II-13 and Figure II-14.

The FTIR results indicate a slight increase in the Si-O stretching peak intensity when the deposition is done with a high microwave power. From the optical emission shown in Figure II-13 *(a)* it is found that the atomic oxygen emission in a SiH_4/O_2 plasma at 844 nm remains constant with increased microwave power. To get a better insight into this phenomenon the oxygen emission in an O_2 plasma (with 3 sccm Ar) was also analyzed, as shown in Figure II-13 *(b)*. Here, the oxygen radical emission does in fact increase linearly with increased power. It can be concluded that the additional atomic oxygen generated with increased microwave power in the SiH_4/O_2 gas mixture is consumed during the deposition. This will in turn lead to an increase in the deposition rate.

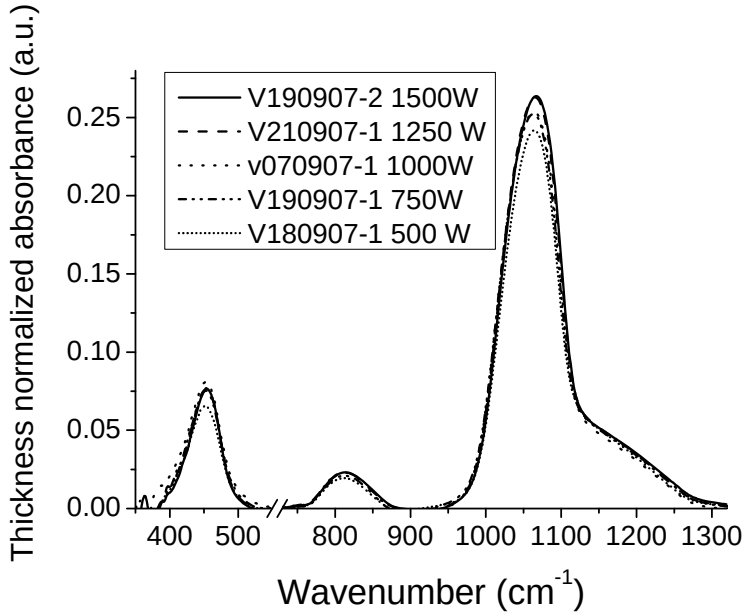

Figure II-12. Thickness normalized IR absorbance spectra for SiO_x depositions done with assorted microwave powers.

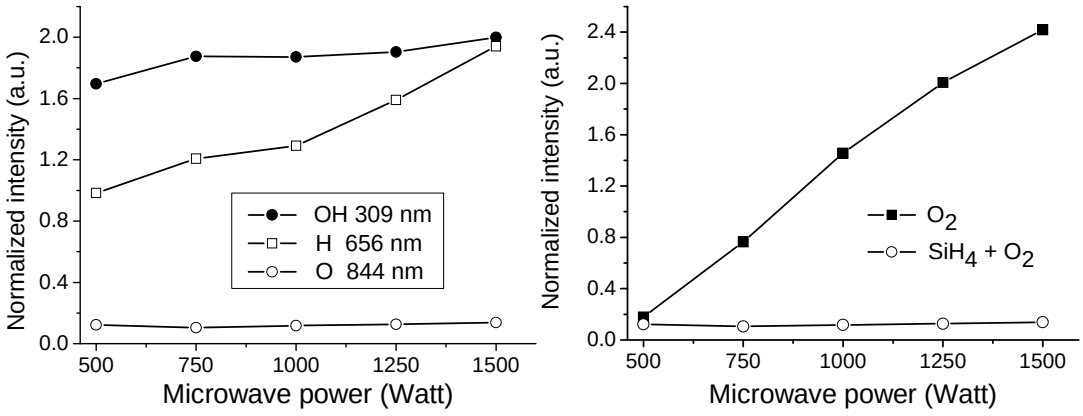

Figure II-13. *(a)* OH, O and H_α optical emission intensities for varying microwave powers, at 1.5 mTorr pressure,5 sccm SiH_4, 40 sccm O_2 and 3sccm Ar. *(b)* O emission intensities with varying microwave powers, both with and without silane in the gas mixture.

The OES results in Figure II-13*(a)* also show a marked rise in the hydrogen emission at 656 nm due to the more effective breaking of the H_2O and SiH_4 molecules with increased microwave power, as well as an increase in the hydroxyl emission system at 306.4 nm with increased microwave power. As a consequence of this, one might expect to see a lowering in the hydroxyl content in the deposited film with increased microwave power, which will be elaborated on in Chapter III. The QMS measurements seen in Figure II-14 show an excellent consumption of the silane precursor even at low microwave powers, as well as a slight rise in the oxygen consumption as higher microwave power is used. The H_2O intensity peak at m/z = 18 was found to follow a trend similar the OH emission shown in Figure II-13*(a)*, as is also reported when using a tetraethoxysilane/oxygen gas mixture[18].

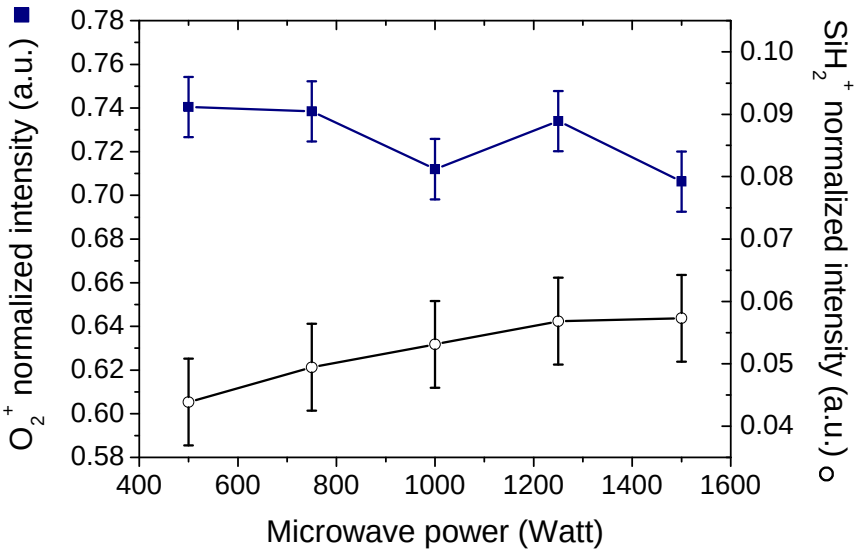

Figure II-14. Mass spectrometry measurements of O_2^+ and SiH_2^+ intensities during a plasma discharge, normalized with respect to measurements taken without a discharge, at different microwave powers.

Three SiN_x films were deposited at 600 W, 1000 W and 1400 W, respectively. The refractive index that can be seen in Figure II-15 is found to increase considerably with increased power, while the deposition rate decreases. This can be attributed to the SiN_x films being denser at high powers. This might be due to an increased removal of NH_3 from the surface due to N_2^+ bombardment and the higher temperature of the surface at increased microwave powers. The increase in the density of the material then leads to the observed rise in the refractive index. The densification assumption is confirmed by the infrared spectra shown in Figure II-16, where it can be seen that the Si-N peak gains intensity, shifts towards lower wavenumbers and becomes narrower with increased power. The mass spectrometry measurements seen in Figure II-17 show very small variations in the SiH_2^+ normalized intensities and a slight improvement in the N_2^+ consumption, pointing to an almost complete utilization of the silane precursor even at low microwave powers, as evidenced by the deposition rates as well [4].

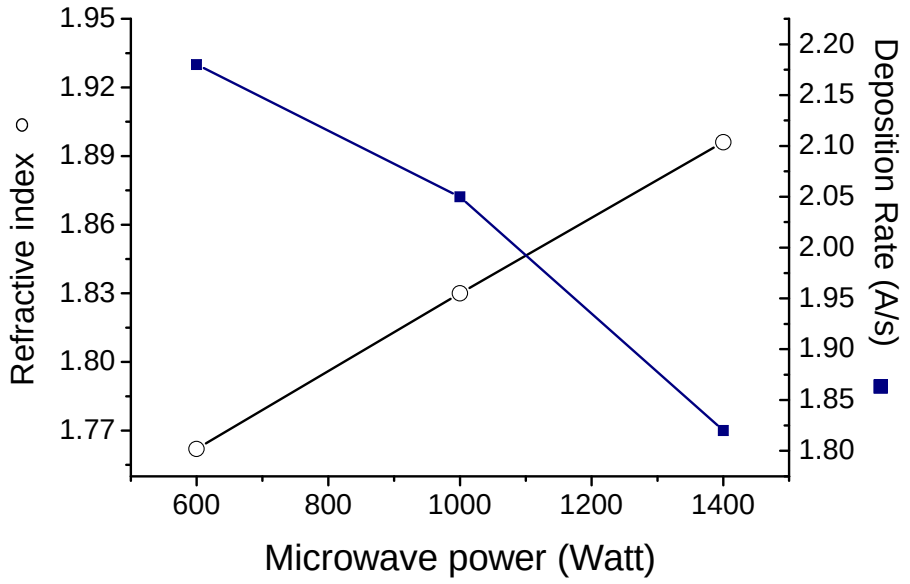

Figure II-15. Refractive index and deposition rates for SiN_x films deposited at different microwave powers.

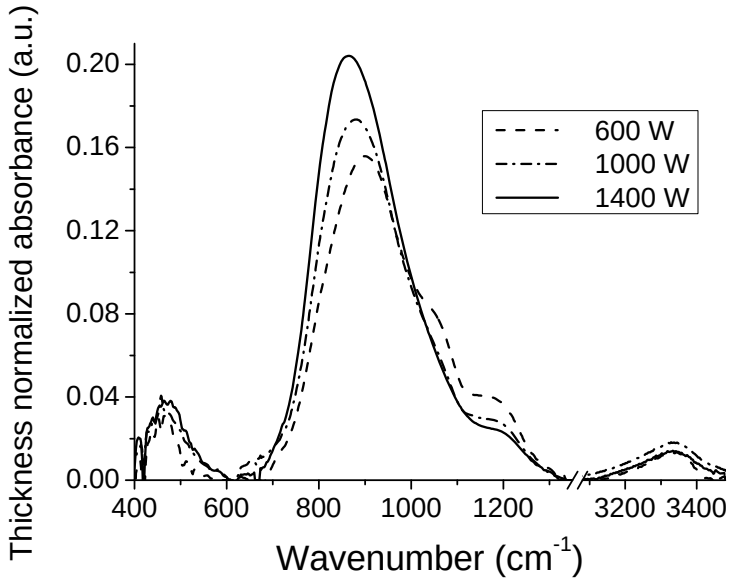

Figure II-16. Thickness normalized IR absorbance spectra for SiN_x depositions done with assorted microwave powers.

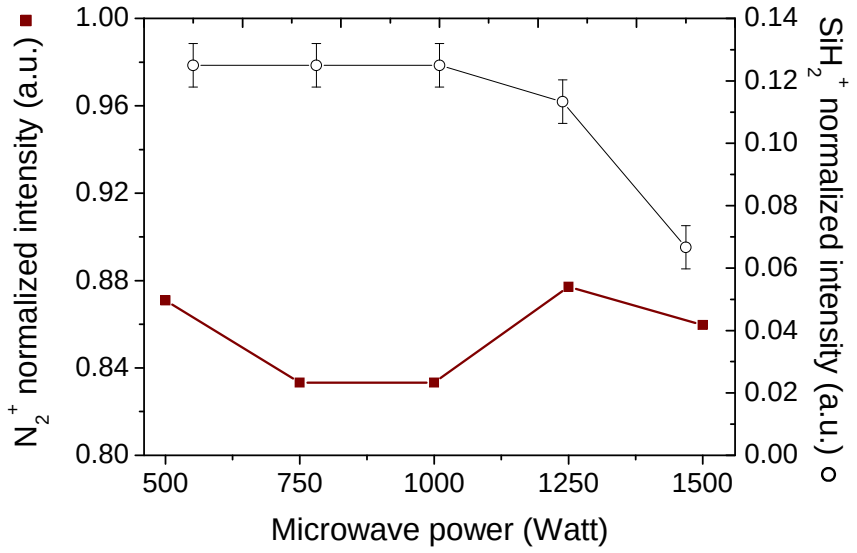

Figure II-17. Mass spectrometry measurements of N_2^+ and SiH_2^+ intensities during a plasma discharge, normalized with respect to measurements taken without a discharge, at different microwave powers.

II-4 Process pressure and substrate heating

Figure II-18 shows the dependence of the refractive index of an oxynitride deposition on the oxidants flow ratio, for a SiH_4 flow of 5 sccm and two different pressures. The pressure is found to have only a minor influence and the index is mainly controlled by the gas flow ratio. The OES measurements seen in Figure II-19 also show that the investigated pressure range does not have a strong influence, except for a slight rise in the OH emission intensity when the pressure is increased up to 8 mTorr. It must be noted here that the pressure was regulated by closing the gate valve, thus reducing the effective pumping rate of the turbomolecular pump. The influence of pressure changes was investigated using QMS measurements of the silane and oxygen consumption between 1 and 3 mTorr, as seen in Figure II-20. A negligible change in the silane consumption and a very slight decrease in the oxygen utilisation with rising pressure are observed.

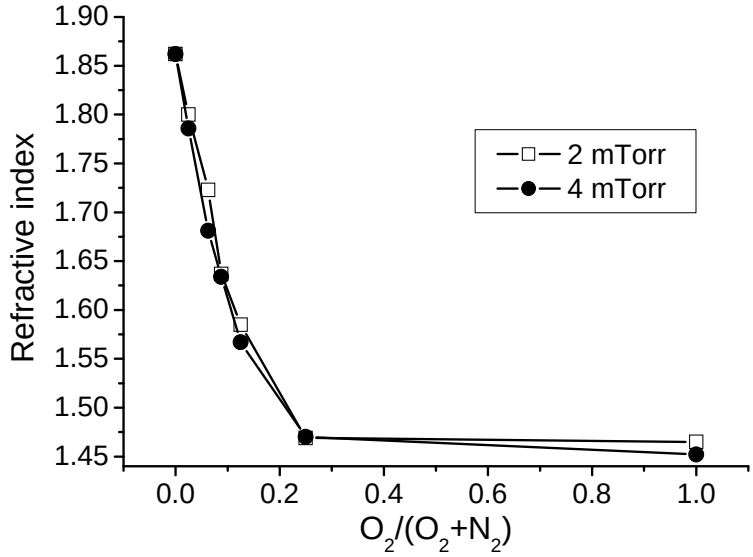

Figure II-18. Refractive index at different $O_2/(O_2+N_2)$ gas flow ratios.

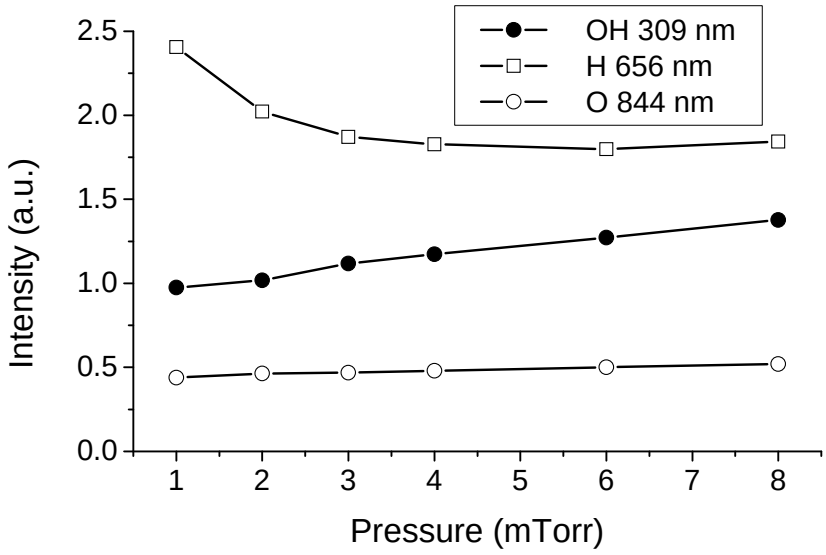

Figure II-19. O, OH and H normalized optical emission of a 5 sccm SiH_4, 40 sccm O_2 and 3 sccm Ar gas mixture at varying pressure.

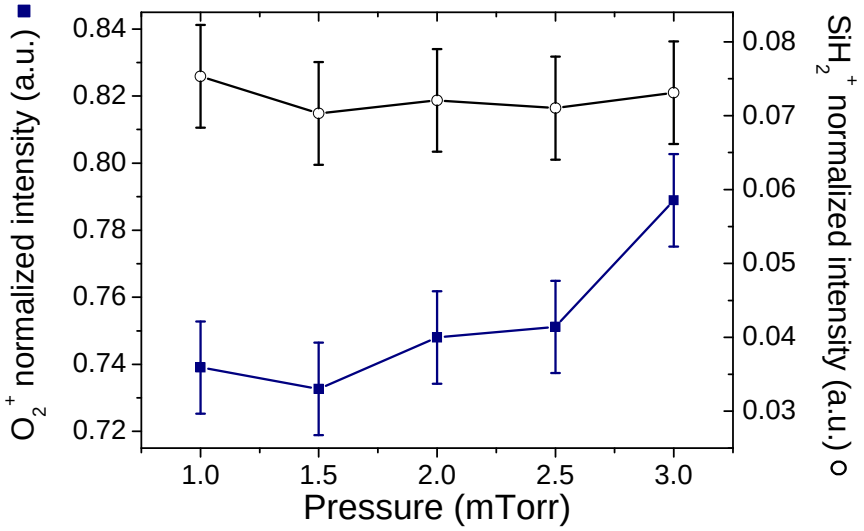

Figure II-20. Pressure dependence of the O_2^+ and SiH_2^+ intensities.

As this study is mainly concerned with the deposition of silicon oxide without intentional heating of the substrate holder, a very brief discussion of the influence of heating the substrate holder is given here. Table II-6 shows the deposition rate and refractive index of two depositions, one done with heating the substrate

holder to 150 °C and one with no intentional heating. The deposition rate decreases with increased substrate temperature, which could be due to changing gas concentrations (as the heating of the gas will lead to a decrease of its density at a constant pressure) or a decrease in the residence time of the SiH_4 on the substrate surface. The FTIR measurements in Figure II-21 also show that the two depositions have a very similar composition, with the film heated during deposition having only a slightly narrower peak. This points to a slightly better ordering in the film.

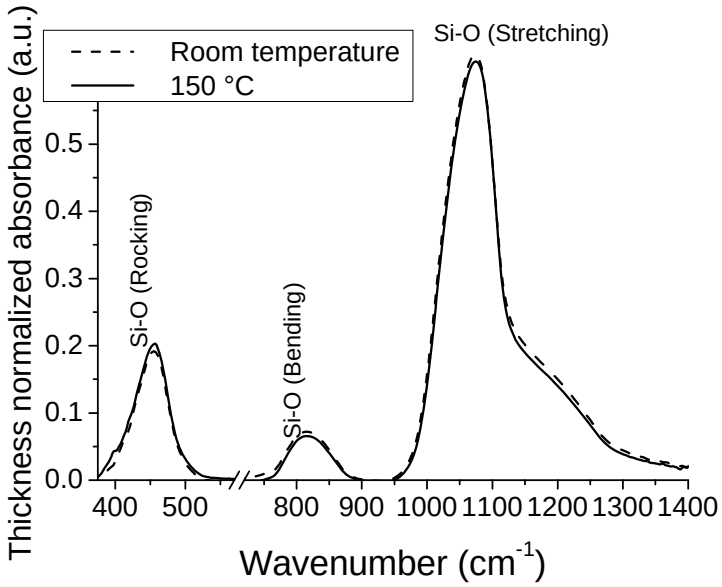

Figure II-21. IR spectra of SiO_2 deposited at room temperature and 150 °C.

Substrate temperature	Deposition rate (Å/s)	Refractive index (2eV)
Unheated	6.3	1.461
150°C	5.2	1.46

Table II-6. Deposition rate and refractive index of silicon dioxide (10 sccm SiH_4, 40 sccm O_2) deposited on heated and unheated substrates.

II-5 Radio frequency biasing of the substrate holder

The influence of applying an RF bias to the substrate holder was investigated by FTIR measurements done on three silica films deposited with different bias voltages[28], as presented in Figure II-22.

The Si-O-Si stretching peak was found to shift from 1074 cm^{-1} when no bias was applied to 1080 cm^{-1} at a -50V substrate bias, due to compressive stress developing in the film, which has also been reported in other studies [29]. The slight narrowing in the peak with increased substrate biasing is due to better ordering in the film. No Si-H bonds were observed in the vicinity of 2100 cm^{-1} in all spectra.

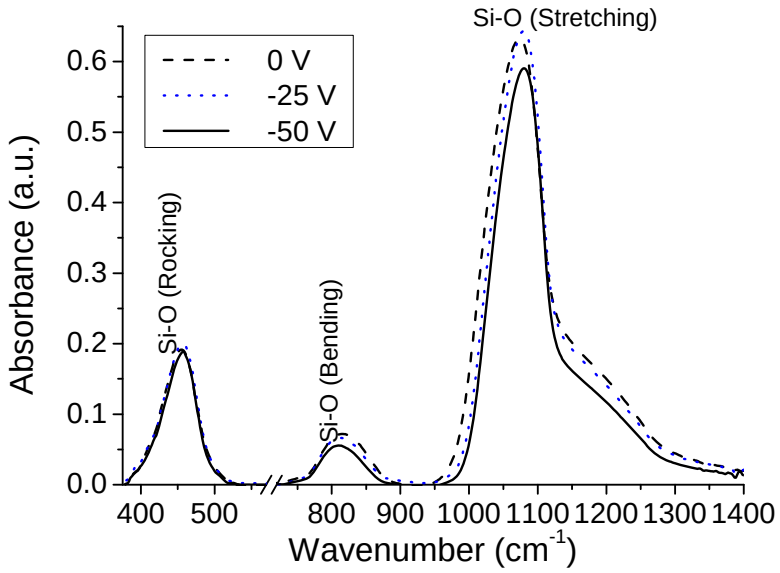

Figure II-22. Infrared spectra of three SiO_2 films deposited at 0 V, -25 V and -50 V substrate bias, respectively.

The OES measurements shown in Figure II-23 demonstrate a distinct increase in the hydroxyl emission, which might indicate efficient removal of the water symmetric feature (the associated SiOH vibration mode) from the deposition surface, due to the increased bias voltage that results in a higher ion energy and flux. The QMS measurements that can be seen in Figure II-24 show an increased consumption of the silane precursor, evidenced by the reduced intensity of the SiH_2^+ normalized intensity, when a low RF substrate bias is applied. There is a slight decline in the quantity of oxygen consumed when the substrate bias is increased. This can be explained by the increased ion bombardment energy caused by raising the substrate bias. The threshold for physical sputtering of thermally grown SiO_2 in an oxygen plasma has been found to be 25V [30]. A too high substrate bias will thus lead to physical sputtering, as also found by other researchers [31-33]. A low RF substrate bias thus contributes to the deposition process by ensuring a high flux of low energy ions and consequently the efficient removal of hydrogen from the growth surface and densification of the film [29].

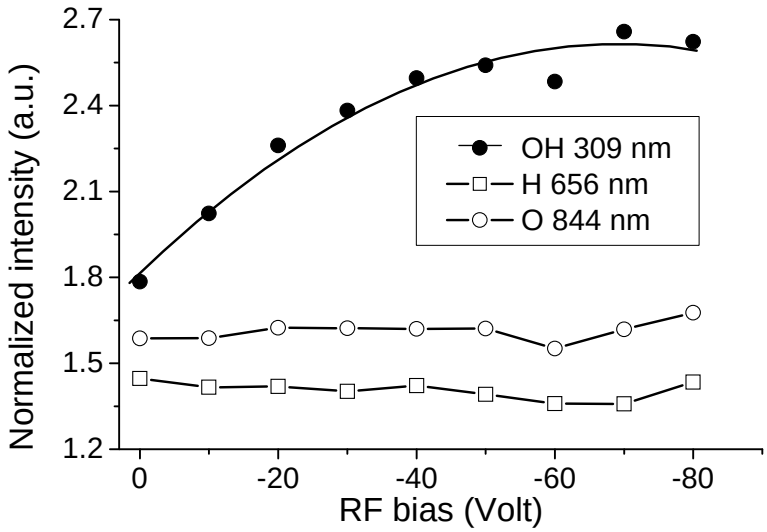

Figure II-23. Changes in the H, OH and O optical emissions as a function of the RF bias applied to the substrate holder.

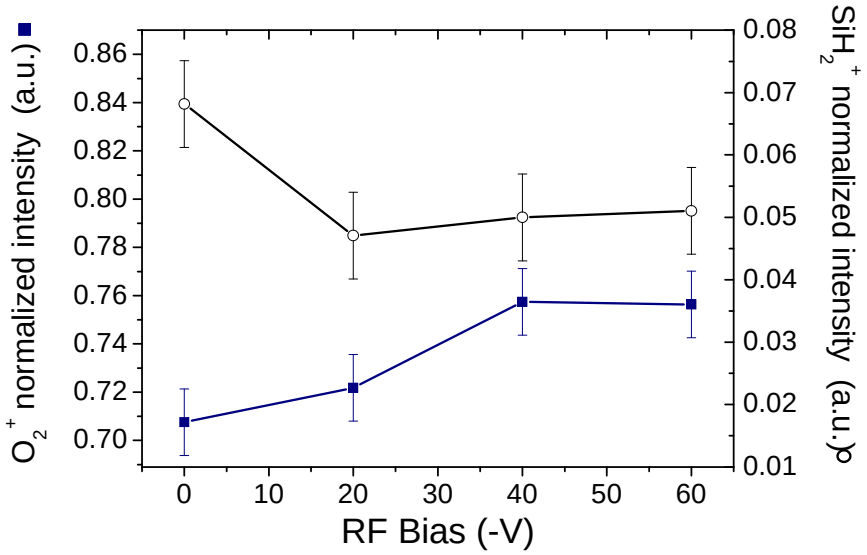

Figure II-24. Mass spectrometry measurements of the O_2^+ and SiH_2^+ ions.

Refractive index values of SiO_xN_y depositions done with a substrate bias of -20V, at both 5 sccm and 10 sccm silane gas flows, are depicted in Figure II-25. The refractive index is found to increase slightly due to the RF bias applied to the substrate holder, which lead to a higher density due to an increase in the energy of the positive ions bombarding the surface[34].

FTIR measurements on silicon nitride depositions done with and without a substrate bias applied are shown in Figure II-26. 2 mTorr pressure, 1 kW microwave power and a 10/80 sccm SiH_4/N_2 gas mixture was used. A significant increase in the Si-N stretching peak with a shift to a lower wavenumber, as well as a reduced N-H stretching peak, indicates the reduced incorporation of hydrogen in the film when applying the substrate bias.

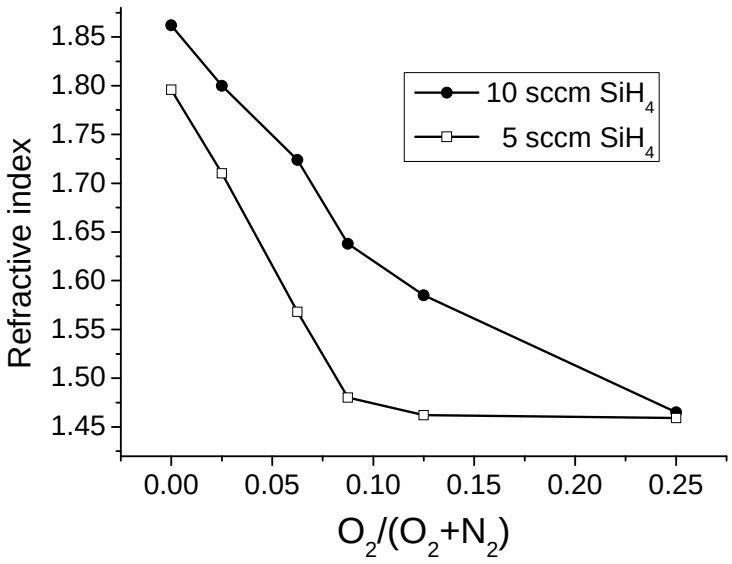

Figure II-25. SiO_xN_y depositions done at different $O_2/(O_2+N_2)$ flow ratios, for 5 sccm and 10 sccm SiH_4 flows.

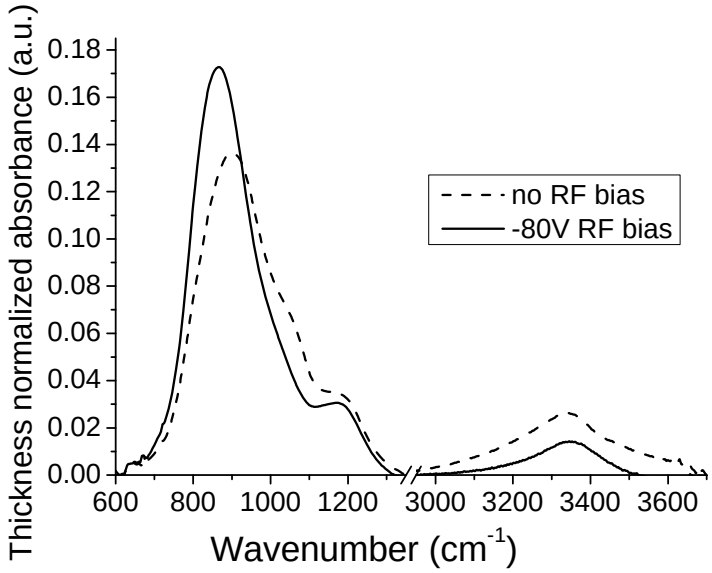

Figure II-26. Infrared transmission spectra of SiN_x depositions done with and without a substrate bias applied.

II-6 Applications

To conclude, a few applications of the parameter study done in this Chapter is presented. The gas flow study in section II-2 on the SiO_x and SiN_x films was used to deposit several filters[26,35]. An example of a 5 cm x 5 cm Bragg mirror's transmission is shown in Figure II-27. The slight discrepancy between the theoretical curve and the measured transmission is due to the refractive index of the deposited SiN_x films being lower than the expected refractive index, since residual oxygen is included in the SiN_x films when alternating the deposition between SiO_2 and SiN_x layers.

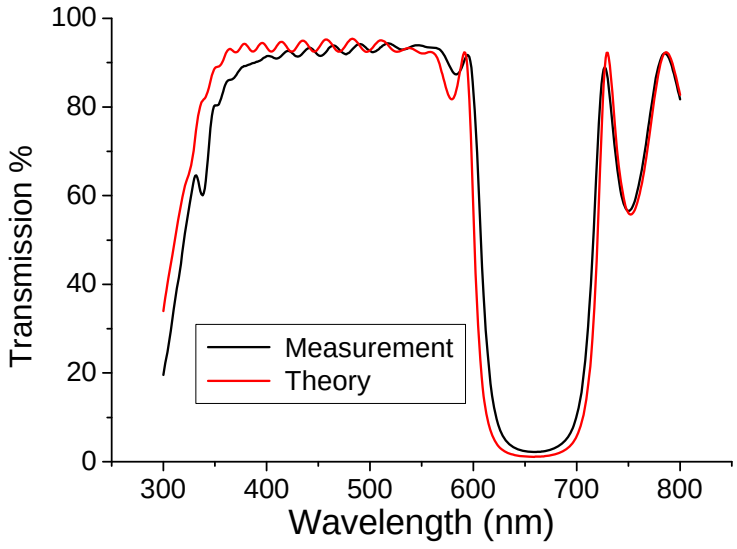

Figure II-27. Transmission of a Bragg mirror at 660 nm deposited on Corning glass[35].

Silicon dioxide and nitride films were deposited as impermeability coatings onto 12μm thick PET substrates in the frame of the ENCAPSAT project. PET has a permanent water flux (or Water Vapour Transmission Rate, WVTR) of 9.8 $g/m^2/day$. As applications such as organic photovoltaïcs or OLEDs require WVTR of the order of 10^{-6} $g/m^2/day$[36], a water barrier coating is required for the PET substrate. In addition to this the melting temperature of PET [36,37] is in the vicinity of 250°C with the glass transition temperature at approximately 80°C, making the use of a low temperature process for depositing the barrier coating essential.

Table II-7 summarizes the results of a series of depositions done, either onto uncoated or titanium coated 12 μm thick PET substrates, as indicated in the table. The Barrier Improvement Factor (BIF) indicated is the ratio of the measured water permanent flux of an uncoated PET substrate to the coated PET's water permeation. A gas mixture of 10 sccm SIH_4 and 40 sccm O_2 was used for the silicon dioxide depositions and an 10 sccm SIH_4 and 80 sccm N_2 mixture for the silicon nitride film. No rf bias was applied to the substrate holder and the substrate holder was not heated intentionally during the depositions.

Sample	Substrate	Material	Microwave power	Thickness	BIF
V250707-1	PET	SiN_x	500 W	530 nm	72
V240707-2	PET	SiO_2	500 W	530 nm	9
V240707-1	PET/Ti	SiO_2	500 W	530 nm	43
V200707-1	PET/Ti	SiO_2	1000 W	531 nm	179

Table II-7. BIFs for SiO_2 and SiN_x depositions done onto PET and Ti-coated PET substrates.

It can be seen that using titanium coated PET improves the BIF significantly. Most likely the 50 nm Ti-layer sufficiently protects the underlying PET from the oxygen plasma and the plasma generated UV light. For the depositions done onto uncoated PET substrates, the best results were obtained with the silicon nitride deposition, which had a BIF of 72. Two 200 nm depositions of SiO_2/SiN_x gradients were done onto uncoated PET substrates, with the material gradually changed from silicon oxide to nitride in the one deposition, and from silicon nitride to oxide in the other. Figure II-28 shows the measured water flux of these depositions, as well as the WVTR of an uncoated PET substrate. The BIF for the two depositions were 3 and 3.5, respectively, which is low compared to the values that were listed in Table II-7.

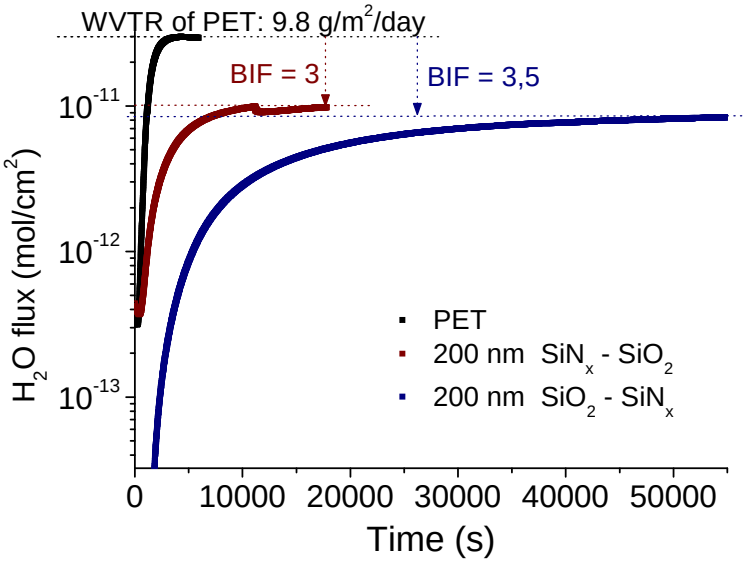

Figure II-28. Water flux measurements for two 200nm SiO_2/SiN_x gradient depositions, with the WVTR of clear PET indicated.

A 320 nm SiO_2 deposition was done using a 5 sccm SiH_4 and 40 sccm O_2 gas mixture and 1.5 mTorr pressure, 1 kW microwave power and -40V RF substrate bias, in order to fabricate an aluminum capacitor test structure for current-voltage measurements. Figure II-29 shows the breakdown field distribution of the fifteen 1.77 x 10^{-8} m^2 capacitor points measured. As can be seen the majority of the points had breakdown fields in the vicinity of 4.1 MV/cm, which is acceptable but still low in comparison with the best values reported in literature [38]. Pinholes in the film, due to the vertical orientation of the reactor chamber (face-up substrate position) leads to dust falling onto the sample during deposition that reduces the quality of the dielectric. A 5.67×10^{-5} m^2 aluminum capacitor test structure with a 107 nm silicon nitride layer was also used for electrical characterization. The obtained dielectric constant of the silicon nitride layer (with refractive index 1.832) was found to be 5.4 and the breakdown field 4.1MV/cm [2].

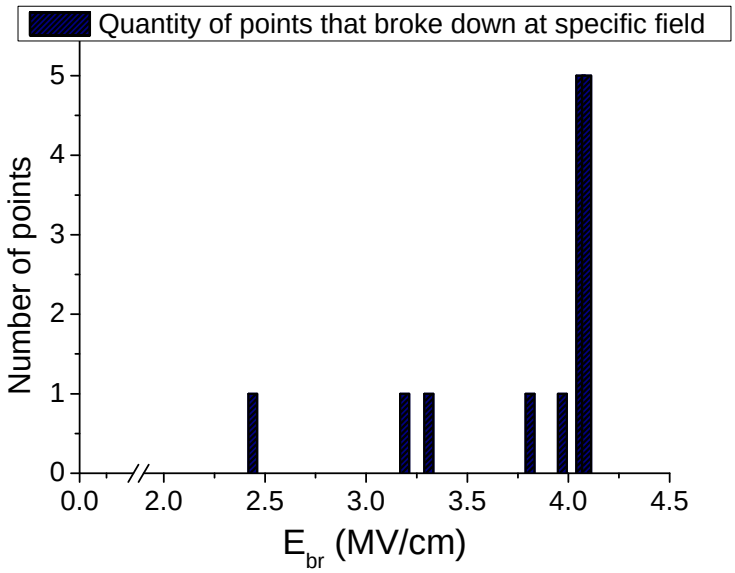

Figure II-29. Breakdown field distribution for a 320 nm SiO_x film deposited from 5 sccm SiH_4, 40 sccm O_2 at 1 kW microwave power, a 1.5 mTorr pressure and a substrate bias of – 40V.

Conclusion

In this Chapter, the influence of various process parameters on the deposited material and plasma properties was presented. Section II-2 discussed the influence the gas flow ratio has on the deposition of silicon oxide, oxynitride and nitride films. The second process parameter investigated in Section II-3 was the microwave power. It was found that additional atomic oxygen is generated in the SiH_4/O_2 gas mixture when the microwave power is increased, but is consumed during the deposition and thus leads to an increase in the deposition rate. Applying a higher microwave power was also found to improve the density of SiN_x films, leading to a higher refractive index and higher precursor utilization.
Section II-4 discussed the influence the process pressure and heating of the substrate holder have on the composition of the depositions and their corresponding plasma characteristics. The influence of applying an RF biasing to the substrate holder was explained in Section II-5 and the results compared to those shown in literature. To conclude the Chapter, three applications of the process parameter study were shown: *1)* The computer controlled deposition of a Bragg mirror using alternating layers of SiO_2 and SiN_x; *2)* the application of SiO_2, SiN_x and gradients of these materials as water barrier coatings for PET and *3)* the use of SiO_2 and SiN_x as dielectrics for interlayer isolation.

Chapter III will elaborate further on the influence the silane injection system has on the precursor consumption, deposition rate and quality of the films, with special emphasis placed on their silanol content.

References

[1] D. Daineka, P. Bulkin, G. Gerard, B. Drévillon, J. Vac. Sci. Technol. A, 22 (2004) 36.

[2] R. Botha, B. haj Ibrahim, P. Bulkin, B. Drévillon, Thin Solid Films, 515 (2007) 7594.

[3] D. Daineka, P. Bulkin, G. Girard, J.-E. Bourrée, B. Drévillon, Eur. Phys. J. Appl. Phys., 26 (2004) 3.

[4] P. Bulkin, N. Bertrand, B. Drévillon, Thin Solid Films, 296 (1997) 66.

[5] A. Goullet, C. Vallée, A. Granier, G. Turban, J. Vac. Sci. Technol. A, 18 (2000) 2452.

[6] S. Rojas, A. Modelli, W.S. Wu, A. Borghesi, B. Pivac, J. Vac. Sci. Technol. B, 8 (1990) 1177.

[7] T.V. Herak T.T. Chau, D.J. Thomson, S.R. Mejia, D.A. Buchanan, K.C. Kao, J. Appl. Phys., 65 (1989) 2457.

[8] W.A. Pliskin, J. Vac. Sci. Technol. A, 5 (1977) 1064.

[9] T. Roschuk, J. Wojcik, X. Tan, J.A. Davies, P. Mascher, J. Vac. Sci. Technol. A, 22 (2004) 883.

[10] F. Ay, A. Aydinli, Optical Materials, 26 (2004) 33.

[11] G. Lucovsky, D.V. Tsu, J. Vac. Sci. Technol. A, 5 (1987) 2231.

[12] A. del Prado, E. San Andrés, F.L. Martinez, I. Martil, G. Gonzalez-Diaz, W. Bohne, J. Röhring, B. Selle, M. Fernandez, Vacuum, 67 (2002) 507.

[13] N. Kitamura, K. Fukumi, and J. Nishii, N. Ohno, J. Appl. Phys., 101 (2007) 123533-1.

[14] M.J. Hernandez, J. Garrido, J. Martinez, J. Piqueras, Semicond. Sci. Technol., 12 (1997) 927.

[15] G. Lucovsky, P.D. Richard, D.V. Tsu, S.Y. Lin, R.J. Markunas, J. Vac. Sci. Technol. A, 4 (1986) 681.

[16] P. Bulkin, P. Swart, B. Lacquet, J. Non-Cryst. Solids, 226 (1998) 58.

[17] A. Banerjee, T. DebRoy, J. Vac. Sci. Technol. A, 10 (1992) 3395.

[18] K. Aumaille, A. Granier, M. Schmidt, B. Grolleau, C. Vallée, G. Turban, Plasma Sources Sci. Technol. A, 9 (2000) 331.

[19] M.A. Lieberman, A.J. Lichtenberg, *Principles of Plasma Discharges and Materials Processing, 2nd ed.*, John Wiley & Sons, Hoboken, New Jersey (2005).

[20] P. Bulkin, P. Swart, B. Lacquet, Thin Solid Films, 241 (1994) 247.

[21] A.J. Flewitt, A.P. Dyson, J. Robertson, W.I. Milne, Thin Solid Films, 383 (2001) 172.

[22] M. Orfert, K. Richter, Surf. Coat. Technol., 116-119 (1999) 622.

[23] A. Wiersch, C. Heedt, S. Schneiders, R. Tilders, F. Buchali, W. Kuebart, W. Prost, F.J. Tegude, J. Non-Cryst. Solids, 187 (1995) 334.

[24] P. Masini, M. Bernasconi, J. Phys.: Condens. Matter, 14 (2002) 4133.

[25] B. Haj Ibrahim, P. Bulkin, D. Daineka, B. Drévillon, Proc. SPIE, 5963 (2005) 500.

[26] B. Haj Ibrahim, R. Botha, J.-E. Bourée, P. Bulkin, B. Drevillon, Applied Optics, 46 (2007) 7776.

[27] P. V. Bulkin P.L. Swart, B.M. Lacquet, J. Non-cryst. solids, 187 (1995) 403.

[28] R. Botha, B. Haj Ibrahim, P. Bulkin, B. Drévillon, J. Vac. Sci. Technol. A, 26 (2008) 1115.

[29] K.L. Seaward, J.E. Turner, K. Nauka, A.M.E. Nel, J. Vac. Sci. Technol. B, 13 (1995) 118.

[30] C. Charles, J. Phys. D: Appl. Phys, 36 (2003) 1.

[31] E.S. Bulat, G. Ditmer, C. Herrick, S. Hankin, J. Vac. Sci. Technol. A, 10 (1992) 1402.

[32] R.G. Andosca, W.J. Varhue, E. Adams, J. Appl. Phys., 72 (1992) 1126.

[33] B. Aguis, M.C. Hugon, N. Jiang, F. Varniere, F. Plais, D. Pribat, M. Froment, M. Puech, Mat. Res. Soc. Symp. Proc., 284 (1993) 181.

[34] P. Bulkin, A. Hofrichter, T. Heitz, J. Huc, B. Drévillon, J. J. Benattar, J. Vac. Sci. Technol. A, 20 (2002) 338.

[35] B. Haj Ibrahim, R. Botha, P. Bulkin, B. Drévillon, Physica Status Solidi, 5 (2008) 1290.

[36] W.A. MacDonald, J. Mater. Chem., 14 (2004) 4.

[37] D.G. Howells, B.M. Henry, J. Madocks, H.E. Assender, Thin Solid Films, 516 (2008) 3081.

[38] D. Goghero, A. Goullet, J.P. Landesman, Solid-state Electron., 49 (2005) 369.

Chapter III

Investigating the gas injection in a High Density Plasma system

III-1 Introduction

In the previous Chapter, the deposition and characterization of silicon dioxide, nitride and oxynitride in the MDECR-PECVD system, using a gas ring for the silane injection, was described. This Chapter will focus on the high-rate deposition of silica films using directional jet injection of the silane precursor [1]. The aim is to study the importance the primary SiH_4 flux has on the SiO_2 deposition. The influence the silane delivery to the substrate has on the deposition rate and the hydroxyl incorporation into the film is also of interest. This study is done by replacing the gas ring for silane injection with a capillary jet.

The study starts by looking at the uniformity and intensity of the flux of oxygen radicals and ions onto the substrate surface as a function of the different process parameters. Section III-3 then presents the different silane injection systems used during the study, and the influence they have on the deposition rate. The well-mixed reactor hypothesis is then discussed. Section III-4 reports the influence of the directionality of the primary silane flux on the deposition of silicon dioxide, by combining phase modulated spectroscopic ellipsometry, AFM, FTIR and transmission measurements with QMS measurements. The deposited materials' properties, with special emphasis placed on the films hydroxyl content, are studied at different distances from the injection point, while also looking at how changes in the process parameters influence the depositions.

III-2 The ashing of photoresist using an O_2 plasma

In order to study the uniformity of the oxygen radical flux onto the substrate surface, the stripping of photoresist using an oxygen plasma was investigated. For this purpose, 1 μm of Shipley Microposit S1400 positive photoresist [2] was spin-coated onto a set of crystalline silicon wafers. The thickness of the photoresist was measured before etching, and the end point of the etching process detected using in-situ spectroscopic ellipsometry.

The ashing of photoresist in ECR systems using oxygen plasmas have been reported by other researchers [3-6]. The results concerning the oxygen plasma are consequently not novel, but the study is necessary to ensure that the active oxygen flux onto the substrate is uniform. This is important for the DSMC simulation, which will be described in Chapter IV. The ash rate results with different process parameters can be seen in Fig. III-1.

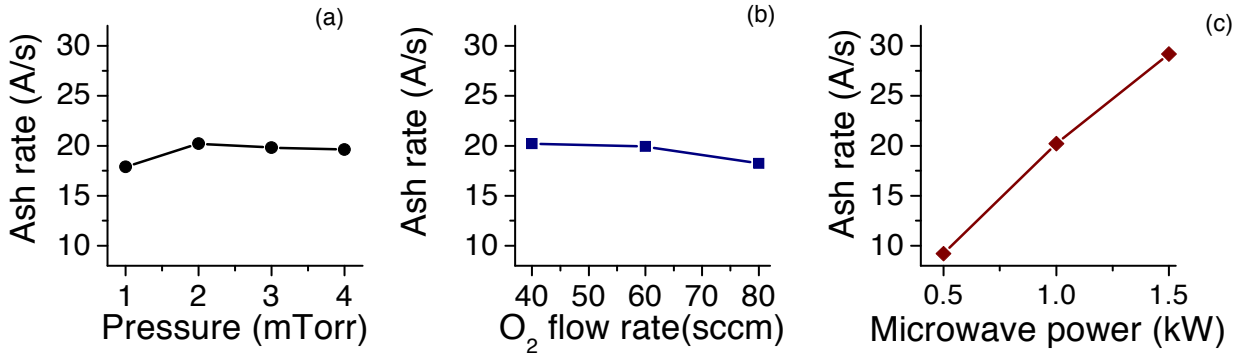

Figure III-1. Ashing of photoresist in oxygen plasma, with *(a)* increasing pressure, *(b)* oxygen flow and *(c)* different microwave powers.

The effect the process pressure and oxygen flow rate have on the ash rate are shown in Fig. III-1*(a)* and *(b)*. They are found to have only a slight influence on the stripping of the photoresist. The etch rate as a function of the microwave power can be seen in Fig. III-1*(c)*. It increases approximately 3 times when the power is increased from 500 to 1500 W. The flux of oxygen radicals onto the substrate surface is thus the determining factor during the photoresist etching process. The uniformity of the oxygen flux onto the substrate holder was estimated by mapping the photoresist thickness across a 150 mm silicon wafer before etching and re-measuring the photoresist thickness after etching in an oxygen plasma, but stopping before the resist is stripped entirely. A flow rate 40 sccm O_2 was used, together with 1 kW microwave power and a pressure of 3 mTorr. The etch rate across the wafer can be seen in Figure III-2 and is found to have a uniformity of ±4.2%. It is interesting to note the similarity between the etch map presented here and the SiO_2 deposition map across a 200 mm wafer that was discussed in Chapter I.

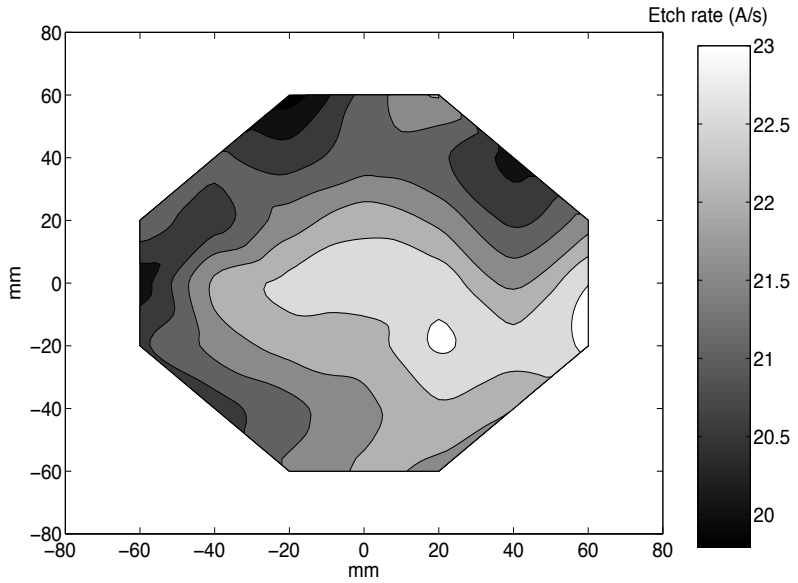

Figure III-2. Uniformity of photoresist ashing over a 150 mm diameter wafer.

III-3 Gas ring versus capillary jet injection of silane

The design of the gas injection manifold in vacuum systems has been the subject of studies for several years [7-9]. Most systems make use of a tubular gas ring with holes spaced at regular intervals around its edge. These systems are usually designed either by trial and error, previous experience or simple rules of thumb. Using such a gas ring it is possible to attain a relatively uniform gas distribution in the vacuum chamber. It is thus understandable that for a gas, such as silane, that has dissociation products with high sticking coefficients[3], the correct positioning and design of the injection system is very important for optimizing the process.

The precursor injection system in a commercially available HDP CVD machine from Novellus is shown in Figure III-3. It uses volume injection in the direction pointing away from the substrate. It assures uniform deposition, but needs to rely on re-sputtering to achieve high deposition rates. In such a system, re-sputtering accounts for a large part of the deposition rate.

Though other studies have made use of a jet injection system for the deposition of silicon nitride [10] and for the injection of helium diluted silane[11], a detailed experimental study of the different silane distribution systems is still required, in order to understand how a particular gas is dispersed in the vacuum system and what influence its distribution has on the deposition rate. A simulation of the gas flow in the vacuum system also allows us to gain further insight into the ideal design of the injection system and will be presented in Chapter IV.

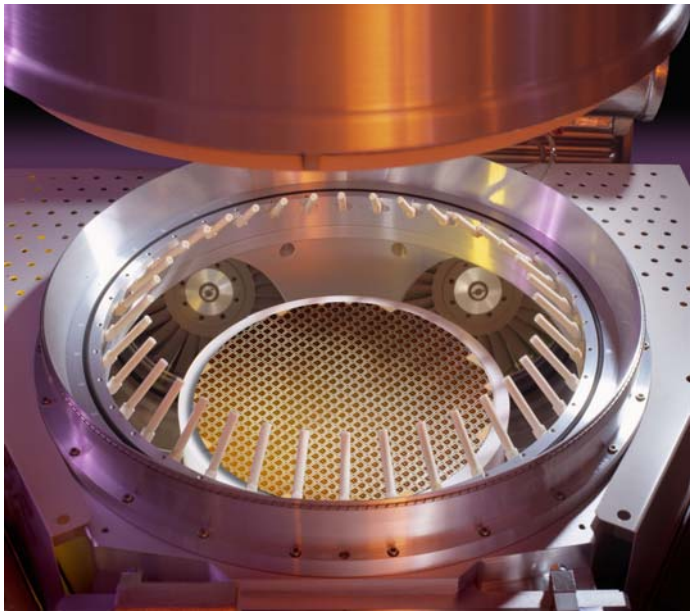

Figure III-3. The Novellus HDP CVD system with a volume injection system.

The three different SiH_4 injection systems used during this study can be seen in Figure III-4. Regardless of the SiH_4 injection system used, the O_2 precursor gas was always introduced into the vacuum chamber in the antenna region, as was indicated on Figure I-6 in Chapter I.

The gas ring injection system shown in Figure III-4 *(i)* was used to attain uniform depositions across 200 mm wafers, as was discussed in Chapter I. The results contained in Chapter II all made use of this injection system. It was then first replaced by a 20° angled capillary jet and then by a vertical capillary jet, both with an internal diameter of 1 mm, as shown in Figure III-4 *(ii)* and *(iii)*.

Figure III-5 shows the thickness mapping results of silicon dioxide films deposited using the angled and the vertical positioning of the capillary jet shown below. The

aim of this is to study an intentionally non-uniform deposition at different distances from the injection point, as indicated on Figure III-4. This makes it possible to gain insight into the deposition mechanism [1].

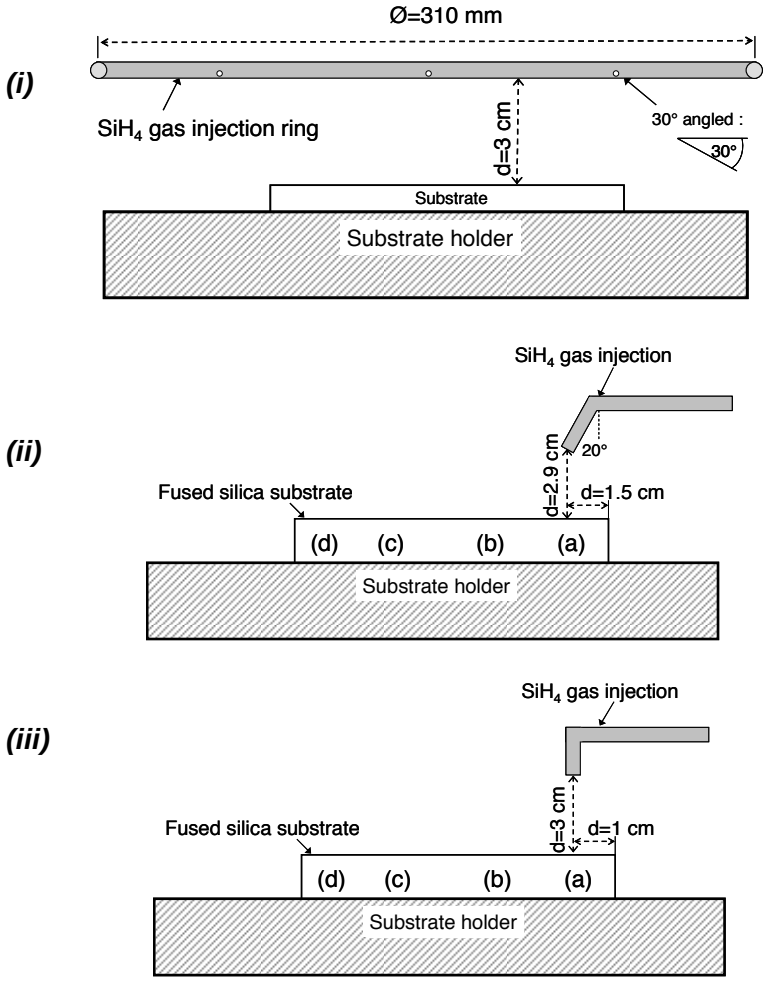

Figure III-4. *(i)* : SiH_4 gas ring around the periphery of substrate holder. *(ii)* Angled jet injection system with transmission measurements done at four points on the substrate (a) 1.5cm, (b) 3.5cm, (c) 6cm and (d) 7.5cm. *(iii)* Vertical SiH_4 injection system, measurements were done at (a) 1.5cm, (b) 3cm, (c) 4.5cm and (d) 6cm.

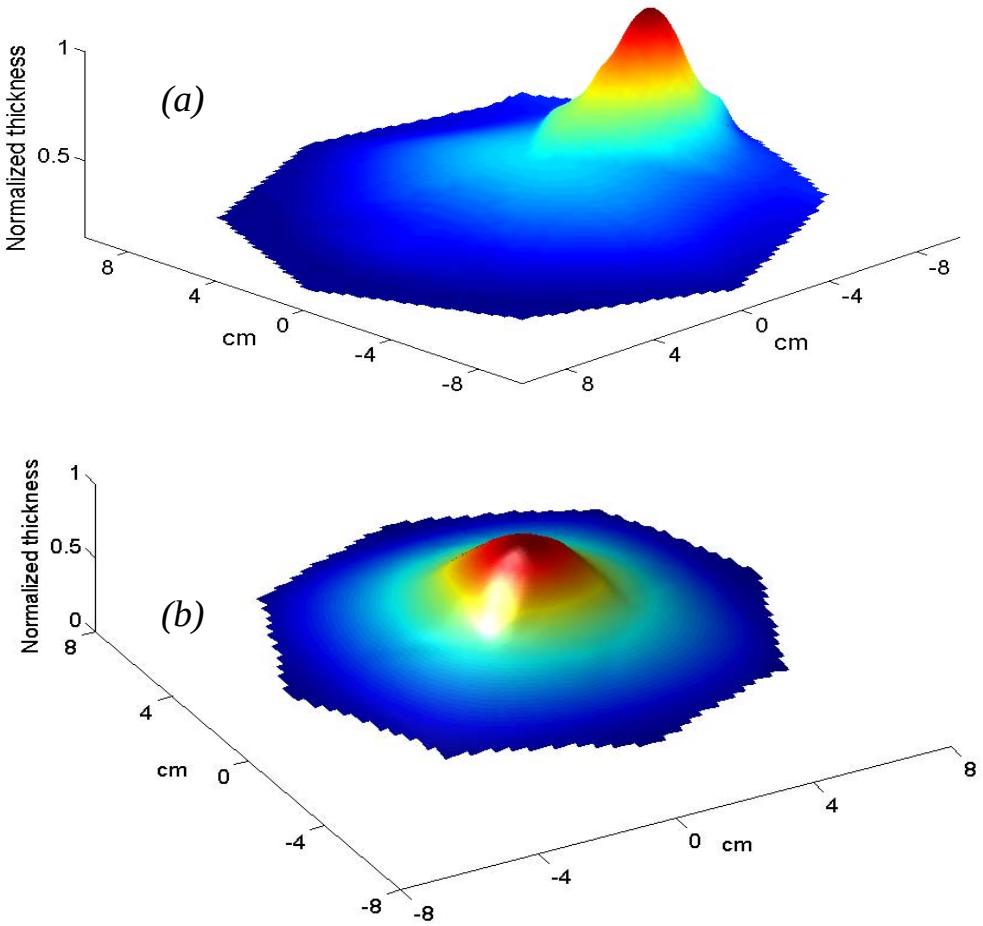

Figure III-5. Thickness scans of two SiO_2 depositions with *(a)* the angled capillary and *(b)* the vertical injection point. The capillary was positioned at the edge of the substrate in *(a)* and over the centre of the substrate in *(b)*.

The relation between the deposition rate and the water incorporation into the film at the different positions is studied as a function of the various process parameters, and will be shown in Section III-4. Previous studies done on the Si-OH concentration in deposited SiO_2 films made use of silane and oxygen precursors that were highly diluted in argon, while entirely disregarding the partial pressure of water as a possible source for OH inclusion into the film [12,13]. This can not be correct, as the water flux is at least comparable to the silane flux. In Figure III-6, QMS measurements taken in the vicinity of the microwave antennas,

with and without a deposition plasma, show the drop in SiH_4 concentration and the corresponding rise in H_2O production in the gas phase in the presence of a plasma. The production of water, which is the main byproduct produced during the deposition process, will be practically constant at a given set of oxygen and silane flows, irrespective of the design of the injection system. The flux of H_2O onto the substrate surface will thus be uniform, while the flux of silane from the capillary jet will not be uniform across the substrate area. The deposition rate will consequently vary over the entire substrate. As a result of this the quantity of water incorporated into the film will be constant across the substrate, but as the deposition rate depends on the primary silane flux, the regions of high deposition rate will contain a lower quantity of hydroxyl bonded species per volume than the lower deposition rate regions. In Section III-4 the deposited films Si-OH absorption is studied at different distances from the capillary tube, while varying the deposition conditions. This helps to shed light on the contribution of the H_2O partial pressure on the hydroxyl concentration in the SiO_2 films.

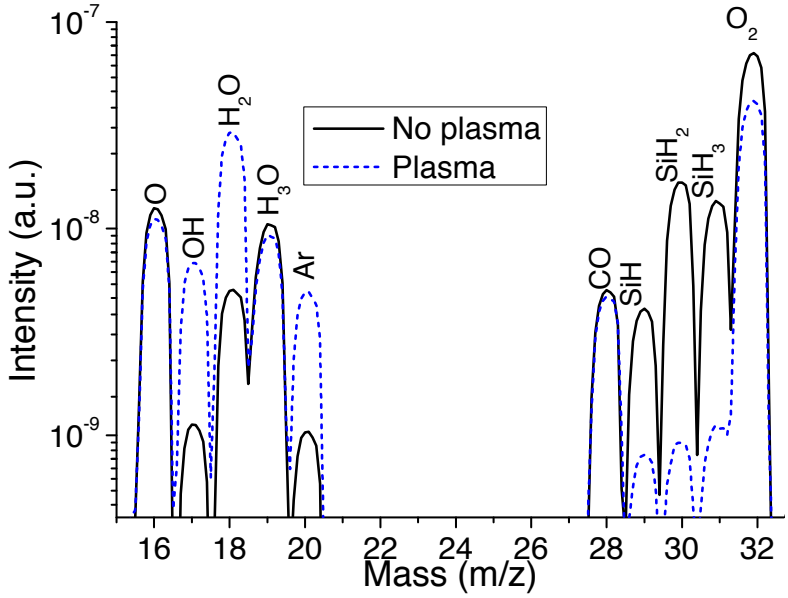

Figure III-6. Mass spectra of a 40 sccm O_2 and 5 sccm SiH_4 gas mixture, with and without a plasma.

III-3.1 Deposition rate, precursor consumption and the well-mixed reactor

The deposition rate of silicon dioxide films deposited using the different silane injection systems shown in Figure III-4 was found to vary tremendously. While the highest deposition rate using the gas ring injection system was found to be 21 Å/s at a SiH_4 flow of 35 sccm and 120 sccm O_2, the angled jet injection was able to achieve higher deposition rates with lower SiH_4 and O_2 flow rates, as shown in Figures III-7 and III-8. The increase in the deposition rate with a rise in the silane gas flow is observed as expected. The refractive indices however remained constant and equal to that of stoichiometric silica. As would be anticipated, the uniformity of the jet injected films are by far not as good as the films deposited with the gas ring injection system, but this is intentional.

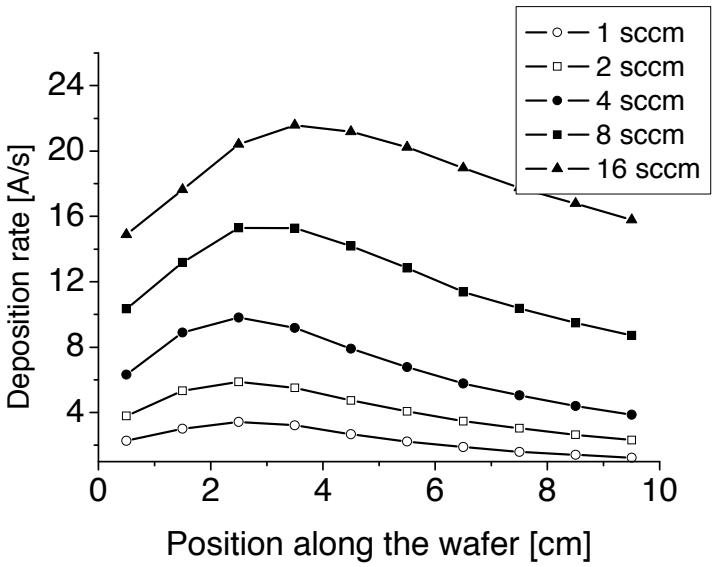

Figure III-7. Deposition rate profiles for different silane flows measured along the infrasil substrate as shown in Figure III-4*(ii)* for the angled capillary jet.

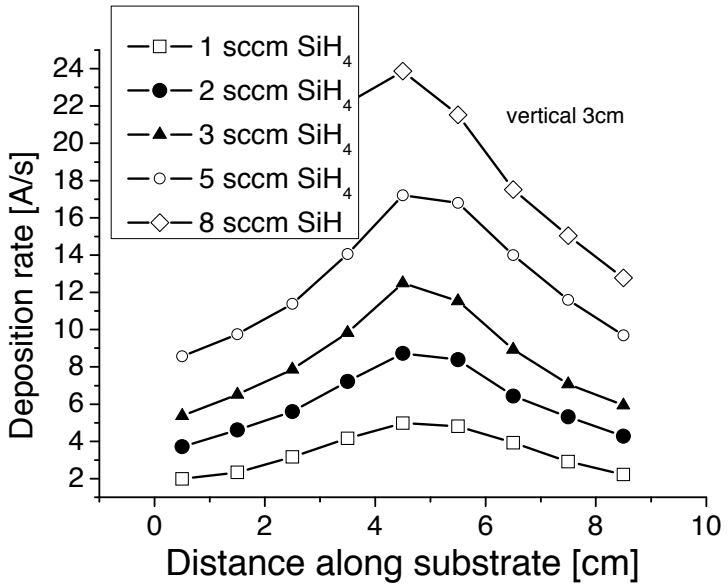

Figure III-8. Deposition rate profiles for different silane flows measured along the infrasil substrate as shown in Figure III-4*(iii)* for the vertical capillary jet.

The difference between the deposition rates when using the gas ring and the capillary jet injection point can be understood by considering the data contained in Table III-1. Here, the deposition of silicon dioxide onto four silicon wafers placed at different positions in the HDP system, when using the gas ring for silane injection, is shown. It can be seen that deposition takes place on all surfaces in the system. As was mentioned before, the dissociation products of the silane precursor have high sticking coefficients, leading to deposition on all surfaces with which they come into contact [14]. However, it is not only the dissociation products that need to be taken into consideration, but first and foremost the neutral silane molecules, as they may get oxidized on the surface by incoming oxygen radicals and ions. It is clear from Table III-1 that the initial

flux of silane molecules are participating in the deposition and could even be considered as having the largest influence on the deposition.

Sample position	Deposition rate
Substrate holder	5.3 Å/s
On top of the gas ring	1.1 Å /s
Bottom of reactor chamber	0.7 Å /s
Reactor wall - *different conditions as sample is placed vertically*	0.4 Å /s

Table III-1. Deposition rate at different positions in the system when using the gas distribution ring shown in Figure III-4*(i)*. A 10 sccm SiH_4 and 40 sccm O_2 gas mixture, 1kW MW power and 0.5 mTorr pressure was used.

The normalized QMS measurements in Figure III-9 show the ratio of the SiH_2^+ ion intensity with a deposition plasma in the reactor chamber, to its intensity without a plasma (in other words, when no silane consumption is taking place). It can be seen that over the entire range of microwave powers investigated, the consumption of the silane precursor improves slightly when the gas ring is replaced by the vertical capillary jet injection system. The difference between the two injection systems lies in the fact that a larger quantity of the precursor is consumed at the substrate level when using the capillary, thus leading to a higher deposition rate. When using the gas ring, the loss of precursors to the walls has to be compensated by increasing the silane flow, if the deposition rate on the substrate surface is to be increased. Though this fact might seem intuitive to the reader, it is of fundamental importance to take it into account when designing the

gas injection system, as it must provide a directed flux of precursors onto the depositing surface.

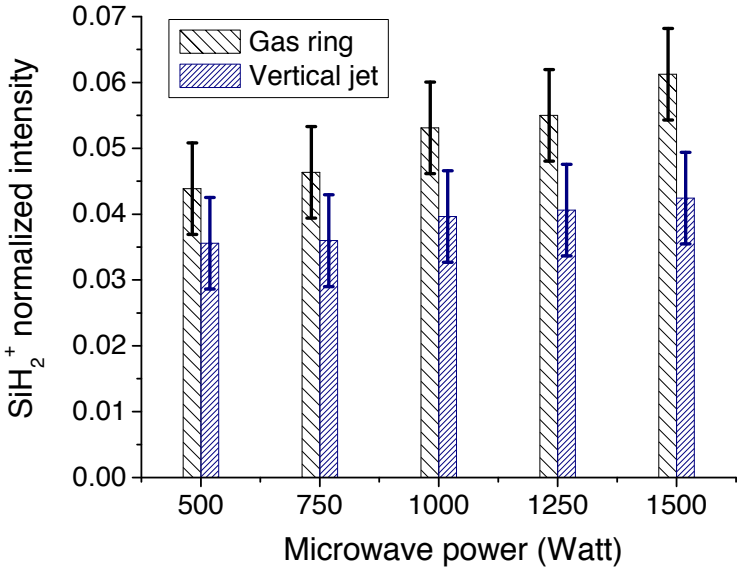

Figure III-9. The SiH_4 consumption at different MW powers when using either a gas ring, or a vertical capillary tube for the precursor injection. Error bars show the standard deviation observed.

The currently accepted paradigm is that very low pressure PECVD systems that are based on HDP principles, are well-mixed[15,16], meaning that the deposition onto all the surface are equal due to the large mean free path of the species. This assumption, that states that there is an equal quantity of fluxes onto all surfaces in HDP systems, holds true for noble gases which do not react in the volume or on surfaces and to a certain extent for nitrogen and oxygen, which can be dissociated in the volume but recombines on surfaces and returns to the volume. It is however not the case for silane, especially in the presence of oxygen, as can be seen from the results shown in Table III-1.

From the above discussion it is seen that the primary silane flux onto the substrate surface, which depends on the positioning of the jet injection point, has an important influence on the film's deposition rate. HDP systems can thus not be considered as well-mixed for gases such as SiH_4 that have dissociation products with high sticking coefficients and ground-state molecules that have the possibility to be consumed on the surface through reactions with oxygen radicals and ions.

To conclude the comparison of the injection systems, Figure III-10 shows AFM images of SiO_2 depositions done with the gas ring and the vertical capillary jet shown in Figure III-4 *(i)* and *(iii)*. The surface rms roughness for the deposition done with the gas ring is found to be 0.224 nm on a 1330 nm thick layer, which increases up to 1.3 nm for the capillary jet deposition, which had a thickness of 8140 nm.

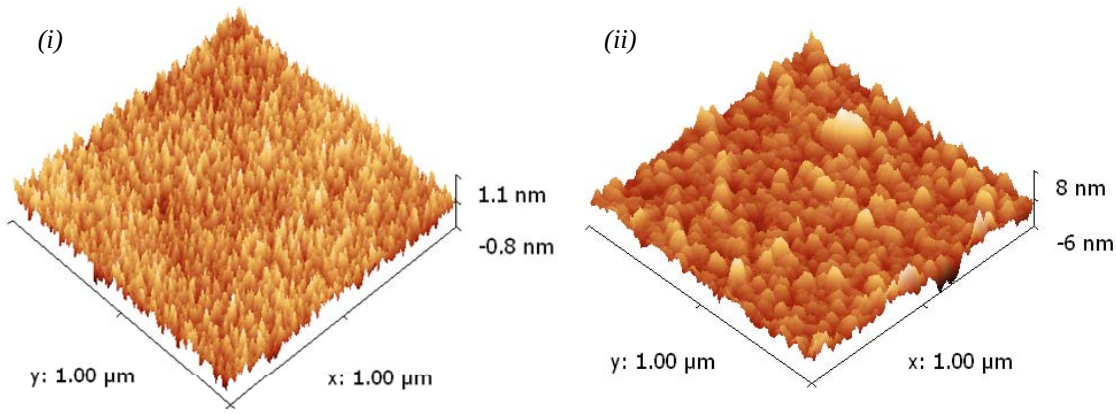

Figure III-10. AFM images of SiO_2 depositions, done using a *(i)* gas ring and a *(ii)* capillary jet for injecting the SiH_4 precursor gas.

III-4 Silanol content in films deposited with different silane injection systems

Contamination of deposited silicon dioxide layers by hydroxyl is known to cause strong absorption, due to its fundamental absorption band at 2.72 μm (about 3650cm^{-1}) and overtone at ~1.38 μm which is in the optical communication window[17]. Different low temperature processes that provide Si-OH concentrations below the IR detection limit, either due to ion bombardment or, in some cases, optimized desorption kinetics as a result of low deposition rates or the use of hydrogen meditated abstraction, have been reported [18-22]. In this section it is shown that the distance between the deposition surface and the silane injection point is an important factor determining the quantity of silanol incorporated into the deposited film.

Transmission and spectroscopic ellipsometry measurements were performed on various silicon dioxide films deposited onto Infrasil fused quartz substrates with the different injection systems, in order to determine the type and quantity of silanol bonds. Measurements of all the samples were taken directly after deposition. Selected samples were re-measured after approximately a month, which revealed no noticeable changes due to atmospheric exposure.

The hydroxyl that is chemically bonded to the silica network is observed as a fundamental absorption band between 3000 cm^{-1} and 3800 cm^{-1}. It can be deconvoluted into three Gaussian bands[23], as shown in Figure III-11. The

Gaussian band around 3650 cm^{-1} corresponds to the isolated silanol content, while the lower Gaussian bands in the 3450 cm^{-1} vicinity represent the associated Si-OH vibration mode which is also sometimes called the water symmetric feature, near-neighbour or partially shielded Si-OH.

Transmission measurements showed the majority of the films to be stoichiometric silica, while a few of them were slightly silicon rich. Modeling of the ellipsometric measurements using the Bruggeman effective index approximation and a combination of SiO and SiO_2 materials, revealed that these films consist of at least 97 percent SiO_2, though the accuracy of these results are close to the accuracy of ellipsometric measurements.

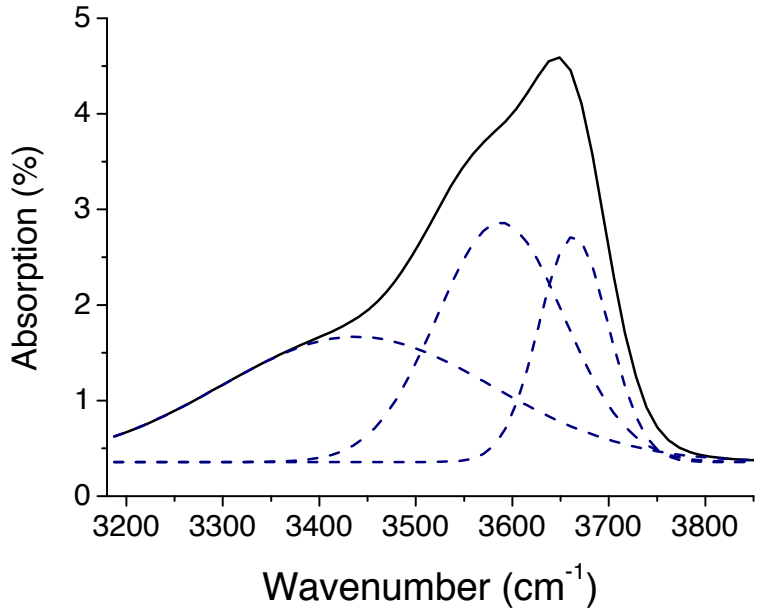

Figure III-11. Deconvolution of the Si-OH stretching absorption peak into three Gaussian bands.

III-4.1 The influence of varying the process parameters

Figure III-12 shows the linear decrease of the Si-OH peak intensity with increased growth rate for four points on four different depositions. All samples were thickness normalized. These depositions were done using the angled jet injection system depicted in Figure III-4*(ii)*, while measurement were taken on the points indicated by *(a)* to *(d)*. A SiH_4 flow of 8 sccm, 40 sccm O_2, 1 kW microwave power, 3 mTorr pressure and no substrate bias were used, unless otherwise indicated on the figure. Numerous tendencies can be seen on this figure. Silanol inclusion into the deposited film is found to increase when the oxygen flow rises, which is similar to results reported by other researchers [24,25].

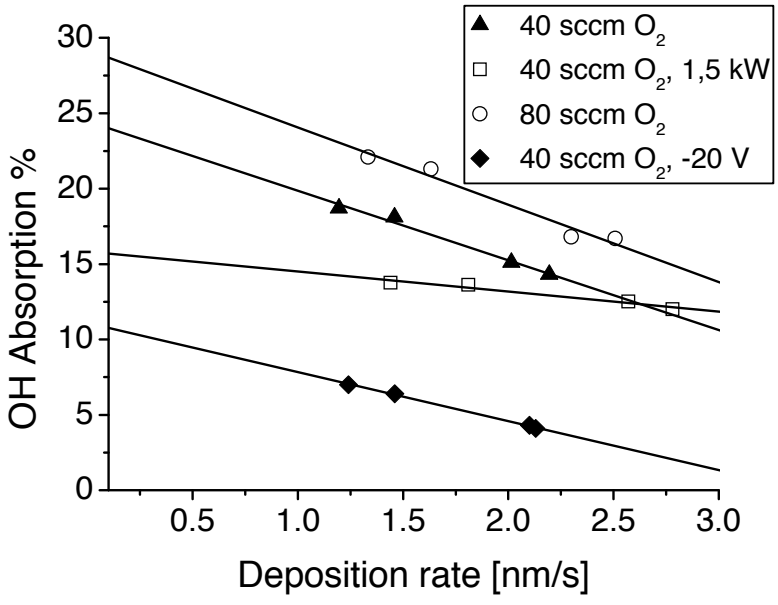

Figure III-12. Deposition rate measurements at four points along the depositions shown in Figure III-4, with their corresponding Si-OH absorption peak intensities.

Rising microwave power leads to a reduced Si-OH content, though the effect is not prominent as the deposition rate increases. Applying a low RF power resulting in a DC self-bias of -10V to the substrate holder is found to be an effective way of reducing the Si-OH content [22]. However applying an RF bias is not always an option.

If the deposition conditions are kept within the range discussed in Chapter II, it is found that the hydroxyl content in the film always increases linearly with decreasing deposition rate. The explanation for this lies in the quantity of water produced in the system during the deposition. When the plasma is ignited, the partial pressure of water will stabilize after a short transitional period [26] and the water flux onto all the surfaces in the vacuum chamber will remain constant and uniform. The deposition rate is determined by the position of the substrate relative to the silane injection point, as was discussed in Section II-3.1. This means that though the flux of water incorporated into the growing film will be the same across the substrate, the high deposition rate under the silane injection point will lead to a low concentration of silanol, while for the low deposition rate observed further away from the silane injection point the concentration of silanol in the deposited film will be relatively high. The ideal design of the silane gas injection system consequently needs to maximize the flux of primary SiH_4 onto the substrate area with a minimum flux onto the surfaces outside of the substrate, while providing a sufficiently large flux of oxidizing species onto the surface. This will ensure that the total silane flow rate, and thus the generation of water, is kept as low as possible.

In addition to the four depositions that were shown in Figure III-12 a variety of SiO_2 films were deposited using the different capillary jet injection systems, while changing several process parameters such as the microwave power, silane gas flow, pressure and RF substrate bias. The influence these parameters have on the silanol content, the deposition rate as well as the oxygen and silane consumption for the various silane injection systems, are discussed in the subsequent sections.

III-4.1.1 Silane and oxygen gas flows

A series of films were deposited using different silane gas flows. Initially this was done using the angled and later the vertical jet injection systems, shown in Figure III-4*(ii)* and *(iii)*. Depositions were characterized in terms of refractive index, deposition rate and Si-OH content, as can be seen in Figure III-13 for the depositions done with the angled jet, and in Figure III-14 for the vertical jet samples. A microwave power of 1000 W was used, while keeping the oxygen flow constant at 40 sccm. For the angled jet depositions, a 3 mTorr pressure was used, while for the vertical jet it was set to 2 mTorr. No RF bias or heating were applied to the substrate holder during these depositions. The refractive index[*] of the deposited material was found to remain between 1.45 and 1.46 for all depositions. For both injection systems, the deposition rate as well as the Si-OH content increases with increased silane flow (as the total water production goes up).

[*] Refractive index will be quoted at 2eV for the remainder of this Chapter.

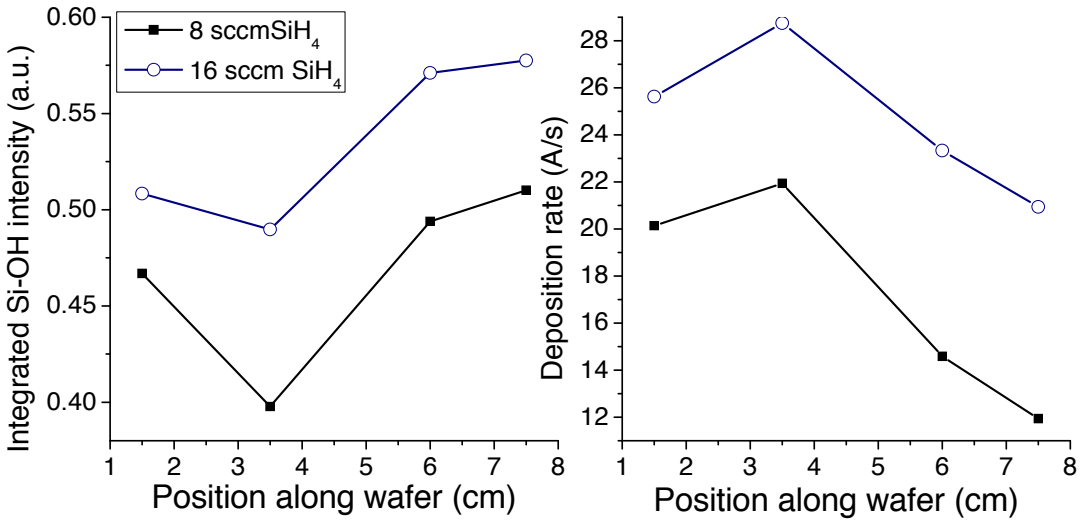

Figure III-13. Deposition rate and normalized integrated Si-OH intensity for SiO_2 depositions done using 8 and 16 sccm SiH_4, respectively, with the angled jet injection system.

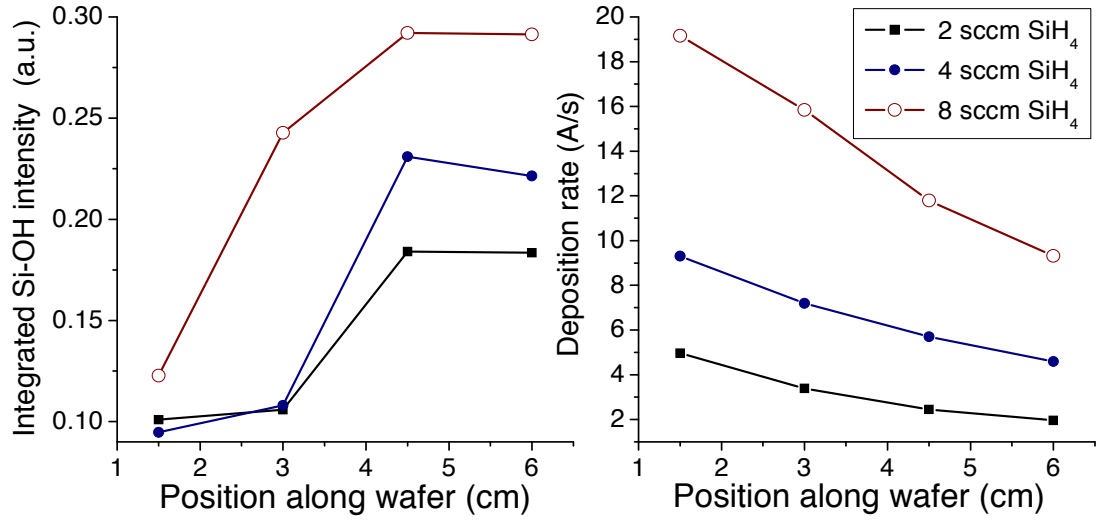

Figure III-14. Deposition rate and normalized integrated Si-OH intensity for SiO_2 depositions done with different SiH_4 flows and using the vertical injection system.

The QMS measurements in Figure III-15 show the ratio of the O_2^+ ion intensity when a deposition plasma is ignited in the reactor chamber, to its intensity without a plasma. In other words, the higher the O_2^+ normalized intensity†, the less oxygen is consumed during the deposition, and vice versa. The process parameters and oxygen flow were set to those mentioned above for the capillary jet. There is a marked improvement in the oxygen consumption with increased silane flow. The influence an increased oxygen flow has on the deposition rate and silanol content of films can be seen in figure III-16 and III-17. The silane flow was kept constant at 8 sccm, with the other parameters kept as defined for the silane flow series.

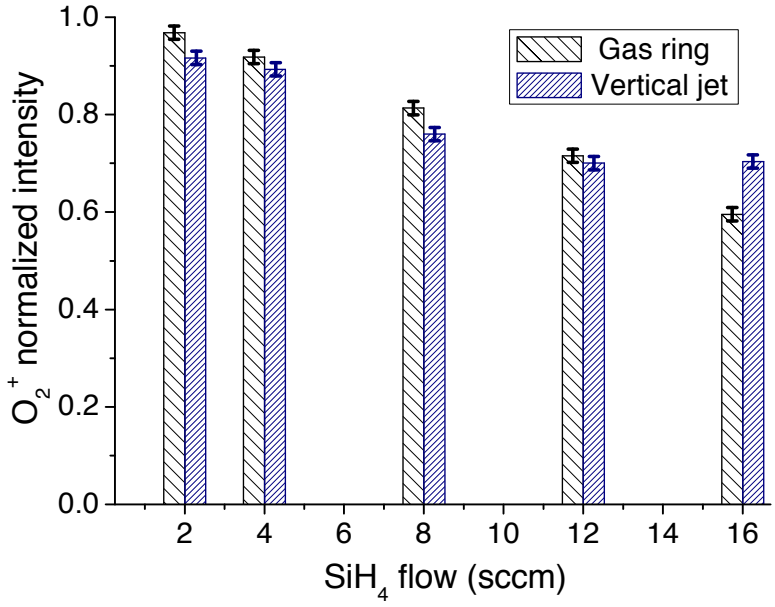

Figure III-15. The consumption of O_2 when using either a gas ring, or a vertical capillary tube for the precursor injection.

† As was mentioned before, the term normalized intensity refers to the ratio of the O_2^+ or SiH_2^+ ion intensity when a deposition plasma exists in the reactor chamber, to its intensity without a plasma (in other words, when no oxygen and silane consumption is taking place).

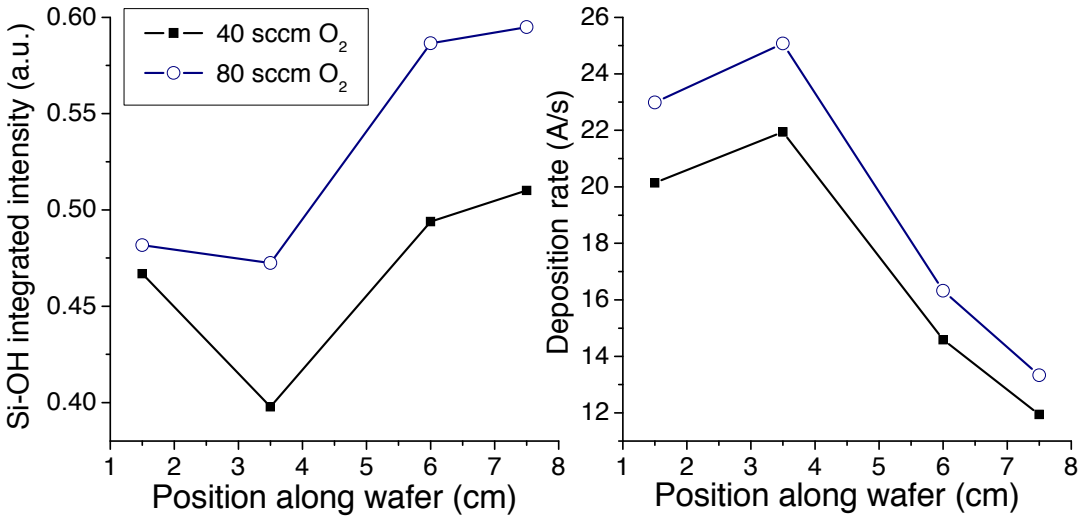

Figure III-16. Deposition rate and normalized absorption peak intensity for SiO_2 depositions done using 40 and 80 sccm O_2, respectively, with the angled jet injection system. 3 mTorr pressure and 1kW microwave power with 8 sccm SiH_4 was used.

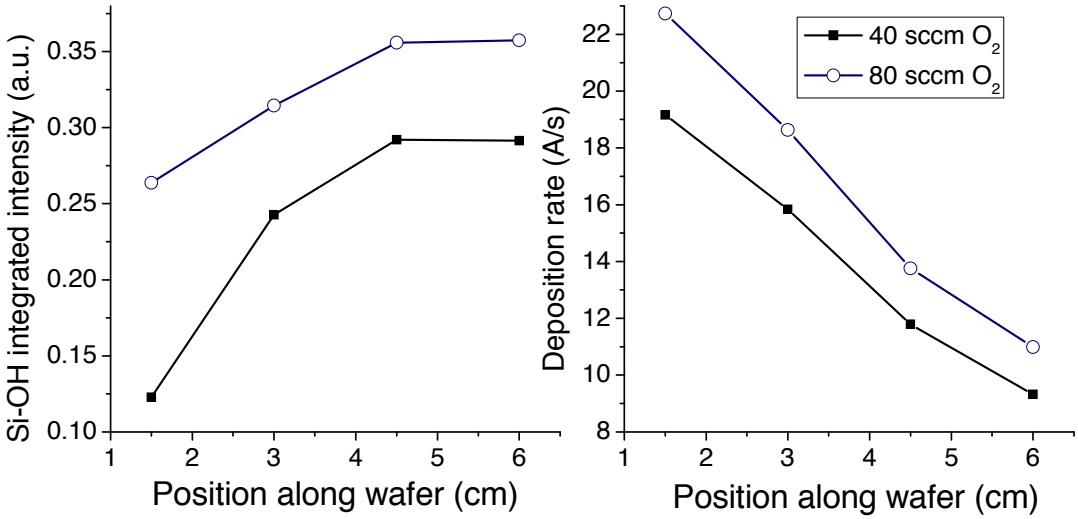

Figure III-17. Deposition rate and normalized integrated Si-OH intensity for SiO_2 depositions done with different O_2 flows and using the vertical injection system at 3 cm from the substrate plane. 2 mTorr pressure and 1kW microwave power with 8 sccm SiH_4 was used.

QMS measurements of the silane and oxygen consumption when increasing the oxygen flow rate, is depicted in Figure III-18. The oxygen consumed during the deposition can be seen to decrease with rising oxygen flow rate. While approximately 30 percent of the O_2 is consumed at a 40 sccm gas flow, it reduces to 15 percent at an 80 sccm flow. In both cases 12 sccm of O_2 is thus consumed. It can be concluded that there is not enough available silane molecules to react with the oxygen radicals. This is confirmed by the silane measurements that show the precursor to be almost entirely consumed at all oxygen flow rates, and which remains at a relatively constant value. During the deposition process the oxygen atoms, which are long-lived species, are able to consume the silane almost completely [27].

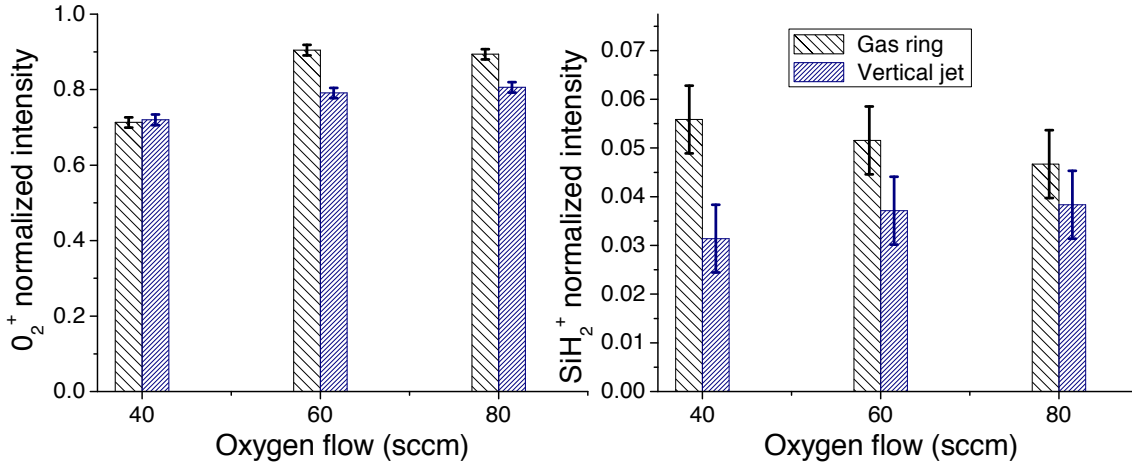

Figure III-18. The consumptions of O_2 and SiH_4 when using either a gas ring, or a vertical capillary tube for the precursor injection at different oxygen flow rates.

III-4.1.2 Microwave power

The deposition rate and silanol content of films deposited at different microwave power using the angled (Figure III-19) and the vertical capillary jet (Figure III-20) are shown. In both cases increased microwave power leads to a higher deposition rate and a corresponding decrease in silanol content.

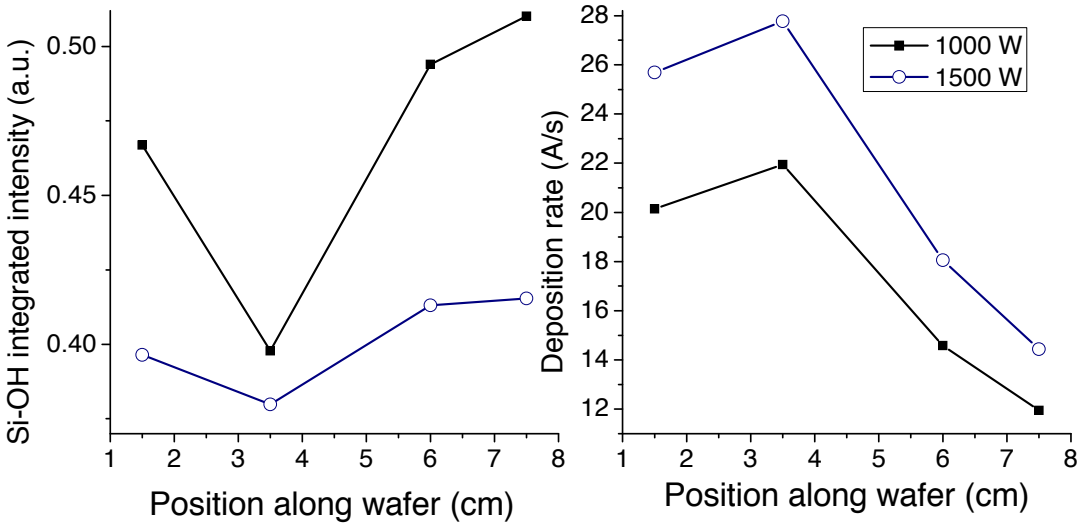

Figure III-19. Depositions done at two different microwave powers, using the angled injection system shown in Figure III-4*(ii)*.

As was discussed in Chapter II, optical emission measurements show an increases in the atomic oxygen fraction with microwave power that in turn leads to higher deposition rates. This fact explains the change in the gradient of the deposition rate observed at different microwave powers, as can be seen on Figure III-20. The flux of oxygen radicals onto the substrate surface is increased

at high microwave power. As there will be an abundance of oxygen atoms available at the growth surface, a part of the SiH_4 molecules arriving to the surface will immediately be oxidized on the surface and the Si atom be incorporated into the growing film. The higher microwave power will lead to a higher surface temperature, which in turn will lower the residence time of the H_2O on the surface and thus its incorporation into the film and lowering the hydroxyl content. At a low microwave power there will be a smaller flux of oxygen atoms onto the substrate surface and the SiH_4 molecule will have a higher chance to be desorbed from the substrate surface before being oxidized and consequently the Si atom incorporation is less probable and thus the deposition rate is lower. As the refractive index rises from 1.45 at 500 W up to 1.46 at 1500 W, it can be concluded that the decreased silanol content leads to a slight increase of the deposited film's density.

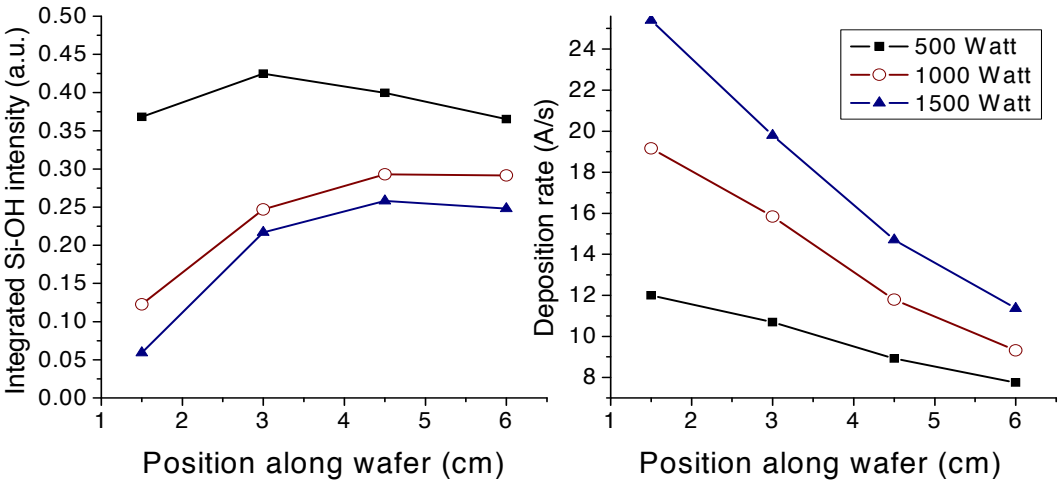

Figure III-20. Depositions done at 500, 1000 and 1500 Watt, using the vertical capillary jet shown in Figure III-4*(iii)*.

The O_2^+ and SiH_2^+ intensity ratios when there is a deposition plasma in the reactor chamber, to their intensities without a plasma, at different microwave powers, are shown in Figure III-21 for measurements taken at the back of the turbo-molecular pump, as described in Chapter I. From these figures it can be seen that both the oxygen and silane consumption remains constant with changes in the microwave power, as the changes are small and it is reasonable to assume they are due to fluctuations and drift in the equipment.

Increasing the microwave power thus does not change the utilisation of the precursor in the vacuum chamber, but does improve its consumption on the substrate surface, as was shown by the increase in the gradient of the deposition rate profiles in Figures III-19 and 20.

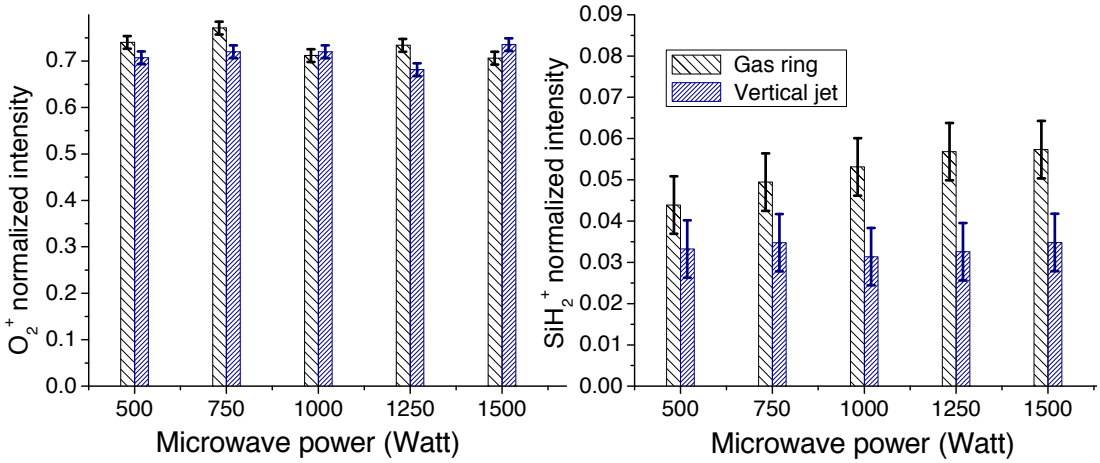

Figure III-21. The consumptions of O_2 and SiH_4 when using either a gas ring or a vertical capillary tube for the precursor injection and varying the microwave power.

III-4.1.3 Pressure

Depositions at different pressures were done using the angled and vertical jet injection systems. The resulting deposition rates and normalized Si-OH absorption, with the corresponding pressure used, are depicted in Figures III-22 and 23. Gas flows of 8 sccm SiH_4, 40 sccm O_2 and a microwave power of 1 kW were used. A pressure increase is found to result in a higher deposition rate and Si-OH content for both injection systems. The refractive index remains in the range of 1.45 to 1.46.

Others have attributed the increased silanol content to the hydroxyl groups in the TEOS precursor being incorporated to a greater extent at higher pressures[23]. Since this study makes use of silane as precursor gas which does not contain hydroxyl groups, the more likely reason is the increased residence time of the precursors in the reactor chamber when the pressure is increased. The concentration of water in the vacuum chamber is consequently increased, which leads to a higher level of water being incorporated.

The oxygen and silane consumptions with changing pressure can be seen in Figure III-24. As the oxygen consumption slightly decreases while the silane consumption remains constant, one would expect the deposited films to have a higher OH content to compensate for the lower oxygen usage. These results thus corroborate the higher Si-OH content found by the transmission measurements.

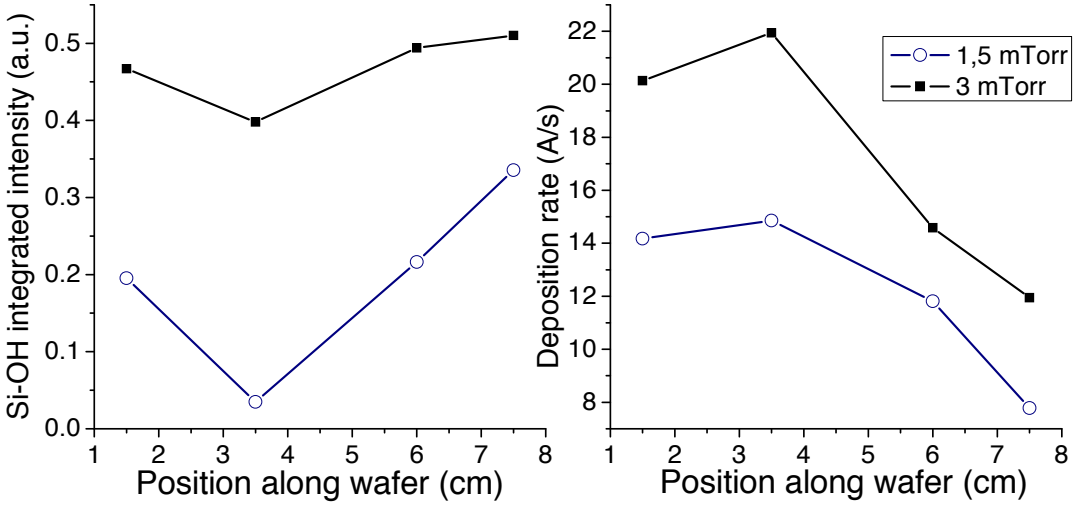

Figure III-22. Depositions done at 1.5 and 3 mTorr pressure, using the angled jet shown in Figure III-4*(ii)*.

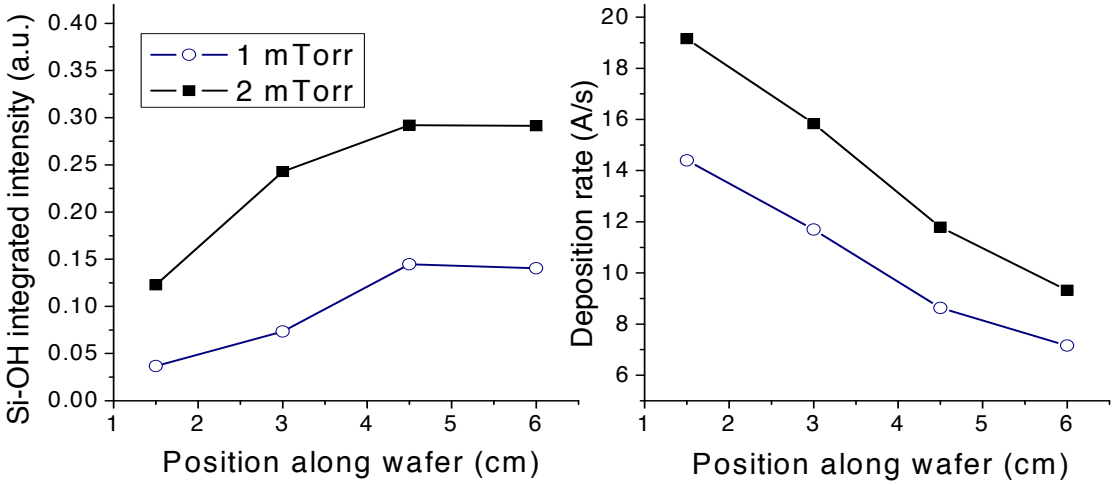

Figure III-23. Depositions done at 1 and 2 mTorr pressure, using the vertical capillary jet shown in Figure III-4*(iii)*.

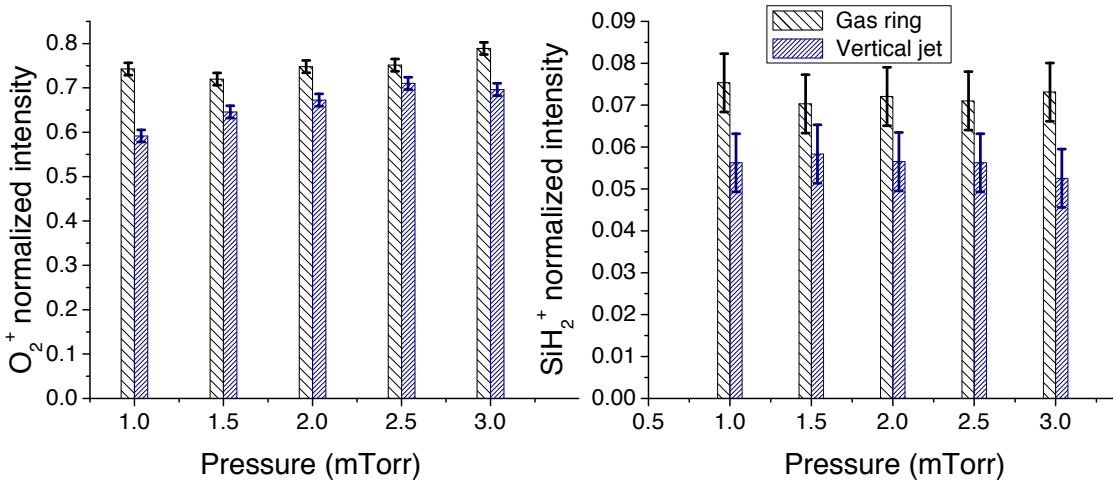

Figure III-24. The consumptions of O_2 and SiH_4 when using either a gas ring or a vertical capillary tube and varying the pressure.

III-4.1.4 Applying an RF bias to the substrate holder

The influence of applying an RF bias to the substrate holder, on the deposition rate and silanol content of silica films, was investigated by depositing three films at varying bias voltages with the angled jet, as presented in Figure III-25, and six films at different bias voltages with the vertical jet (see Figure III-26). The microwave power was set to 1 kW and the gas flows to 8 sccm and 40 sccm for the silane and oxygen gases, respectively. For the angled jet the pressure was set to 3 mTorr and for the vertical jet it was set to 2 mTorr. It can be seen that an RF bias applied to the substrate holder effectively removes the associated Si-OH vibration mode absorption peak located in the vicinity of 3400 cm^{-1}. A low RF bias is very effective at removing the hydroxyl contaminants, while a higher bias again increases the isolated silanol content. The refractive index remained between 1.45 and 1.46 for all depositions done.

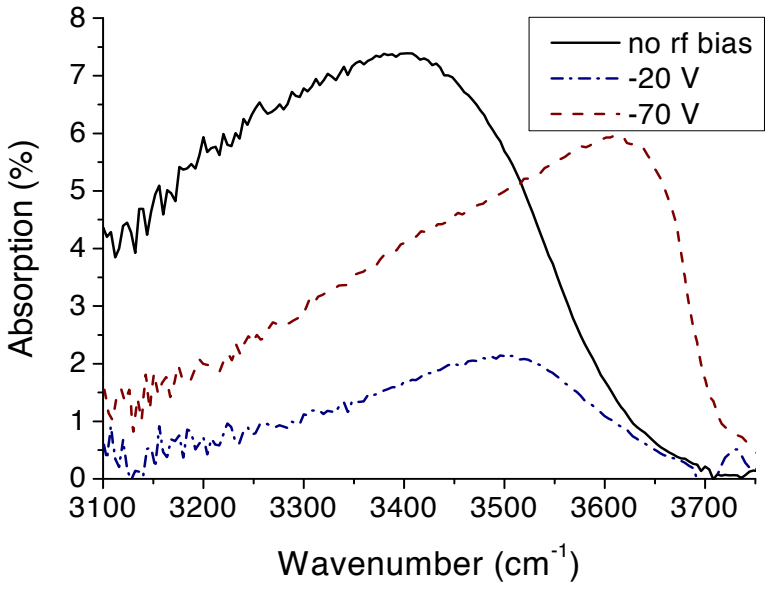

Figure III-25. Thickness normalized Si-OH absorption of SiO_2 films deposited using the angled jet system, at different RF substrate bias values.

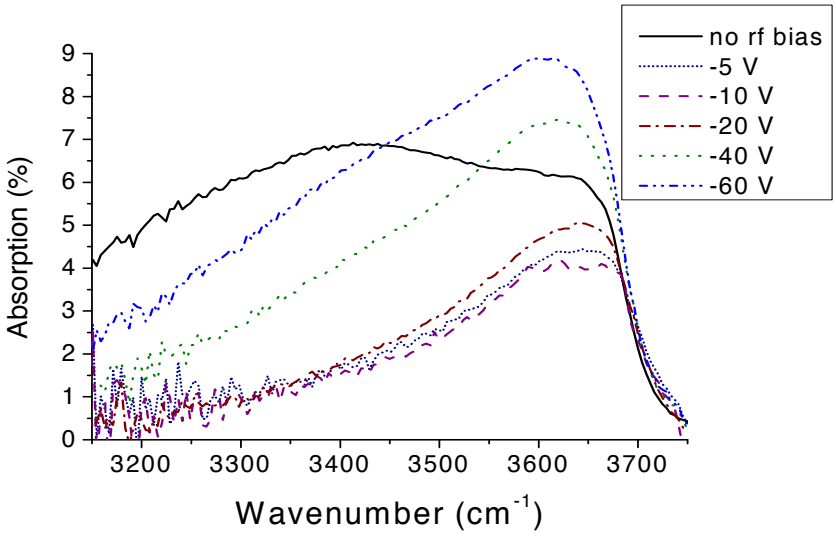

Figure III-26. Thickness normalized Si-OH absorption of SiO_2 films deposited using the vertical jet injection system, at different RF substrate bias values.

The RF bias series of films deposited with the vertical jet were etched chemically in a [HF(48%) : HNO_3(70%) : H_20 = 3:2:60] p-etch solution. Figure III-27 shows the etch results and the corresponding Si-OH peak position shift of the films, from the associated vibration mode to the isolated Si-OH vibration band. Applying any RF bias to the substrate is found to lower the p-etch rate significantly, suggesting an increase in the density of the film. The p-etch rate results are comparable to values of films deposited in other HDP systems [22,28-31].

The QMS measurements of the oxygen and silane consumptions are shown in Figures III-28. While the O_2^+ ratio remained constant with changes in the substrate bias, the SiH_2^+ ratio was found to decrease slightly, thus pointing to an increase in the silane precursor's consumption.

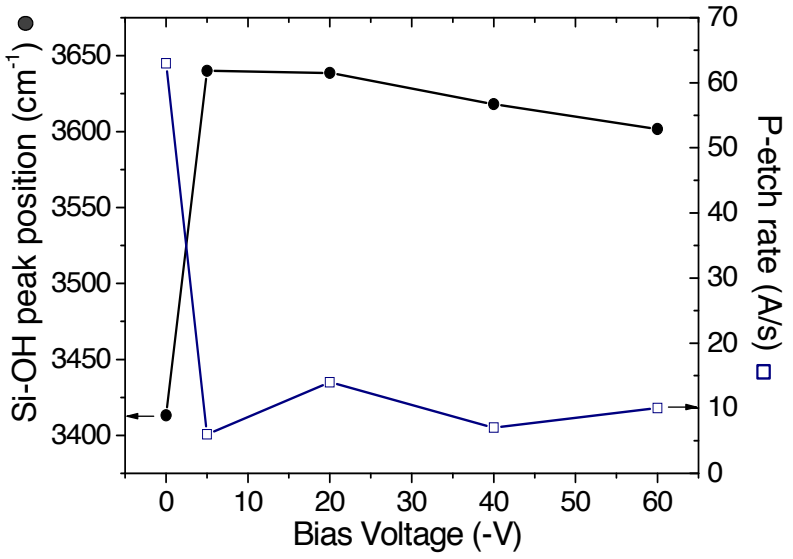

Figure III-27. Si-OH peak position and P-etch rate for depositions done with different substrate bias values. The vertical capillary jet was used.

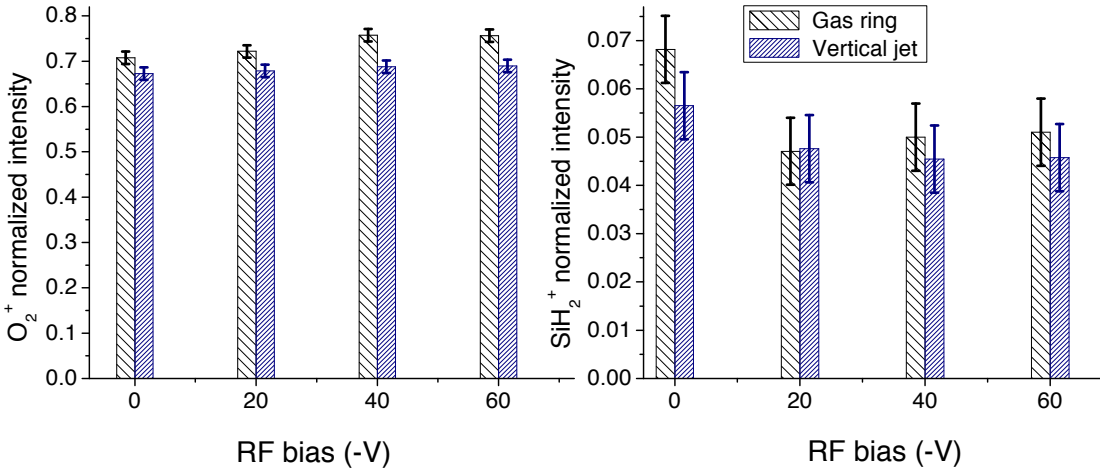

Figure III-28. The consumptions of O_2 and SiH_4 when using either a gas ring, or a vertical capillary tube for the precursor injection and varying the substrate bias.

Figure III-29 shows AFM images of two SiO_2 depositions done with the vertical jet injection. The rms roughness when no substrate bias was applied was 1.3nm and can be seen in Figure III-29(i). Applying a -10V bias to the substrate holder (Figure III-29(ii)) did not influence the rms roughness.

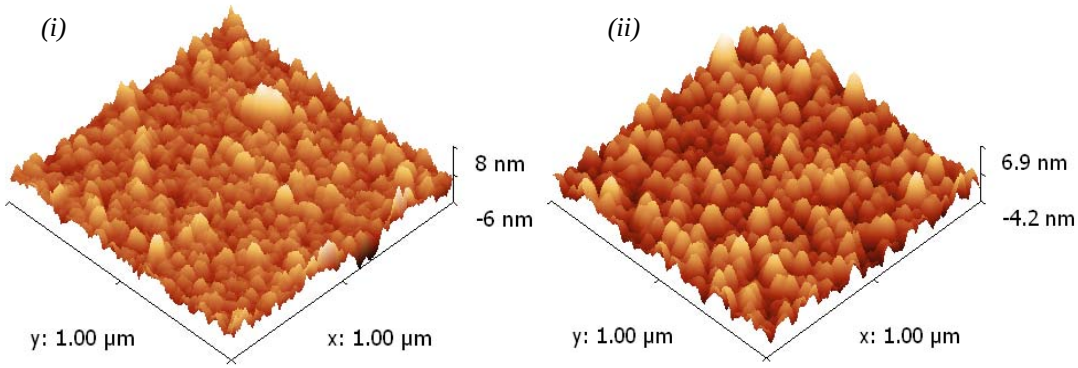

Figure III-29. AFM images of SiO_2 depositions done with the vertical capillary jet for injecting the SiH_4 precursor gas, with *(i)* no applied rf substrate bias and *(ii)* -10V rf substrate bias.

III-5 Conclusion

As evidenced from a large number of publications, high density low pressure plasmas are very sensitive to the nature of the precursors and the process parameters [1,32,33] . While having the same power input into the plasma and the same process pressure and precursor flows, subtle specifics - such as the residence time in the reactor, the state of the walls, the direction of the injection of precursors, the type of pumps used (as the pumping speed for different gases may vary for different makes and models of pumps not based on the volume displacement principle) - can not only have an influence on the deposition or etching rates, but can also drastically affect the nature of the process. In these situations it is very important to not only report all the details of the experiments, but to also take extreme care when generalizing the trends and making extrapolations onto different discharge chemistries.

This chapter presented a detailed study of the gas injection in a low-pressure high-density plasma system. Section III-2 contained a parametric study of photoresist stripping using an oxygen plasma. This study confirmed the uniformity of the active oxygen flux onto the substrate surface. In section III-3 the different silane injection systems investigated were discussed and their influence on the precursor flux and deposition rate shown. The well-mixed reactor hypothesis was discarded at the hand of experimental evidence, which shows the occurrence of beam-like transport of the silicon precursors. In section III-4, using the different jet injection systems and studying the associated Si-OH content of

the material at different points on the substrate, it was possible to separate the influence of the water-rich atmosphere created during the SiH_4/O_2 deposition plasma from the influence of the primary silane flux at distinct points on the depositing surface. This study of the non-uniform SiO_2 films shows that the primary silane flux has a large influence on the deposition, which suggests that the correct positioning of the silane injection point is vital for optimizing both the deposition rate and the quality of the films. The remainder of the chapter focused on how the changes in the process parameters influence the films silanol content, deposition rate and oxygen and silane consumption for the different injection systems. A low RF bias applied to the substrate holder was found to be an effective method for reducing the associated Si-OH vibration mode content in the film.

References

[1] R. Botha, B. Haj Ibrahim, P. Bulkin, B. Drévillon, J. Vac. Sci. Technol. A, 26 (2008) 1115.

[2] Towne Technologies, Inc., http://townetech.com/shipley.htm

[3] M.A. Lieberman, A.J. Lichtenberg, *Principles of Plasma Discharges and Materials Processing, 2nd ed.*, John Wiley & Sons, Hoboken, New Jersey (2005).

[4] D.A. Carl, D.W. Hess, M.A. Lieberman, J. Appl. Phys., 68 (1990) 1859.

[5] S. Hiyama, T. Ono, S. Lizuka, N. Sato, Plasma Sources Sci. Technol., 5 (1996) 299.

[6] J. Pelletier, Y. Arnal, O. Joubert, Appl. Phys. Lett., 53 (1988) 1914.

[7] T.C. Paulick, J. Vac. Sci. Technol. A, 21 (1982) 1032.

[8] J.A. Theil, J. Vac. Sci. Technol. A, 13 (1995) 442.

[9] D. Daineka, P. Bulkin, G. Girard, J.-E. Bourée, B. Drévillon, Eur. Phys. J. Appl. Phys., 26 (2004) 3.

[10] T.P. Ma, IEEE Trans. Electron Dev., 45 (1998) 680.

[11] A.Y. Kovalgin, G. Isai, J. Holleman, J, Schmitz, J. Electrochem. Soc., 155 (2008) G21.

[12] S.M. Han, E.S. Aydil, Thin Solid Films, 290-291 (1996) 427.

[13] Han, E. Audil, J. Electrochem. Soc., 144 (1997) 3963.

[14] C. Charles, J. Phys. D: Appl. Phys., 36 (2003) 1.

[15] E. Meeks, R.S. Larson, P. Ho, C. Apblett, S.M. Han, E. Edelberg, E.S. Aydil, J. Vac. Sci. Technol. A, 16 (1998) 544.

[16] A.Y. Kovalgin, A. Boogaard, I. Brunets, J. Holleman, J. Schmitz, Surf. Coat. Technol., 201 (2007) 8849.

[17] O. Humbach, H. Fabian, U. Grzesik, U. Haken, W. Heitmann, J. Non-Cryst. Solids, 203 (1996) 19.

[18] A. Gupta, G.N. Parsons, J. Vac. Sci. Technol. B, 18 (2000) 1764.

[19] S.M. Han, E.S. Aydil, J. Vac. Sci. Technol. A, 14 (1996) 2062.

[20] S.C. Deshmuck, E.S. Aydil, Appl. Phys. Letters, 65 (1994) 3185.

[21] A. Goullet, C. Vallee, A. Granier, G. Turban, J. Vac. Sci. Technol. A, 18 (2000) 2452.

[22] K. L. Seaward, J.E. Turner, K. Nauka, A.M.E. Nel, J. Vac. Sci. Technol. B, 13 (1995) 118.

[23] D. Goghero, A. Goullet, J.P. Landesman, Solid-State electron., 49 (2005) 369.

[24] S.P. Shufflebotham, M Weise, D. Pirkle, D. Denison, Materials Sci. Forum, 140-142 (1993) 255.

[25] S.E. Lassig, J.D. Tucker, Microelectr. J., 26 (1995) xi.

[26] D. Daineka, P. Bulkin, G. Girard, B. Drévillon, J. Vac. Sci. Technol. A, 22 (2004) 36.

[27] G. Lucovsky, P.D. Richard, D.V. Tsu, S.Y. Lin, R.J. Markunas, J. Vac. Sci. Technol. A, 4 (1986) 681.

[28] C. Charles, R.W. Boswell, J. Appl. Phys., 84 (1998) 350.

[29] C. Charles, G. Giroult-Matlakowski, R.W. Boswell, A. Goullet, G. Turban, C. Cardinaud, J. Vac. Sci. Technol. A, 11 (1993) 2954.

[30] C. Charles, R.W. Boswell, H. Kuwahara, Appl. Phys. Lett., 67 (1995) 40.

[31] N.Jiang, B. Aguis, M.C. Hugon, J. Olivier, M. Puech, J. Appl. Physics, 76 (1994) 1847.

[32] M. Calafat, D. Escaich, R. Clergereaux, P. Raynaud, Y. Segui, Applied Physics Letters, 91 (2007) 181502.

[33] P. Roca i Cabarrocas, P. Bulkin, D. Daineka, T.H. Dao, P. Leempoel, P. Descamps, T. Kervyn de Meerendré, J. Charliac, Thin Solid Films, 516 (2008) 6834.

Chapter IV

Direct Simulation Monte Carlo modeling

IV-1 Overview of the DSMC technique

Continuum models making use of the conservation equations, model a gas flow at the macroscopic level, that is to say the gas is considered to be a continuous medium and is described in terms of spatial and temporal variations of the velocity, density, pressure and temperature [1]. Gas flows can however also be modeled at the microscopic (molecular) level, which entails considering the gas as discrete molecules with specific positions and velocities at a given time and solving the Boltzmann equation for the velocity distribution function. A physical or direct simulation approach can also be used in this case, due to the discrete nature of the gas at the microscopic level [1]. DSMC is consequently a tool for the analysis of practical, non-linear gas flows at the molecular level[1,2].

In the DSMC technique, a large number of statistically representative particles* are tracked. The motion and interaction (both elastic and inelastic) of these particles lead to changes in their velocities, positions and chemical composition, while taking mass, momentum and energy conservation into account[3-5]. The key approximation of DSMC is “to uncouple the molecular motions and intermolecular collisions over small time intervals” [5]. This allows one to model the motion of the particles deterministically while the treatment of collisions is of a statistical nature. This probabilistic process of simulating the collisions is the major difference between DSMC and molecular dynamics. The technique is based on dividing the

* Each simulated particle has the properties of one molecule, and is statistically respresentative of a larger amount of molecules. It is not simulated as a cluster of molecules, but as a single molecule.

simulated region into a grid of cells. The local collision rates are calculated for each cell. An adequate number of collisions are then simulated by randomly selecting molecule pairs in each cell [5]. Collisions between molecules are modeled using either a Variable Hard Sphere (VHS) model or more complex models.

The DSMC method thus allows one to simulate gases using a probabilistic approach [5]. The computational burden is however more affordable for dilute gases. It has been used with great success to model problems in rarefied gas[3,4,6-14], such as the gas flow around the substrate in low pressure CVD processes used for semiconductor growth. As it is straightforward to implement and can easily be adapted, it is ideally suited for solving engineering physics problems. In deposition and CVD systems, the precursor transport of the plasma excited species to the substrate, their interactions with surfaces and the removal of the created by-products can be modeled. These simulations allow one to predict the gas phase composition near the substrate, which is of utmost importance to ensure greater control of the film's growth process and quality.

IV-2 Details of the implementation of the technique

The DSMC method [1] is very efficient if a system falls in the transition flow regime[2], defined as having a Knudsen number, the ratio of the mean-free-path λ, and the characteristic length L, between 0.1 and 10. The characteristic

dimensions of low pressure, high density plasma systems are mostly larger than the mean free path of the precursor gas, but in some cases it is better to make use of a local Knudsen number, where *L* can be a length scale of the macroscopic gradients in temperature, pressure, density or velocity[5]. Alternatively, DSMC can be described as being suitable for modeling dilute fluids if the ratio of the mean-free-path to the molecular diameter[5] is at least $\lambda/d \geq 10$. In addition to this, systems may have large pressure gradients in them, with continuum equations only being accurate in certain parts of the system. The DSMC method is of particular interest in these cases, as it is applicable over a large range of Knudsen numbers.

Figure IV-1 shows a flow chart of the DSMC procedure. Initially, a set of conditions are used to describe the particles velocities and positions. The boundary conditions of the system are also defined. The procedure then moves through the different steps of moving the particles, indexing and cross-referencing them, sorting the particles into a grid of cells and simulating the collisions, and finally sampling the flow field [1, 5]. Several factors should be taken into account to ensure the accuracy of the results obtained from a DSMC model. The global time step increment Δt_g must be chosen to be less than the mean collision time, and the linear cell dimensions in each spatial direction must be smaller than the mean-free-path λ [1]. The cell dimensions are of particular interest in order to correctly predict the large gradients of the macroscopic flow variables. Also, as the collision partners are taken randomly from the same cell, they should ideally be nearest neighbours. The statistical error in the sampled macroscopic flow properties is given to be inversely proportional to the square

root of the total number of simulated particles. If the value of the ratio of the actual number of particles (calculated from the given value of pressure) to the simulated number of particles is too high, it can lead to too high levels of statistical scatter. It is recommended to keep this value within the range of [5] 10^{14} to 10^{18}. Proper boundary conditions determine the accurate treatment of the particle-surface interactions and can be a determining factor of the model's success. The boundary conditions of the vacuum system must take into account that the impinging particles at the walls can be reflected elastically (specular reflection) or inelastically (diffusive reflection), can stick to the surface or create a new particle. The outflow region should likewise remove particles from the system. In the case of diffuse reflection the reflected molecules normal velocity components are distributed with a Maxwellian distribution based on the temperature of the surface from which it is reflected[5].

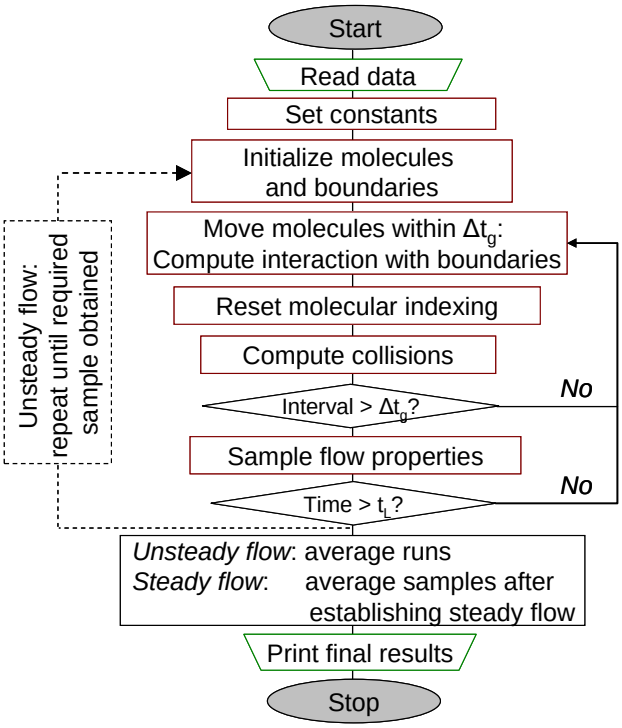

Figure IV-1. Flow chart of the DSMC method [5].

For collisions between molecules, either a relatively simple hard-sphere model or more complex models can be used. The variable hard-sphere (VHS) model is considered to be an accurate representation of the total collision cross section and is very popular due to its ease of use[5]. In the VHS model a hard sphere molecule, with a diameter *d* that is a function of the relative velocities of the colliding species c_r and the viscosity-temperature index ν, is used. It is given by[1]

$$d = d_{ref}\,(c_{r,ref} / c_r)^{\nu} \qquad \textit{(IV-1)}$$

Where the subscript *ref* denotes reference values for the thickness and relative velocities.

Though chemical reactions (in a kinetic sense) can be treated in the DSMC model, it falls outside of the scope of this thesis and only a simple phenomenological treatment is realized here.

The FORTRAN software using the DSMC technique is included with G.A. Bird's book[1] entitled "*Molecular Gas Dynamics and the Direct Simulation of Gas Flow*", with the latest corrections available from the author's website[15]. This code was modified according to the process conditions, capillary and reactor geometries. In order to estimate the velocity at which the SiH_4 precursor gas exits from the capillary tube into the vacuum chamber, the gas flow through the capillary tube used during experiments is modeled. DSMC calculations are then implemented to model the flux of the SiH_4 and O_2 precursor gases onto the substrate plane. This supplies information on the spatial distribution of the reactant gases near the substrate surface. The experimentally determined quantity of silicon that is

incorporated into the growing film is compared with the simulated silane molecule fluxes onto the surface. The following section will show the modeled capillary tube and the simulation results obtained, after which the modeled vacuum chamber and its simulation results will be presented.

IV-3 The capillary gas injection tube

A first order estimate of the maximum velocity with which gas can exit from the capillary jet can be obtained from the one-dimensional equations for isentropic[†] flow of a compressible fluid:

$$\frac{P_0}{P_d} = \left[1 + \frac{\gamma - 1}{2} M^2\right]^{\gamma/(\gamma-1)} \qquad \textit{(IV-2)}$$

$$U = M\sqrt{\gamma R_s T} \qquad \textit{(IV-3)}$$

where P_0 is the pressure at the capillary tube's entrance, P_d - the pressure at the exit, γ - is the ratio of specific heat capacities[‡], M - the Mach number, U - the gas stream speed (m/s), T - the absolute temperature (K) and R_s - a specific gas constant, which for SiH_4 equals 260 $J \cdot kg^{-1} \cdot K^{-1}$.

[†] An isentropic flow is adiabatic and reversible, meaning no energy is added or lost due to, for example, friction.

[‡] This is the ratio of the heat capacity at constant pressure (C_P) to the heat capacity at constant volume (C_V). It is also sometimes called the adiabatic index. For ideal diatomic gases that have no variations in C_p and C_v with temperature, $\gamma = 7/5$.

The existence of multidimensional shock waves downstream of the jet, the "zone of silence" where there are supersonic velocities and a "Mach disk" at which the gas has a rapid decrease in velocity to less than Mach = 1, makes it impossible for the above equation to accurately predict the gas velocity[16]. Using a very low pressure value for P_d in equation (IV-2) will lead to a very large Mach number. Figure IV-2 shows a schematic of the capillary tube which has the same cross section diameter along the axis, so it can not be considered as a convergent-divergent nozzle. It is known from fluid dynamics that choked flow or Mach = 1 conditions will exist at the exit of the capillary tube. The velocity at the exit will consequently be less than or equal to that at Mach = 1, which is equal to 288 m/s in our conditions, when using equation (IV-3). Hence, increasing the capillary pressure ratio further will not increase the exit Mach number above unity.

The exact velocity at which the SiH_4 precursor gas exits from the capillary tube into the vacuum chamber is consequently needed, as it is necessary for the accurate simulation of the precursor flow in the vacuum chamber and the flux of the different molecules onto the substrate surface, which will be shown in Section IV-4. The rarefied gas flow of silane through the capillary tube used during the experiments shown in Chapter III was thus simulated using the DSMC method.

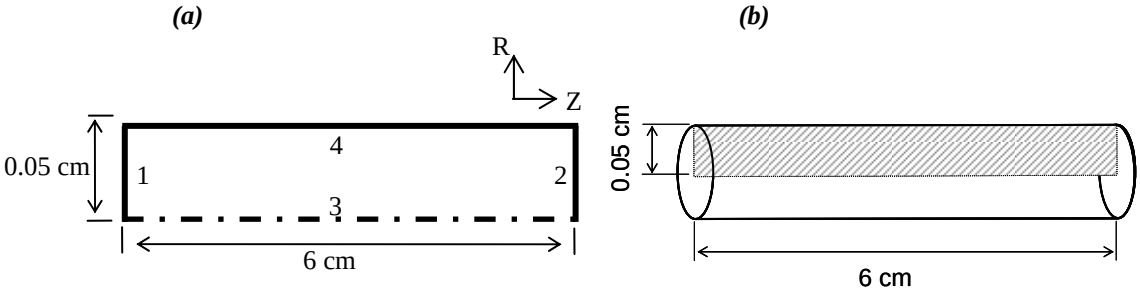

Figure IV-2. ***(a)*** **2D and** ***(b)*** **3D Schematic of the capillary tube, with a radius of 0.05 cm and length 6 cm.**

IV-3.1 Model and computational results

The capillary flow is axisymmetric and because of this symmetry, the three dimensional flow can be treated as two dimensional in the R-Z plane, with collisions being treated as 3 dimensional events. As indicated on Figure IV-2 *(a)*, the boundaries were defined as *1)* the SiH_4 stream, *2)* the vacuum end of the capillary, *3)* the axis of the capillary tube and *4)* the capillary wall, which is a diffusively reflecting surface. The simulated region shown in Figure IV-2 *(a)* is divided into a grid of 80 elements in the radial (*R*) direction, and 800 elements along the z-axis of the capillary tube, which forms 64 000 cells. This is shown schematically in Figure IV-3, for the case of *(a)* a uniform grid (UG) of cells and *(b)* a non-uniform grid (NUG) of cells. Each cell represents a circular element around the axis of the capillary tube.

According to Bird [1], the most severe practical problem associated with DSMC simulations making use of axially symmetric flows is the difference in sample size between the cell at the axis and the outermost cell. To overcome this problem, either a weighting factor can be added to make sure the distribution of particles over the cells is equal, or a non-uniform grid can be used, as shown in Figure IV-3*(b)* with the vacuum end of the capillary tube located at 6cm. The change in the radial and axial cell dimension is indicated on the figure. The largest cell in the radial (*R*) direction is located at the capillary axes, at boundary number 3 on Figure IV-2*(a),* and the largest cell in the axial (Z) direction, at the SiH_4 stream boundary, number 1.

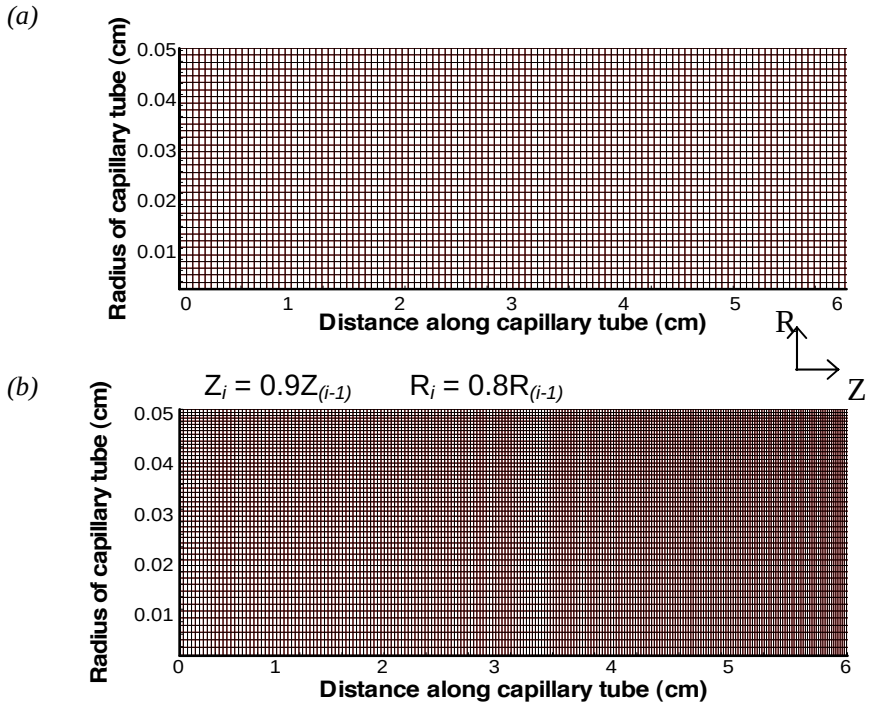

Figure IV-3. (a) Uniform and (b) non-uniform grid used during simulation of the capillary jet injection system.

For the purpose of the simulation, the pressure in the capillary tube used in Chapter III was measured at different silane flows, as can be seen in Figure IV-4. For comparison with experimental results, a value of 8 sccm SiH_4 was chosen in the simulations, which relates to a 5.1 Torr pressure in the capillary tube, and makes it possible to calculate the speed V_{FX} with which the gas is injected into the capillary tube, as

$$V_{FX} = \frac{Gasflowrate_{5.1Torr}[m^3/s]}{CrossSectionArea_{Capillary}[m^2]} = 25.3m/s$$

A rule of thumb when choosing the time step is that it should be less than a third of the time the molecule takes to traverse its mean free path. At the 5.1 Torr pressure used, the mean free path λ_{MFP} is 80 μm that gives a mean free path

time of 3.16 μs. The time step *DTM* used during the simulation was equal to 1E-8 seconds, which is well below a third of this value. Another parameter to set is the number of real molecules that are represented by each simulated particle, *FNUM*. It is recommended [3] to keep a minimum amount of between 10 to 20 particles per cell. Several simulations were run to find the ideal value of the parameter *FNUM* to ensure low statistical error in the density distribution along the capillary tube's radius. A final *FNUM* value of *2E10* molecules was chosen. When the simulation reached a steady state, a total number of ~900 000 particles were being simulated. Table IV-1 shows other user-configurable parameters used in the developed DSMC model. The initial state in the capillary tube was set to vacuum. The simulation was consequently run until a steady state was obtained.

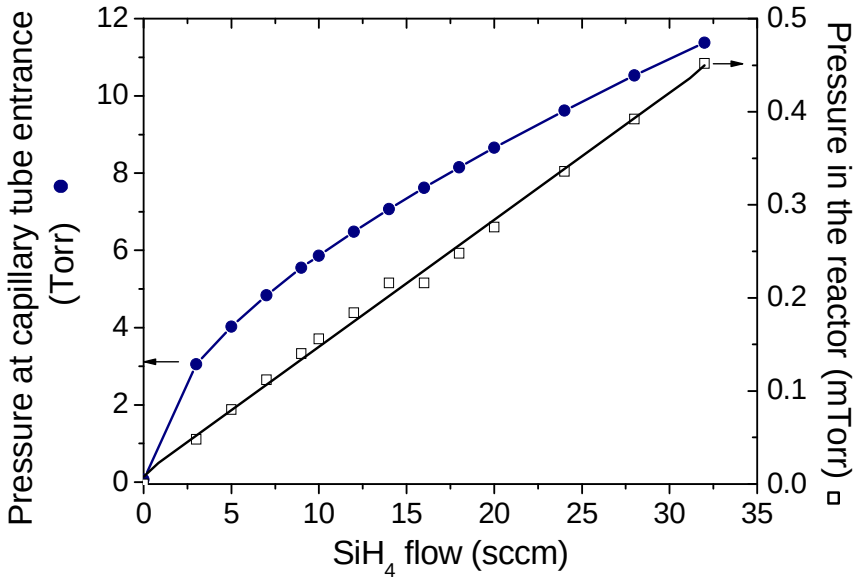

Figure IV-4. Pressure measurements at the entrance to the capillary tube and in the reactor chamber.

Parameter	**Value**
Reference diameter of SiH_4	4.722E-10 m
Reference temperature of SiH_4	273 K
Molecular mass of SiH_4	5.3E-26 kg
Viscosity of SiH_4	0.8826
Variable Hard Sphere or Soft Sphere	VHS

Table IV-1. DSMC model parameters used for simulating the capillary tube.

The results of simulating the above structure are shown in Figure IV-5 at the vacuum end of the capillary tube, where there are large gradients of the velocity field, density and temperature.

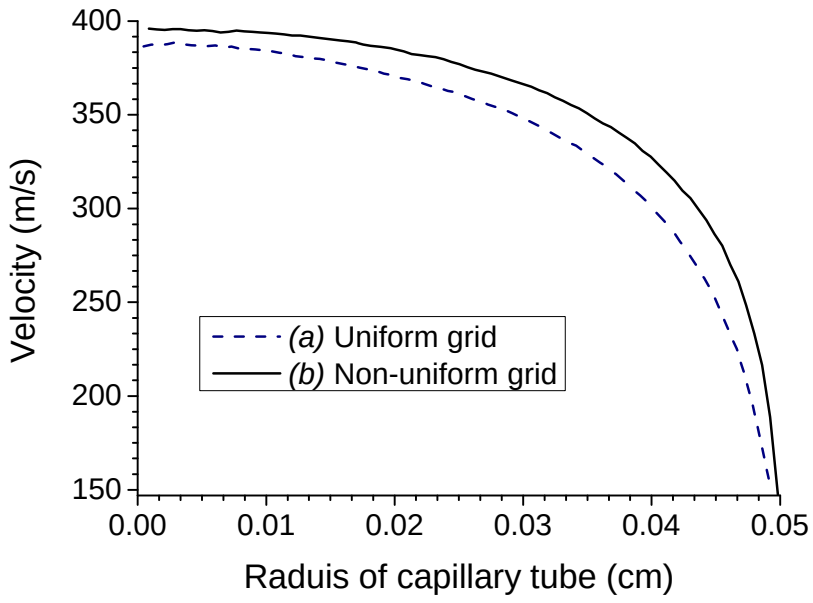

Figure IV-5. Exit velocity of the simulated particles from the capillary tube, using both the *(a)* uniform and *(b)* non-uniform grids shown in Figure IV-3.

The lower value of the exit velocity for the simulation run with a UG is due to the fact that the cell dimensions exceed the mean free path value and the exit velocity was sampled over a bigger particle set, which contains more slow particles than when using a smaller cell size such as for the NUG. Due to this the value of the exit velocity was underestimated in the case of a UG. The density, velocity stream traces and temperature distribution in the capillary tube can be seen in Figure IV-6 for the simulation performed with a NUG.

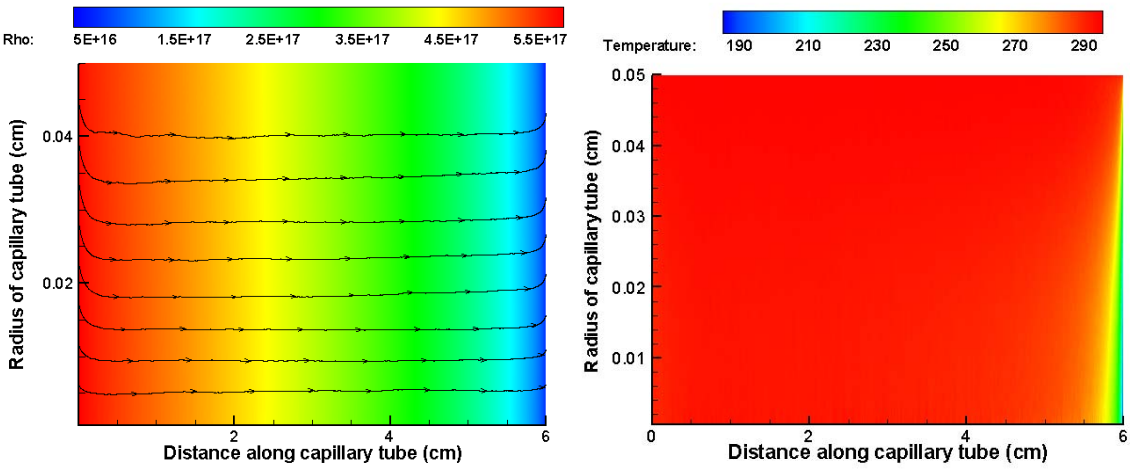

Figure IV-6. *(a)* Density [molecules/cm^3], stream traces and *(b)* temperature [°K] of the stream in the capillary tube. The simulation was done for 30 ms with a NUG.

By using the results shown in Figure IV-5 and taking the density distribution of the silane molecules along the radius of the capillary into account, the average velocity of the gas stream exiting the capillary tube was calculated to be 255 m/s. This value was consequently used for the SiH_4 jet injected into the reactor chamber, as discussed in the following section.

IV-4 Reactor chamber

The DSMC code was modified to model the injection of the SiH_4 precursor from the capillary tube into the vacuum system. This can be computed in a reasonable time and compared with real deposition profiles. However, the question that arises is how gas flow simulations may be relevant to the prediction of the behaviour of a plasma process, and how it can assist with the analysis of the results of a real deposition process.

In the reactor configuration which makes use of a capillary tube for the SiH_4 injection, the flux of SiH_4 is the biggest source of non-uniformity in the deposition rate across the sample. Due to the position of the capillary at a distance from the substrate which is close to the mean free path, a very low electron temperature and a rather low electron density in the proximity of the substrate can be expected, due to multipolar confinement of the fast electrons in the source area[17]. For a hydrogen plasma at comparable conditions[17] values of approximately 1 eV for the electron temperature and $2 \cdot 10^{10}$ cm^{-3} for the electron density have been reported. No considerable dissociation in the primary flux of SiH_4 is consequently expected. Indeed, most of the dissociation and ionization take place in the ECR zones in the antenna plane, located 10 cm above the substrate holder. The contribution of species created in the antenna region to the deposition rate may however be expected to be quite uniform at the substrate plane, as was evidenced by the uniform etch profiles observed in an O_2 plasma (Section III-2) and the uniform deposition of SiO_2 when using a gas distribution

ring for the injection of SiH_4 (Section I-1.4.1). Though gas flow simulation is certainly a crude approximation for the prediction of a plasma process, it does allow one to observe the trends of the fluxes of H_2O and SiH_4 onto the wafer and how they affect the deposition of SiO_2.

For the purpose of the simulation, the O_2 and SiH_4 flows were chosen to be 40 sccm and 8 sccm respectively, with a 3 mTorr pressure in the vacuum chamber, to make the results comparable with the experimental measurements. To simplify the model, geometric asymmetries, such as ports for SE or OES measurements, were disregarded. The user-defined model parameters were set to the values shown in Table IV-2.

Parameter	**Value**
Reference diameter of SiH_4	4.722E-10 m
Reference temperature of SiH_4	273 K
Molecular mass of SiH_4	5.3E-26 kg
Reference diameter of O_2	3.558E-10 m
Reference temperature of O_2	273 K
Molecular mass of O_2	5.3E-26 kg
Viscosity of SiH_4	0.8826
Viscosity of O_2	0.77
SiH_4 reactive sticking coefficient	Varied
Variable Hard Sphere or Soft Sphere	VHS

Table IV-2. User-defined DSMC model parameters.

IV-4.1 Model and computational results

The volume of the system that was initially modeled can be seen in Figure IV-8. For the schematic in Figure IV-8 a SiH_4 and O_2 gas mixture was used without taking the production of H_2O into account and surface 5 was considered to be a diffusively reflecting surface for all molecules coming into contact with it.

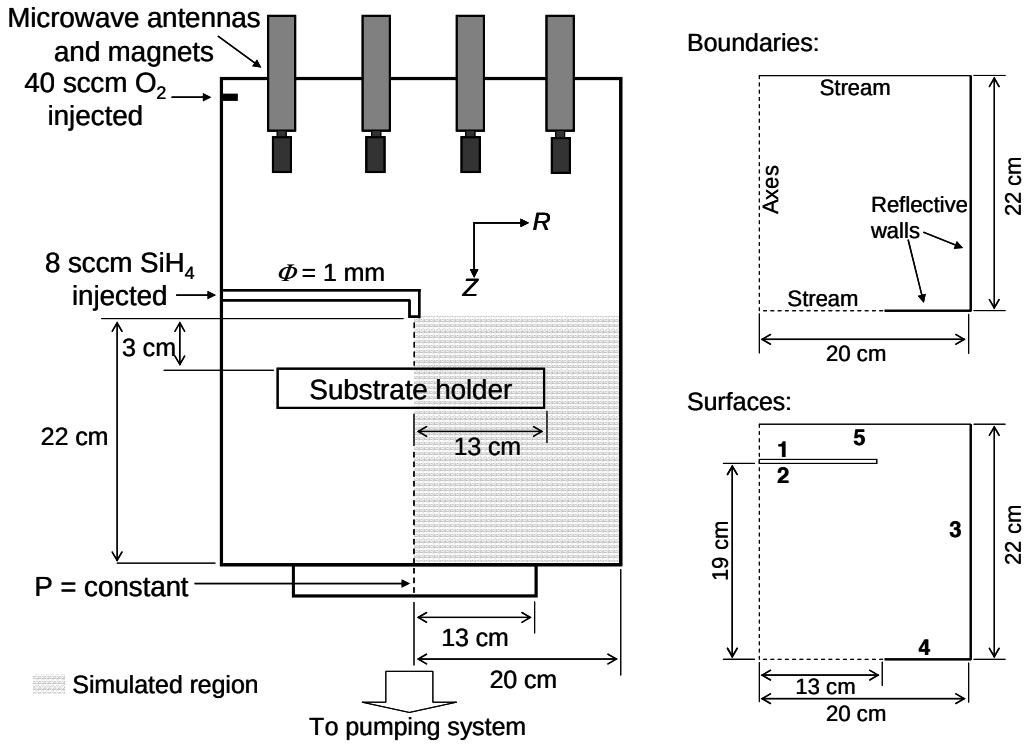

Figure IV-8. 2D model of the volume of the reactor simulated with an O_2 and SiH_4 gas mixture, indicated in grey. The boundaries and surfaces used in the simulation are shown on the right.

The simulation results of the model structure shown in Figure IV-8 can be seen in Figure IV-9 *(a)* - *(d)*. The SiH_4 and O_2 density and velocity stream traces are indicated, while the fraction of silane molecules that stuck to the various surfaces with which they came into contact was varied from 0 to 1.

The results show the uniform density distribution of O_2 in the system and the large density variation induced by even a small SiH_4 reactive sticking coefficient value (Figure IV-9 *(b)*). There are almost no SiH_4 molecules pumped out of the reactor when the sticking coefficient is set to a non-zero value (Figure IV-9 *(b)* - *(d)*). The volume of the system above the substrate holder needs to be taken into account to confirm that well-mixed conditions do not exist.

Using these results as a starting point, the model was modified in the axial direction to represent the upper part of the system as well, while not taking the antenna region into account. As shown in the simulated structure in Figure IV-10, an extra 8 cm was added above the injection point in order to make the modeled structure a more accurate representation of the experimental system.

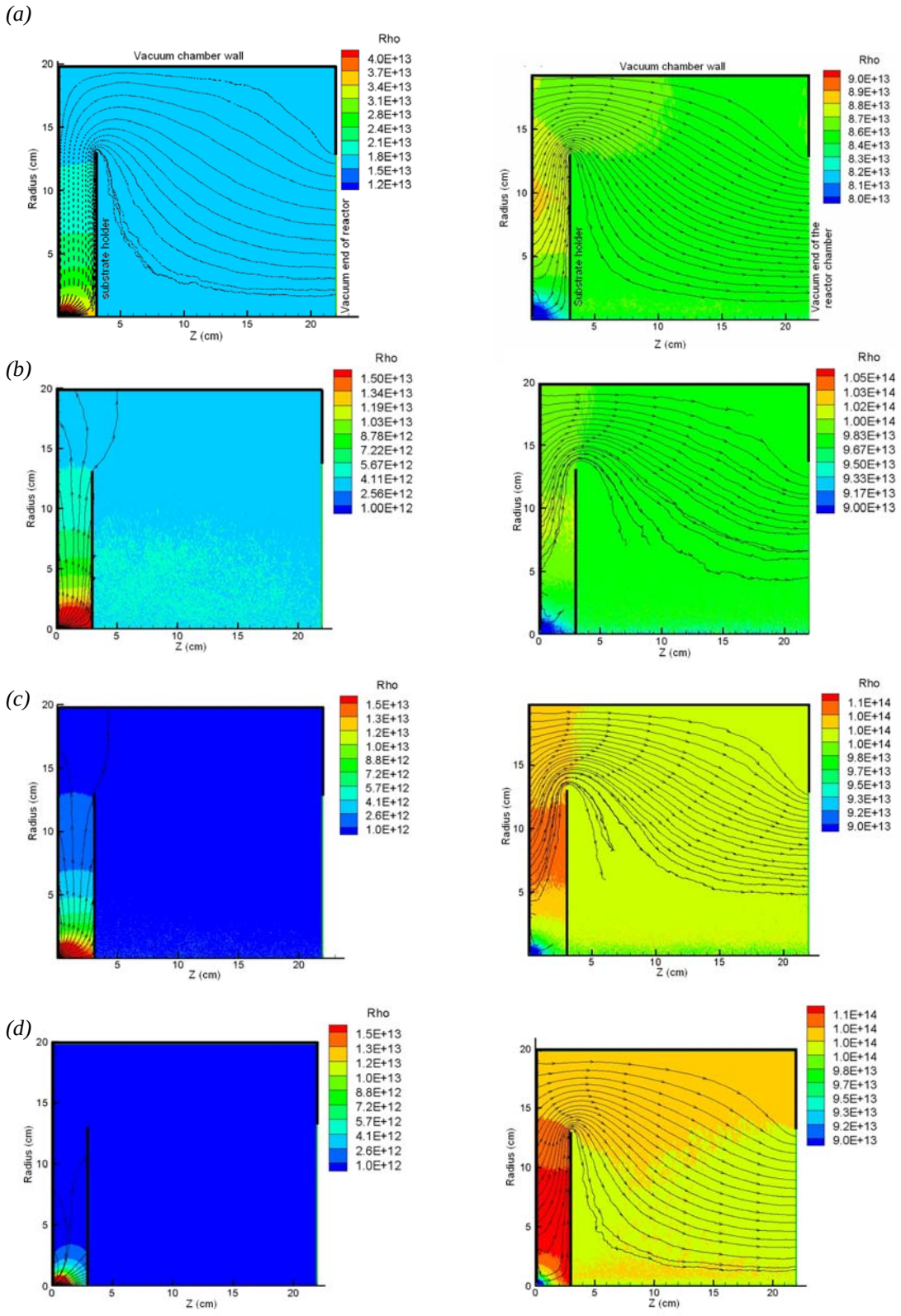

Figure IV-9. Simulated SiH_4 (left) and O_2 (right) density [molecules/cm^3] and velocity stream traces using the structure shown in Figure IV-8. The reactive sticking coefficient value for silane was set to *(a)* zero *(b)* 0.033 *(c)* 0.1 and *(d)* 1, with the exception of the back of the substrate holder where it was set to zero throughout all simulations.

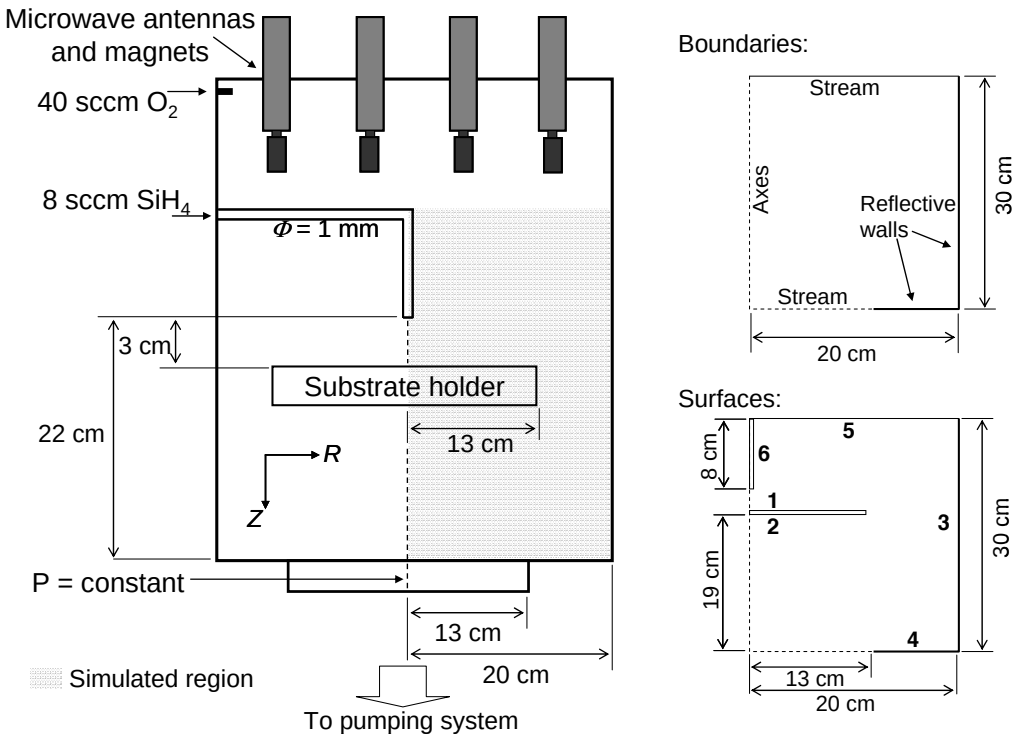

Figure IV-10. 2D model of the volume of the reactor simulated with water production incorporated, indicated in grey.

The removal of two oxygen molecules and the creation of two water molecules in their place for each silane molecule that sticks to any surface were taken into account by the balanced reaction:

$$SiH_4(gas) + 2O_2(gas) \rightarrow SiO_2(solid) + 2H_2O(gas) \qquad (IV\text{-}4)$$

The oxygen molecules are removed from the same computational cell where the silane molecule sticks to the surface. Two water molecules are then created in the cell from which the silane molecule was removed. This allows one to see the variation in the amount of silicon incorporated into the growing film and what influence it has on the oxygen distribution and the production and distribution of

water in the system. The fraction of the silane molecules sticking to the various surfaces, also referred to as the reactive sticking coefficient ρ, was varied during the different simulations.

As there was no deposition of SiO_2 observed on the back of the substrate holder (surface 2) during experiments, the reactive sticking coefficient for this surface was kept at zero in all the simulations. In addition to this, surface 5 was set to diffusively reflect oxygen molecules and to remove any silane molecules that might reach it, in other words the reactive sticking coefficient of silane for this surface was set to one and the corresponding removal of two oxygen molecules and creation of two water molecules took place for every silane molecule reaching surface 5.

The user-defined parameters for water molecules were set to the values shown in Table IV-3. The simulated flux of the H_2O, O_2 and SiH_4 species onto the substrate holder for different SiH_4 flow rates are shown in Figure IV-11 *(a)* - *(d)*.

Parameter	**Value**
Reference diameter of H_2O	2.75E-10 m
Reference temperature of H_2O	273 K
Molecular mass of H_2O	3.0E-26 kg
Viscosity of H_2O	1.16

Table IV-3. User-defined H_2O parameters used in the DSMC model.

In Section III-4 it was claimed at the hand of experimental evidence that a uniform flux of H_2O onto the substrate holder will lead to the same amount of H_2O incorporated into the growing film across the substrate. The high flux of SiH_4 – and consequently the high deposition rate - under the injection point, will then lead to a low concentration of silanol in these areas, while for the regions further away from the injection point the concentration of silanol in the deposited film will be relatively high. While the simulated SiH_4 flux in Figure IV-11 changes by almost two orders of magnitude across the substrate holder, the H_2O and O_2 flux only changes slightly, confirming the validity of the above claim.

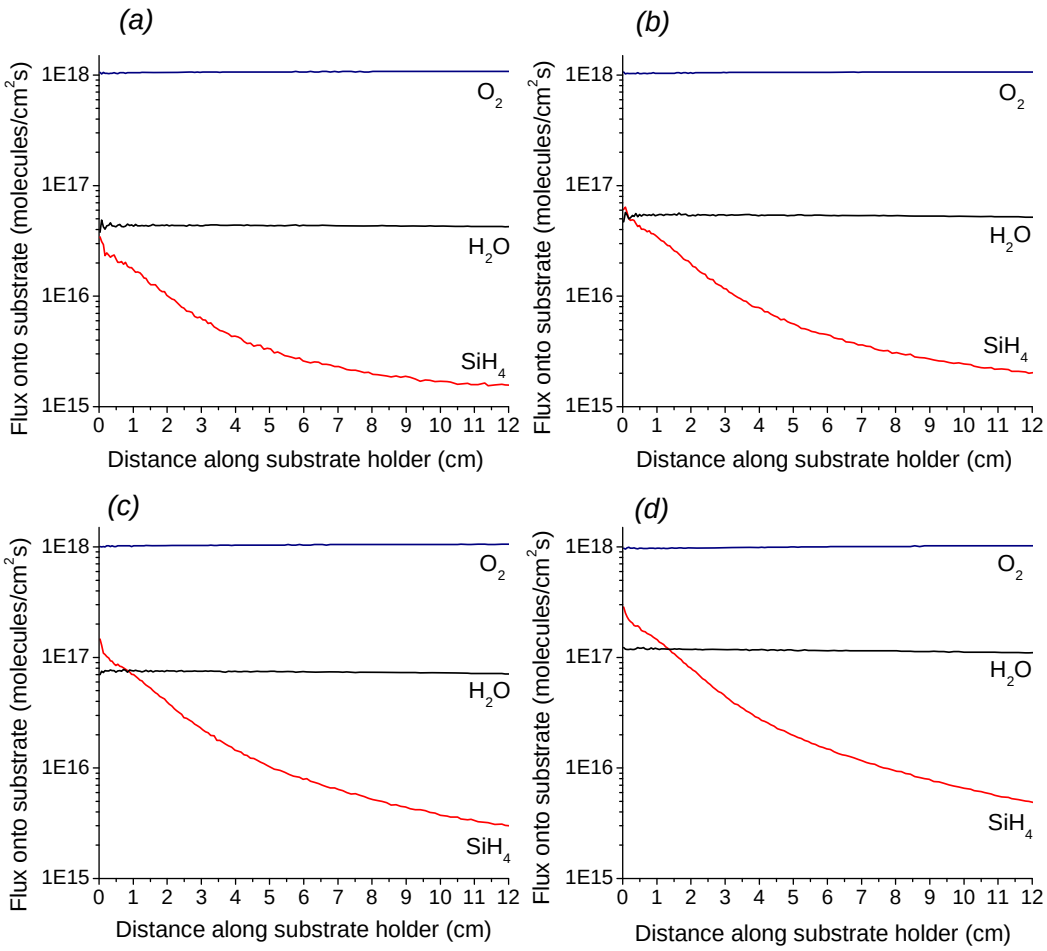

Figure IV-11. Simulated SiH_4, O_2 and H_2O flux onto the substrate holder at *(a)* 1 sccm, *(b)* 2 sccm, *(c)* 4 sccm and *(d)* 8 sccm SiH_4 flow rates.

The increase in the density of water created in the system at different SiH_4 flow rates can be seen in Figure IV-12 *(a)* - *(d)*, with the surfaces from Figure IV-10 indicated on Figure IV-12 *(b)*. The increase in H_2O production with rising SiH_4 flow rates can be clearly seen, as well as the homogeneous nature of the density distribution along the substrate surface.

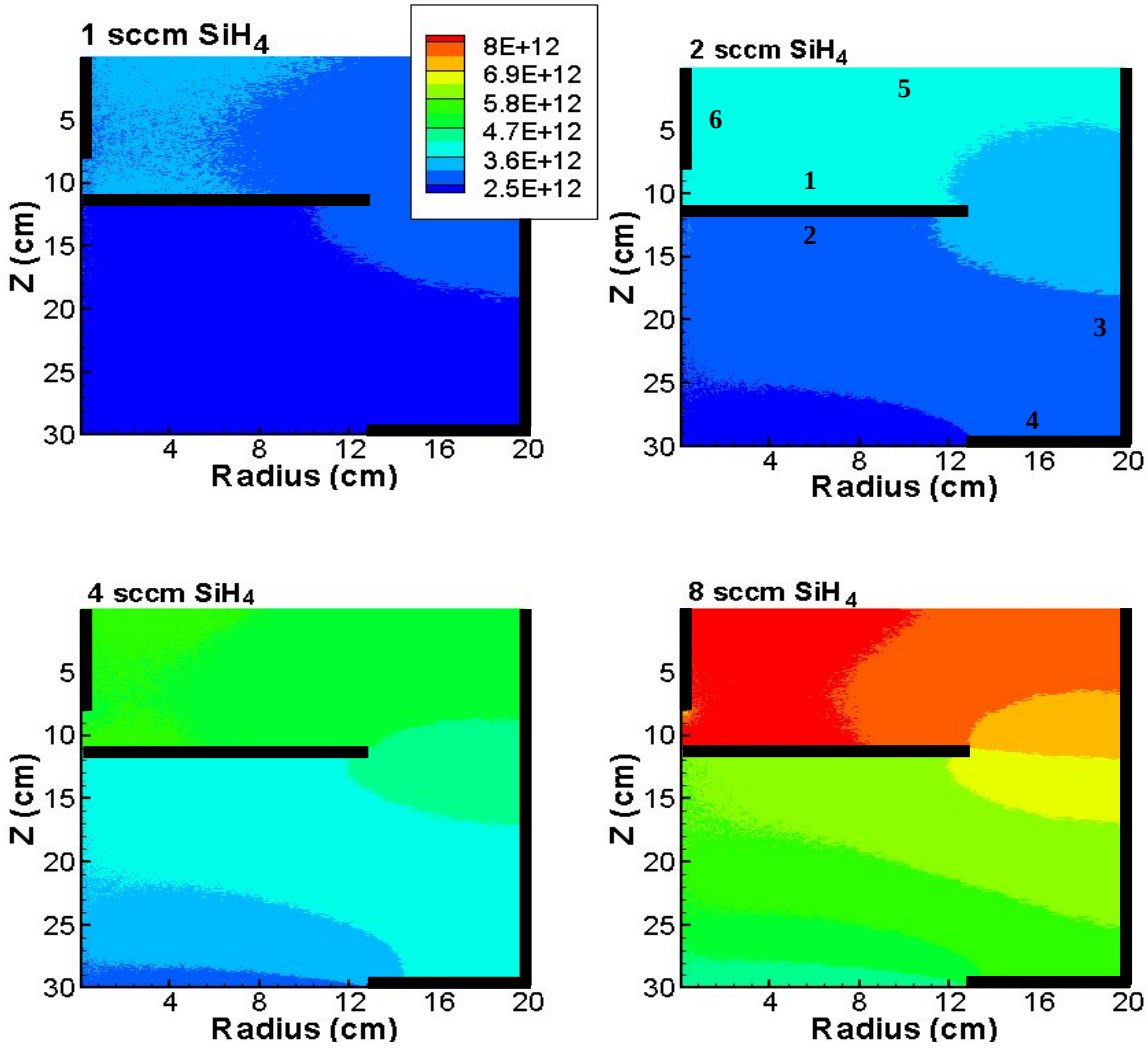

Figure IV-12. Density [molecules/cm^3] distribution of H_2O molecules at *(a)* 1 sccm, *(b)* 2 sccm, *(c)* 4 sccm and *(d)* 8 sccm SiH_4 flow rates.

The simulated SiH_4 density distributions are depicted in Figure IV-13 *(a)* - *(d)* with the surfaces defined as in the figure above. The reactive sticking coefficient value was set to 0.1 for all surfaces, with the exception of surface 5 which was set to 1. A much stronger variation in the density distribution of the SiH_4 gas can be observed than in the H_2O density shown in Figure IV-12.

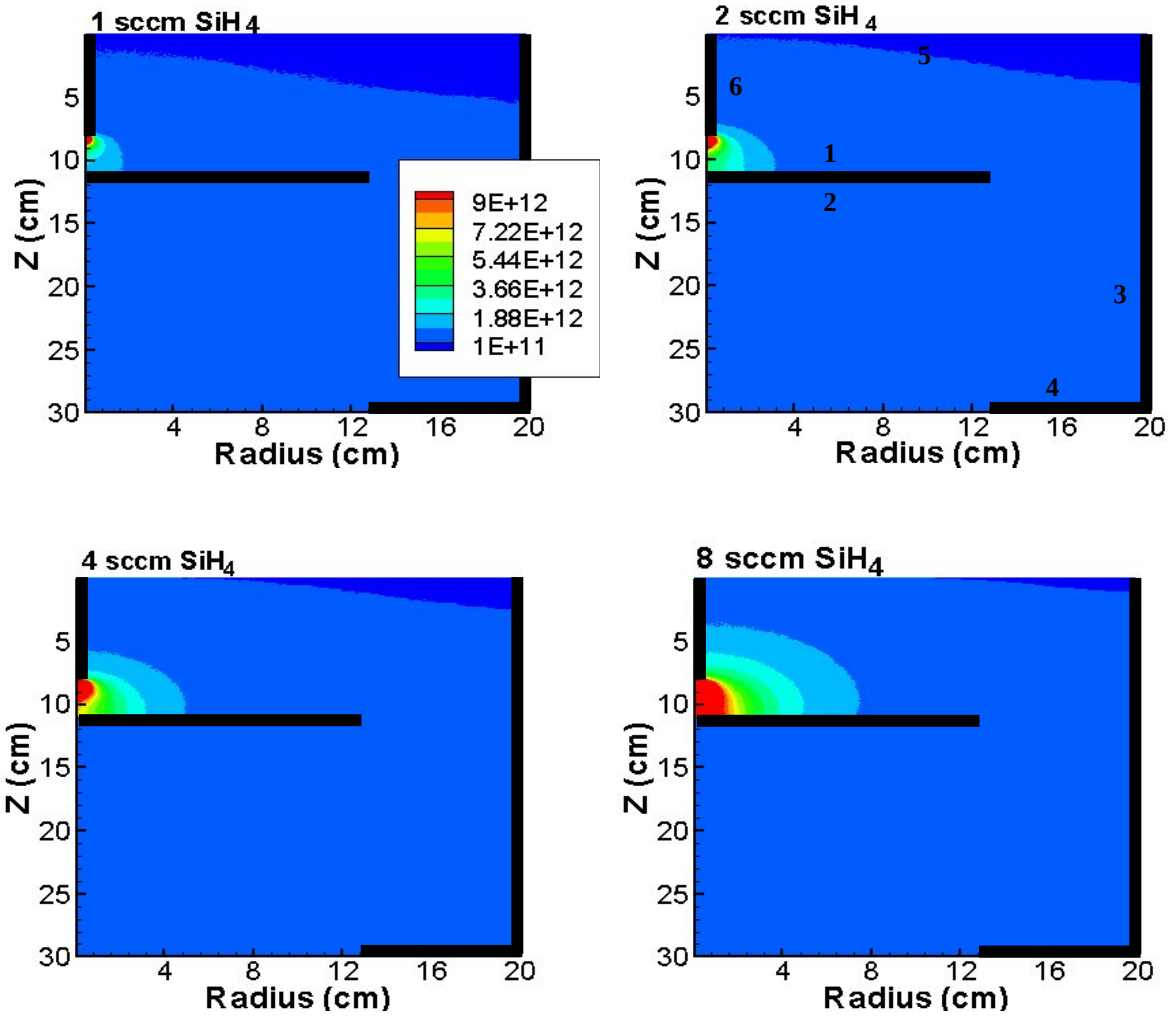

Figure IV-13. Density [molecules/cm^3] distribution of SiH_4 molecules at *(a)* 1 sccm, *(b)* 2 sccm, *(c)* 4 sccm and *(d)* 8 sccm SiH_4 flow rates.

Figure IV-14 shows the simulated quantity of SiH_4 molecules incorporated into the growing film per second, at different SiH_4 flow rates. A reactive sticking coefficient value of 0.1 was used during these simulations, with the exception of surface 5 which was set to 1.

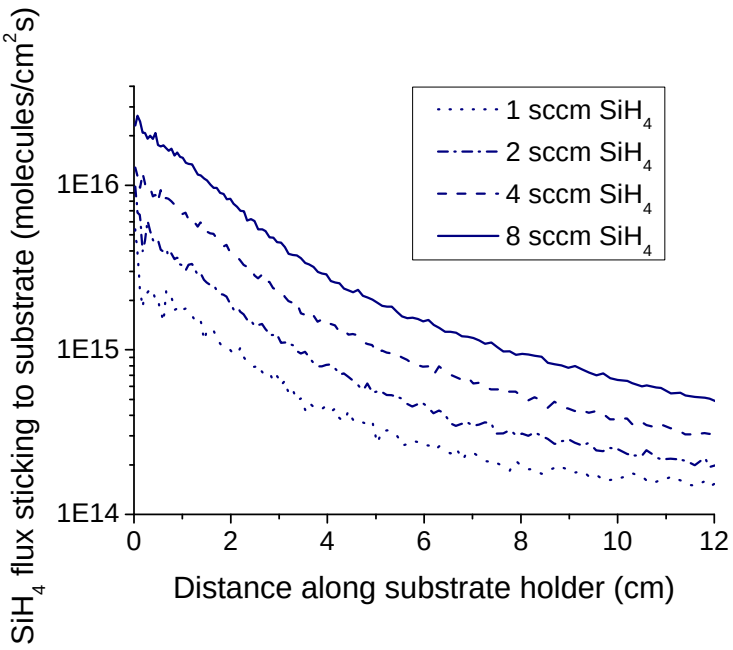

Figure IV-14. Simulation results of the SiH_4 molecules incorporated into the growing film, at different SiH_4 flow rates.

In Figure IV-15 *(a)-(d)* a comparison of the amount of silane molecules incorporated into the growing film for different reactive sticking coefficient values can be seen. Here, 8 sccm SiH_4 and 40 sccm O_2 was used for all four simulations. In *(a), (b)* and *(c)* each SiH_4 molecule that reaches surface 5, as indicated on Figure IV-10, is removed, together with two O_2 molecules, while two H_2O molecules are created in its place. The fraction of SiH_4 sticking to the other surfaces was changed between *(a)* 0.01, *(b)* 0.03 and *(c)* 0.1. The lower reactive

sticking coefficient value has the obvious effect of decreasing the fraction of silane sticking to the substrate surface, but also leads to a decrease in the gradient of the curve and thus a more uniform radial distribution of the silicon sticking to the surface. Comparing these results with the experimental values obtained for the flux of silicon atoms incorporated, as shown in Figure IV-16, it is estimated that the reactive sticking coefficient of the SiH_4 molecules is between 0.01 and 0.03. The influence of changing the reactive sticking coefficient ρ of surface 5 can be seen in Figure IV-15 for *(c)* ρ = 1 and *(d)* ρ = 0.1. While the lower amount of SiH_4 sticking to this surface will have an influence at the edge of the substrate holder, the region on which samples are placed during deposition (until a radius of 5 cm) are not influenced significantly.

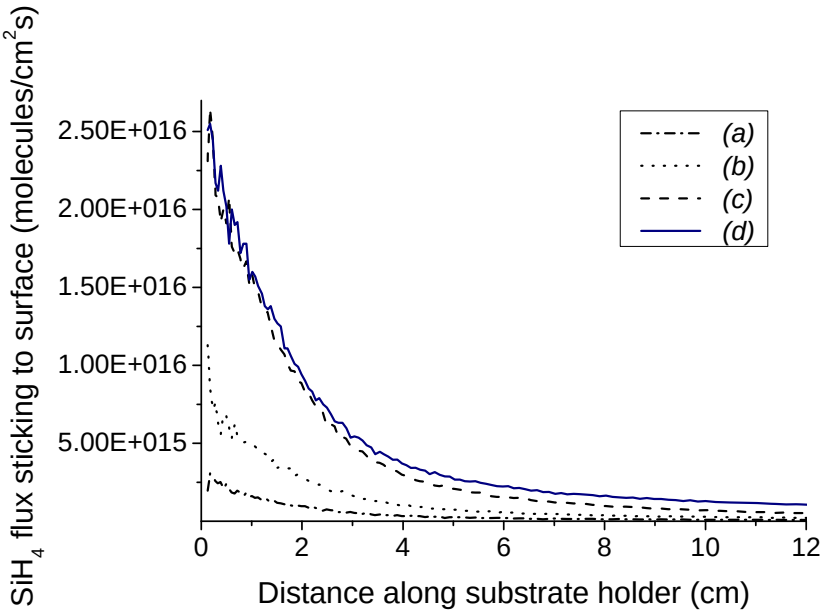

Figure IV-15. Simulated SiH_4 flux sticking to the substrate surface, for the reactive sticking coefficient set to *(a)* 1 for surface 5 and 0.01 for all the other surfaces, *(b)* 1 for surface 5 and 0.03 for all the other surfaces *(c)* 1 for surface 5 and 0.1 for all other surfaces and *(d)* 0.1 for all surfaces.

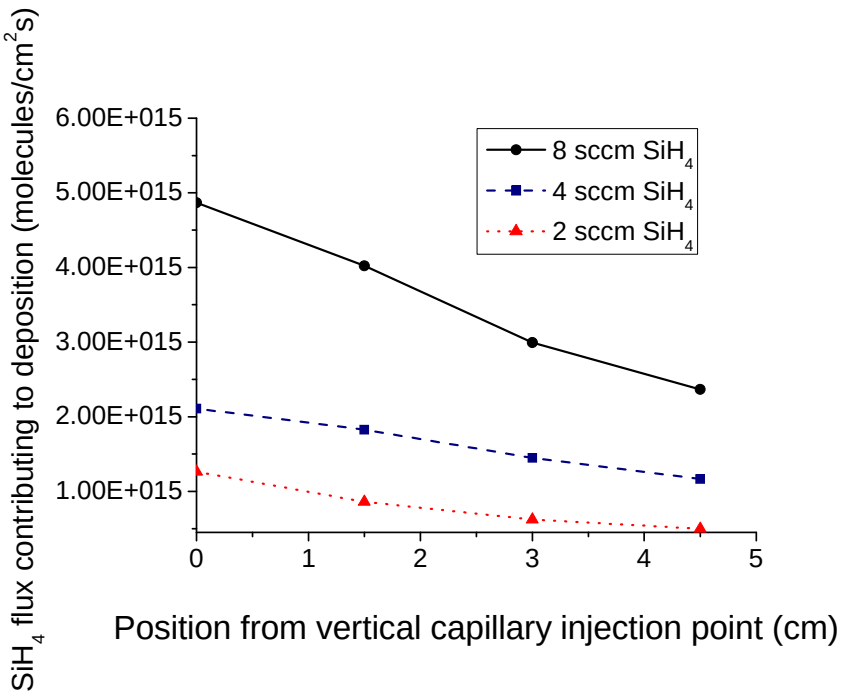

Figure IV-16. Experimental results of the flux of silicon atoms incorporated into the growing film, at different SiH_4 flow rates.

IV-5 Conclusion

In this Chapter, the high-density plasma system described in the preceding chapters is investigated using a DSMC model developed for this purpose. The Chapter starts with a brief overview of the DSMC method and an assessment of the factors that need to be taken into consideration when using it. The silane flow in the capillary jet used for injection of the precursor in the reactor was then studied numerically with a DSMC model. This model was modified to study the silane and oxygen precursor flux in the deposition chamber and was then extended to include the removal of two oxygen molecules and the creation of two water molecules when a silane molecule sticks to a surface.

Modeling results show the flux of water onto the substrate holder to be relatively uniform, confirming the claim made in section III-4 that a uniform flux of H_2O onto the substrate holder will lead to the same amount of H_2O incorporated into the growing film across the substrate and a consequent lower Si-OH content in the regions of higher deposition rate. Comparing the simulation results with experimental values of the fraction of silane molecules incorporated into the growing film per second, the silane reactive sticking coefficient is found to be between 0.01 and 0.03.

References

[1] G.A. Bird, *Molecular Gas Dynamics and the Direct Simulation of Gas Flows*, Clarendon Press, Oxford (1994).

[2] P.S. Prasanth, J.K. Kakkassery, J. Indian Inst. Sci., 86 (2006) 169.

[3] C.R. Kleijn, *Multi-scale computational modeling of fluid mechanics in thin film processing*, 5th GRACM int. congr. Comp. Mech., 29 June – 1 July, (2005).

[4] C.R. Kleijn, R. Dorsman, K.J. Kuijlaars, M. Okkerse, H. van Santen, J. Non-Cryst. Growth, 303 (2007) 362.

[5] E.S. Oran, C.K. Oh, B.Z. Cybyk, Annual Review of Fluid Mechanics, 30 (1998) 403.

[6] M. Reira, J.A. Rodríguez, J. Barreto, C. Domínguez, Thin Solid Films, 515 (2007) 3380.

[7] T. Kim, S-M. Suh, S.L. Girshick, M.R. Zachariah, P.H. McMurry, R.M. Rassel, Z. Shen, S.A. Campbell, J. Vac. Sci. Technol. A, 20 (2002) 413.

[8] S.-M. Suh, M.R. Zachariah, S.L. Girshick, J. Vac. Sci. Technol. A, 19 (2001) 940.

[9] S. Varoutis, D. Valougeorgis, O. Sazhin, F. Sharipov, J. Vac. Sci. Technol. A, 26 (2008) 228.

[10] L.A. Gochberg, R.L. Kinder, *Low Pressure Deposition in a High Density Plasma CVD reactor*, Novellus Systems, Inc., San Jose, California.

[11] D.J. Economou, Thin Solid Films, 365 (2000) 348.

[12] A.K. Rebrov, J. Vac. Sci. Technol. A, 19 (2001) 1679.

[13] D.B. Hash, T. Mihopoulos, T.R. Govindan, M. Meyyappen, J. Vac. Sci. Technol. B, 18 (2000) 2808.

[14] P.K. Shufflebotham, T.J. Bartel, B. Berney, J. Vac. Sci. Technol. B, 13 (1995) 1862.

[15] http://www.gab.com.au.

[16] T.C. Adamson, Jr. J.A. Nicholls, *On the structure of jets from highly underexpanded nozzles into still air*, Engineering research institute, University of Michigan Ann Arbor, Feb. (1958).

[17] A.A. Ivanov, Jr., C. Rouillé, M. Bacal, Y. Arnal, S. Béchu, J. Pelletier, Rev. Scientific Instr., 76 (2004) 1750.

Chapter V

Conclusion

V-1 *Summary of the results*

This thesis reports on the deposition of silicon dioxide, oxynitride and silicon nitride, with specific focus on the influence of the SiH_4 injection system, in a low-pressure, high-density MDECR-PECVD system. The precursor gases used were silane, oxygen and nitrogen with argon occasionally added as tracer gas. Depositions were done onto glass, crystalline silicon and PET substrates. Chapter I gave an overview of the state-of-the-art in HDP systems, with special emphasis placed on the MDECR-PECVD system used during this thesis. The various characterization techniques used were also briefly discussed. The influence of the magnetic field configuration on the uniformity of silica deposited onto a 200 mm wafer was studied. Applying an RF bias and using an optimized magnetic field configuration a uniformity better than 3.3 % across the 200 mm wafer diameter was obtained.

In Chapter II, the influence of the gas flow rates, reactor pressure, microwave power and radio frequency bias on the properties of the silica, silicon nitride and oxynitride films were investigated with FTIR and SE, while the plasma was characterized with OES and differentially pumped QMS. It was found that using a $SiH_4/(SiH_4+O_2)$ gas flow ratio of 0.25 and the gas ring injection system for the silane gas, silica films with optical properties comparable with those of thermal silica and with deposition rates of up to 2.1 nm/s could be deposited. This process parameter study was used for the deposition of optical filters and Bragg mirrors, as well as silicon dioxide and nitride water barrier coatings on PET.

The directional jet injection of the undiluted silane was investigated in Chapter III. Residual gas measurements using differentially pumped QMS were performed for the different injection systems. This showed the precursor's consumption in the reactor chamber to be similar when using the different injection systems. The amount of silane precursor consumed at the substrate level however increases when using a capillary jet instead of a gas ring. This could be seen by the deposition rate that increased to 3.5 nm/s when using the capillary jet injection system and similar gas flow rates as with the gas ring. The MDECR-PECVD system can thus not be considered as well mixed for gases with dissociation products that have high sticking coefficients. This conclusion is in contradiction with the currently accepted paradigm that considers low-pressure, high-density plasma systems to be well-mixed reactors. This work showed that the low pressure used in the MDECR-PECVD system prevented mixing of the gases and led to beamlike transport of the silicon precursors. The influence the different process parameters have on the hydroxyl content of the oxide films was studied using transmission measurements. Measurements were taken at various points across Infrasil fused quartz substrates in order to see the influence the distance from the injection point has on the thickness–normalized Si-OH concentration. It was found that there is a decrease in the silanol concentration in the areas of higher deposition rates. These results show that the primary silane flux onto the surface, which depends on the positioning of the injection point and the gas flow rate, plays an important role in determining both the deposition rate and the Si-OH content of the film. The correct positioning of the silane injection point is found to be vital for optimizing the quality of the films.

The Direct Simulation Monte Carlo method developed by G.A. Bird was used in Chapter IV to simulate the exit velocity of the silane molecules from the capillary tube into the vacuum chamber of the HDP system, as well as to simulate the flux of precursors and their utilization in the vacuum chamber and on the substrate surface. It was found that the flux of H_2O onto the substrate holder is uniform, while the SiH_4 flux varies considerably along the substrate surface. The SiH_4 reactive sticking coefficient was estimated by comparing the simulated amount of silicon atoms incorporated into the growing film for different reactive sticking coefficients with experimental values. This resulted in an estimate for the reactive sticking coefficient of between 0.01 and 0.03.

V-2 *Recommendations for future work*

The DSMC simulation presented in Chapter IV currently makes use of SIH_4 and O_2 precursors that create H_2O via a surface reaction. The simulation has the possibility to be improved by including the plasma physics and chemistry. As a first step, the atomic oxygen flux can be added (the O^*/O_2 ratio can be a free parameter or can be deduced from OES measurements). At a later stage the charged species in the plasma and the electromagnetic field can be taken into account. This last point is however a very complex problem that has not yet been resolved anywhere.

While the optical emission measurements used in this study were useful for identifying the different radicals in an oxide deposition plasma, measurements taken with a device that offers a higher resolution will be useful for characterizing the SiN_x and SiO_xN_y deposition plasmas.

Changing the configuration of the MDECR-PECVD system in a way that substrate is positioned “face-down” to reduce the flakes falling on the substrate during deposition and thus suppress the creation of pinholes and other particle-related growth defects in the films will improve the integrity of the dielectric and increase the breakdown voltage of both the SiO_2 and SiN_X films.

The experience gained during this work could be used to design an injection system that will ensure a high deposition rate over large surfaces while minimizing OH incorporation. This will however require a full 3D implementation of the model.

V-3 *List of publications*

- R. Botha, P. Bulkin, P. Swart, *Deposition of Ge-doped silica thin films for an integrated optic application using a matrix distributed electron cyclotron resonance PECVD reactor*, Optical Materials, 30 (2007) 244.

- R. Botha, B. Haj Ibrahim, P. Bulkin, B. Drévillon, *Deposition of dielectrics using a matrix distributed electron cyclotron resonance plasma enhanced chemical vapor deposition system*, Thin Solid Films, 515 (2007) 7594.
- R. Botha, B. Haj Ibrahim, P. Bulkin, B. Drévillon, *Silane injection in a high-density low-pressure plasma system and its influence on the deposition kinetics and material properties of SiO_2*, Journal of Vacuum Science & Technology A, 26 (2008) 1115.
- B. Haj Ibrahim, R. Botha, J.E. Bourée, P. Bulkin, B. Drévillon, *Correlation of side-lobe suppression between rugate filters and multilayer mirrors*, Applied Optics, 46 (2007) 7776.
- B. Haj Ibrahim, R. Botha, P.Bulkin, B. Drévillon, *Multilayer optical filters control by multi-channel kinetic ellipsometry*, Physica Status Solidi C, 5 (2008) 1290.
- R. Botha, T. Novikova, P. Bulkin, *Capillary jet injection of SiH_4 in the HDP CVD of SiO_2, submitted to the Journal of Vacuum Science & Technology A* (October 2008).

V-4 *List of attended conferences and workshops*

- American Vacuum Society, Boston, United States. Oral presented: *Capillary Jet Injection of SiH_4 in the HDP-PECVD of SiO_2*, 19 – 24 October 2008.

- Technological Plasma Workshop, Belfast, Ireland. Poster presented: *Study of SiO_2 Deposition in a HDP-PECVD System using a Free Jet Experiment and a DSMC Simulation*, December 2007.
- CIP 2007 Short courses, *16th International Colloquium on Plasma Processes*, Toulouse, France, June 2007.
- EMRS spring meeting, Strasburg, France. Oral presented: *High-density low-pressure plasmas for coatings deposition,* May 2007.
- 2nd FlexiDis Traning Workshop, King's College Cambridge, UK, March 2007.
- 5éme Journées plasma froids, Bonascre, France, October 2006.
- *European summer school on Low Temperature Plasma Physics*, Bad Honnef, Germany, October 2006.
- EMRS spring meeting, Nice, France. Poster presented: *Deposition of dielectrics using a matrix distributed electron cyclotron resonance plasma enhanced chemical vapour deposition system,* May 2006.

Bibliography

A

F. Abelès, Annales de Physique 5 (1950) 596 (706).

T.C. Adamson, Jr. J.A. Nicholls, *On the structure of jets from highly underexpanded nozzles into still air*, Engineering research institute, University of Michigan Ann Arbor, Feb. (1958).

B. Aguis, M.C. Hugon, N. Jiang, F. Varniere, F. Plais, D. Pribat, M. Froment, M. Puech, *Floating temperature deposition of device quality SiO2 thin films by DECR plasma*, Mat. Res. Soc. Symp. Proc., 284 (1993) 181.

R.G. Andosca, W.J. Varhue, E. Adams, *Silicon dioxide films deposited by electron cyclotron resonance plasma enhanced chemical vapor deposition*, J. Appl. Phys., 72 (1992) 1126.

K. Aumaille, A. Granier, M. Schmidt, B. Grolleau, C. Vallée, *Study of oxygen/tetraethoxysilane plasmas in a helicon reactor using optical emission spectroscopy and mass spectrometry*, Plasma Sources Sci. Technol., 9 (2000) 331.

K. Aumaille, A. Granier, M. Schmidt, B. Grolleau, C. Vallée, G. Turban, *Study of oxygen/tetraethoxysilane plasmas in a helicon reactor using optical emission spectroscopy and mass spectrometry*, Plasma Sources Sci. Technol. A, 9 (2000) 331.

F. Ay, A. Aydinli, *Comparative investigation of hydrogen bonding in silicon based PECVD grown dielectrics for optical waveguides*, Optical Materials, 26 (2004) 33.

R. Azzam, N. Bashara, *Ellipsometry and polarized light*, North Holland Personal Library (1970).

B

A. Banerjee, T. DebRoy, *Optical emission investigation of the plasma enhanced chemical vapor deposition of silicon oxide films*, J. Vac. Sci. Technol. A, 10 (1992) 3395.

G. Bekefi, *Principles of laser plasmas*, John Wiley & sons, New York (1976) 592.

J. Benedikt, A. von Keudell, *Surface processes in plasmas*, European summer school of Low Temperature Plasma Physics, Bad Honnef, Germany (2006).

Bieder, A. Gruniger, Ph. Rudolf von Rohr, *Deposition of SiO_x diffusion barriers flexible packaging materials by PECVD*, Surf. Coat. Technol., 200 (2005) 928.

G.A. Bird, *Molecular Gas Dynamics and the Direct Simulation of Gas Flows*, Clarendon Press, Oxford (1994).

A. Bogaerts, E. Neyts, R. Gijbels, J. van der Mullen, *Gas discharge plasmas and their applications*, Spectrochimica Acta Part B 57 (2002) 609.

R. Botha, B. haj Ibrahim, P. Bulkin, B. Drévillon, *Deposition of dielectrics using a matrix distributed electron cyclotron resonance plasma enhanced chemical vapor deposition system*, Thin Solid Films, 515 (2007) 7594.

R. Botha, B. Haj Ibrahim, P. Bulkin, B. Drévillon, *Silane injection in a high-density low-pressure plasma system and its influence on the deposition kinetics and material properties of SiO_2*, J. Vac. Sci. Technol. A, 26 (2008) 1115.

N. St J. Braithwaithe, *Introduction to gas discharges*, Plasma Sourc. Sci. Technol., 9 (2000) 517.

D.A.G. Bruggeman, *Berechnung verschiedener ohysikalischer Konstanten von heterogenen Substanzen. I. Dielectrizitatkonstanten und Leitfahigkeiten der Mischkorper aus isotropen Substanzen*, Ann. Physik, Leipzig, Germany, 24 (1935) 636.

E.S. Bulat, G. Ditmer, C. Herrick, S. Hankin, *Characterization of biased electron cyclotron resonance deposited oxides*, J. Vac. Sci. Technol. A, 10 (1992) 1402.

P. Bulkin, N. Bertrand, B. Drévillon, *Deposition of SiO_2 in integrated distributed electron cyclotron resonance microwave reactor*, Thin Solid Films, 296 (1997) 66.

P. Bulkin, A. Hofrichter, T. Heitz, J. Huc, B. Drévillon, J. J. Benattar, *Deposition of silicon alloys in an integrated distributed electron cyclotron resonance reactor: Oxide, nitride, oxinitrides, and multilayer structures*, J. Vac. Sci. Technol. A, 20 (2002) 338.

P. V. Bulkin P.L. Swart, B.M. Lacquet, *Effect of process parameters on the properties of electron cyclotron resonance plasma deposited silicon-oxynitride*, J. Non-cryst. solids, 187 (1995) 403.

P. Bulkin, P. Swart, B. Lacquet, *Electron cyclotron resonance plasma enhanced chemical vapour deposition and optical properties of SiO thin films*, J. Non-Cryst. Solids, 226 (1998) 58.

P. Bulkin, P. Swart, B. Lacquet, *Electron cyclotron resonance plasma deposition of SiN_x for optical applications*, Thin Solid Films, 241 (1994) 247.

C

M. Calafat, D. Escaich, R. Clergereaux, P. Raynaud, Y. Segui, *Particle formation in acetylene very low-pressure high density magnetized plasmas*, Applied Physics Letters, 91 (2007) 181502.

A. Canillas, A. Pinyol, J. Sancho-Parramon, J. Ferré-Borrull, E. Bertran, *FTIR phase-modulated ellipsometry characterization of hydrogenated amorphous silicon nitride thin films with embedded nanoparticles*, Thin Solid Films, 455 (2004) 167.

D.A. Carl, D.W. Hess, M.A. Lieberman, *Kinetics of photoresist etching in an electron cyclotron resonance plasma*, J. Appl. Phys., 68 (1990) 1859.

P. Chabert, *Physique des plasmas froids: Plasmas radiofréquence*, Ecole polytechnique, France (2007).

C. Charles, *Effects of cross field diffusion in a low pressure high density oxygen/silane plasma*, J. Vac. Sci. Technol. A, 20 (2002) 1275.

C. Charles, *Wall effects on the chemistry in a pulsed oxygen/silane radiofrequency helicon plasma*, J. Phys. D: Appl. Phys, 36 (2003) 1.

C. Charles, R.W. Boswell, *Stress reduction in silicon dioxide layers by pulsing an oxygen/silane helicon diffusion plasma*, J. Appl. Phys., 84 (1998) 350.

C. Charles, R.W. Boswell, H. Kuwahara, *SiO_2 deposition from oxygen/silane pulsed helicon diffusion plasmas*, Appl. Phys. Lett., 67 (1995) 40.

C. Charles, G. Giroult-Matlakowski, R.W. Boswell, A. Goullet, G. Turban, C. Cardinaud, *Characterization of silicon dioxide films deposited at low pressure and temperature in a helicon diffusion reactor*, J. Vac. Sci. Technol. A, 11 (1993) 2954.

T.T. Chau, K.C. Kao, *Optical emission spectra of microwave oxygen plasmas and fabrication of SiO_2 films*, J. Vac. Sci. Technol. B, 14 (1996) 527.

F.F. Chen, *Industrial applications of low temperature plasma physics*, Physics of plasmas, 2 (1995) 2164.

F.F. Chen, J.P. Chang, *Lecture notes on principles of plasma processing*, Springer, Los Angelos (2003).

H. Conrads, M. Schmidt, *Plasma generation and plasma sources*, Plasma Sci. Technol., 9 (2000) 44.

D.R. Cote, S.V. Nguyen, A.K. Stamper, D.S. Armbrust, D. Többen, R.A. Conti, G.Y. Lee, *Plasma-assisted chemical vapor deposition of dielectric thin films for ULSI semiconductor circuits*, IBM J. Res. Develop., 43(1/2) (1999).

J.N. Cox, *Fourier Transform Infrared Spectroscopy, Section 8.1 in Encyclopaedia of materials characterization*, Edited by C.R. Brundle, C.A. Evans Jr., S. Wilson, Butterworth-Heinemann, Stoneham MA (1992).

D

D. Daineka, P. Bulkin, G. Girard, J.-E. Bourrée, B. Drévillon, *High density plasma enhanced chemical vapor deposition of optical thin films*, Eur. Phys. J. Appl. Phys., 26 (2004) 3.

D. Daineka, P. Bulkin, G. Girard, B. Drévillon, *Simple method of gas flow ratio optimization in high rate deposition of SiO_2 by electron cyclotron resonance plasma enhanced chemical vapor deposition*, J. Vac. Sci. Technol. A, 22 (2004) 36.

P.H. Dawson, *Quadrupole mass spectrometry and its applications*, American Institute of Physics, New York, (1997).

M. Deilmann, H. Halfmann, N. Bibinov, P. Awakowicz, *Pulsed microwave plasma polymerization of silicon oxide films: application of efficient permeation barriers on polyethylene terephthalate*, Surf. Coat. Technol., 202 (2008) 1911.

A. del Prado, E. San Andrés, F.L. Martinez, I. Martil, G. Gonzalez-Diaz, W. Bohne, J. Röhring, B. Selle, M. Fernandez, *Composition and optical properties of silicon oxynitride films deposited by electron cyclotron resonance*, Vacuum, 67 (2002) 507.

S.C. Deshmuck, E.S. Aydil, *Low-temperature Plasma Enhanced Chemical Vapor Deposition of SiO_2*, Appl. Phys. Letters, 65 (1994) 3185.

J.A. Dobrowolski, *Optical properties of films and coatings, in Handbook of Optics, Vol. I*, Edited by M. Bass, E. W. van Stryland, D. R. Williams, and W. L. Wolfe, McGraw-Hill, New York (1995).

S. Dreer, P. Wilhartitz, *Critical evaluation of the state of the art of the analysis of light elements in thin films demonstrated using the examples of SiO_XN_Y and AlO_XN_Y films*, Pure and Applied Chemistry, 76 (2004) 1161.

B. Drévillon, *Phase modulated ellipsometry from the ultraviolet to the infrared: In situ application to the growth of semiconductors*, Prog. Crystal Growth Char. Mat., 27 (1993) 1.

E

D.J. Economou, *Modeling and simulation of plasma etching reactors for microelectronics*, Thin Solid Films, 365 (2000) 348.

F

U. Fantz, *Basics of plasma spectroscopy*, Pl Sources Sci & Technol, 15 (2006) 137.

A.J. Flewitt, A.P. Dyson, J. Robertson, W.I. Milne, *Low temperature growth of silicon nitride by electron cyclotron resonance plasma enhanced chemical vapour deposition*, Thin Solid Films, 383 (2001) 172.

M.H. Francombe, Ed., *Handbook of Thin Film Devices Volume 1: Heterostructures for High Performance Devices*, Academic Press, San Diego, CA, (2000).

J. Foggiato, *Chemical Vapor Deposition of Silicon Dioxide Films, Chapter 3 of the Handbook of thin film deposition techniques: principles, methods, equipment and applications, second edition*, edited by Krishna Seshan, William Andrew Inc., Austin (2002).

G

L.A. Gochberg, R.L. Kinder, *Low Pressure Deposition in a High Density Plasma CVD reactor*, Rarefied Gas Dynamics: 25th International Symposium, ed. M.S. Ivanov and A.K. Rebrov, Novosibirsk (2007) 1029.

D. Goghero, A. Goullet, G. Borvon, G. Turban, *Effect of the ion bombardment energy on silicon dioxide films deposited from oxygen/tetraethoxysilane plasmas in a helicon reactor*, Thin Solid Films, 471 (2005) 123.

D. Goghero, A. Goullet, J.P. Landesman, *Structural and electrical properties of SiO_2 films deposited on Si substrates from tetraethoxysilane/oxygen plasma*, Solid-state Electr. 49 (2005) 369.

A. Goullet, C. Vallée, A. Granier, G. Turban, *Optical spectroscopic analyses of OH incorporation into SiO_2 films deposited from O_2/tetraethoxysilane plasmas*, J. Vac. Sci. Technol. A, 18 (2000) 2452.

A. Granier, *Deposition of thin films by PECVD*, CIP'2007 Short courses, 16th international colloquium on plasma processes, Toulouse, France (2007).

A. Granier, F. Nicolazo, C. Vallée, A. Goullet, G. Turban, B. Grolleau, *Diagnostics in O_2 heilcon plasmas for SiO_2 deposition*, Plasma Sources Sci. Technol., 6 (1997) 147.

A. Granier, M. Vervloet, K. Aumaille, C. Vallée, *Optical emission spectra of TEOS and HMDSO derived plasmas used for thin film deposition*, Plasma Sources Sci. Technol., 12 (2003) 89.

D. Graves, *Plasma Processing*, IEEE Transactions on Plasma Science, 22 (1994) 31.

A. Gupta, G.N. Parsons, *Bond strain, chemical induction and OH incorporation in low temperature(350° – 100°C) plasma deposited silicon dioxide films*, J. Vac. Sci. Technol. B, 18 (2000) 1764.

H

B. Haj Ibrahim, R. Botha, J.-E. Bourée, P. Bulkin, B. Drevillon, *Correlation of side-lobe suppression between rugate filters and multilayer mirrors*, Applied Optics, 46 (2007) 7776.

B. Haj Ibrahim, R. Botha, P.Bulkin, B. Drévillon, *Multilayer optical filters control by multi-channel kinetic ellipsometry*, Physica Status Solidi C, 5 (2008) 1290.

B. Haj Ibrahim, P. Bulkin, D. Daineka, B. Drévillon, *Optical thin films deposition by MDECR-PECVD*, Proc. SPIE, 5963 (2005) 500.

S.M. Han, E.S. Aydil, *Study of surface reactions during plasma enhanced chemical vapor deposition of SiO_2 from SiH_4, O_2 and Ar plasma*, J. Vac. Sci. Technol. A, 14 (1996) 2062.

S.M. Han, E.S. Aydil, *Silanol concentration depth profiling during plasma deposition of SiO_2 using multiple internal reflection infrared spectroscopy*, J. Electrochem. Soc., 144 (1997) 3963.

S.M. Han, E.S. Aydil, *Plasma and surface diagnostics during plasma-enhanced chemical vapor deposition of SiO_2 from $SiH_4/O_2/Ar$ discharges*, Thin Solid Films, 290-291 (1996) 427.

D.B. Hash, T. Mihopoulos, T.R. Govindan, M. Meyyappen, *Characterization of showerhead performance at low pressure*, J. Vac. Sci. Technol. B, 18 (2000) 2808.

E. Hecht, *Optics, Fourth Edition, Chapter 3*, Addison-Wesley, San Francisco (2002).

T.V. Herak T.T. Chau, D.J. Thomson, S.R. Mejia, D.A. Buchanan, K.C. Kao, *Low-temp deposition of silicon dioxide films from electron cyclotron resonant microwave plasmas*, J. Appl. Phys., 65 (1989) 2457.

M.J. Hernandez, J. Garrido, J. Martinez, J. Piqueras, *Compositional and electrical properties of ECR-CVD silicon oxynitrides*, Semicond. Sci. Technol., 12 (1997) 927.

S. Hiyama, T. Ono, S. Lizuka, N. Sato, *Wide-area uniform plasma processing in an ECR plasma*, Plasma Sources Sci. Technol., 5 (1996) 299.

D.G. Howells, B.M. Henry, Y. Leterrier, J._A.E. Manson, J. Madocks, H.E. Assender, *Mechanical properties of SiO_x gas barrier coatings on polyester films*, Surf. Coat. Technol., 202 (2008) 3529.

D.G. Howells, B.M. Henry, J. Madocks, H.E. Assender, *High quality plasma enhanced chemical vapour deposited silicon oxide gas barrier coatings on polyester films*, Thin Solid Films, 516 (2008) 3081.

O. Humbach, H. Fabian, U. Grzesik, U. Haken, W. Heitmann, *Analysis of OH absorption bands in synthetic silica*, J. Non-Cryst. Solids, 203 (1996) 19.

I

G.I. Isai, J. Holleman, H. Wallinga, P.H. Woerlee, *Low hydrogen content silicon nitride films deposited at room temperature with an ECR plasma source*, J. Electrochem. Soc., 151 (2004) C649.

A.A. Ivanov, Jr., C. Rouillé, M. Bacal, Y. Arnal, S. Béchu, J. Pelletier, *H- ion production in electron cyclotron resonance driven multicusp volume source*, Rev. Scientific Instr., 76 (2004) 1750.

J

S.N. Jasperson, D.K. Burge, R.C. O'Handley, *A modulated ellipsometer for studying thin film optical properties and surface dynamics*, Surface Science, 27 (1973) 548.

G.E. Jellison Jr., F.A. Modine, *Parameterization of the optical functions of amorphous materials in the interband region*, Appl. Phys. Lett., 69 (1996) 371 (Errata 69 (1996) 2137).

G.E. Jellison Jr., V.I. Merkulov, A.A. Puretzky, D.B. Geohegan, G. Eras, D.H. Lowndes, J.B. Caughman, *Characterization of thin-film amorphous semiconductors using spectroscopic ellipsometry*, Thin Solid Films, 377 – 378 (2000) 68.

F.A. Jenkins, H.E. White, *Fundamentals of Optics*, McGraw-Hill, Auckland (1981) 482.

N. Jiang, B. Aguis, M.C. Hugon, J. Olivier, M. Puech, *Radio frequency bias effects on SiO_2 films deposited by distributed electron cyclotron resonance plasma enhanced chemical vapor deposition*, J. Appl. Physics, 76 (1994) 1847.

N. Jiang, M.-C. Hugon, B. Aguis, T. Kretz, F. Plais, D. Pribat, T. Carriere, M. Puech, *Device quality SiO_2 deposited by distributed electron cyclotron resonance plasma enhanced chemical vapor deposition without substrate heating*, Jpn. J. Appl. Phys., 31 (1992) L1404.

J. Jolly, *Spectrométrie de masse des plasmas réactifs*, DEA Physique des Plasmas (2003).

K

P. Kae-Nune, J. Perrin, J. Guillon, J. Jolly, *Mass spectrometry detection of radicals in SiH_4–CH_4–H_2 glow discharge plasmas*, Plasma Sources Sci. Technol., 4 (1995) 250.

T. Kim, S.-M. Suh, S.L. Girshick, M.R. Zachariah, P.H. McMurry, R.M. Rassel, Z. Shen, S.A. Campbell, *Particle formation during low-pressure chemical vapor deposition from silane and oxygen: Measurement, modeling and film properties*, J. Vac. Sci. Technol. A, 20 (2002) 413.

N. Kitamura,a K. Fukumi, and J. Nishii, N. Ohno, *Relationship between refractive index and density of synthetic silica glasses*, J. Appl. Phys., 101 (2007) 123533-1.

C.R. Kleijn, *Multi-scale computational modeling of fluid mechanics in thin film processing*, 5th GRACM int. congr. Comp. Mech., 29 June – 1 July, (2005).

C.R. Kleijn, R. Dorsman, K.J. Kuijlaars, M. Okkerse, H. van Santen, *Multi-scale modeling of chemical vapor deposition processes for thin film technology*, J. Non-Cryst. Growth, 303 (2007) 362.

A.Y. Kovalgin, A. Boogaard, I. Brunets, J. Holleman, J. Schmitz, *Chemical modeling of a high-density inductively-coupled plasma reactor containing silane*, Surf. Coat. Technol., 201 (2007) 8849.

A.Y. Kovalgin, G. Isai, J. Holleman, J. Schmitz, *Low-Temperature SiO_2 Layers Deposited by Combination of ECR Plasma and Supersonic Silane/Helium Jet*, J. Electrochem. Soc., 155 (2008) G21.

L

A. Lacoste, T. Lagarde, S. Béchu, Y. Arnal, J Pelletier, *Multi-dipolar plasmas for uniform processing: physics, design and performance,* Plasma Sources Sci. Technol., 11 (2002) 407.

W.A. Lanford, M.J. Rand, *The hydrogen content of plasma-deposited silicon nitride*, J. Appl. Phys., 49 (1978) 2473.

S.E. Lassig, J.D. Tucker, *Intermetal dielectric deposition by electron cyclotron resonance chemical vapor deposition (ECR CVD)*, Microelectr. J., 26 (1995) xi.

Leybold Vacuum, *Mass spectrometry: Products and reference book*, (2001/2002).

M.A. Lieberman and R.A. Gottscho, *Design of High-Density Plasma Sources for Materials Processing: advances in research and development: plasma sources for thin film deposition and etching,* Physics of Thin Films, edited by M. Francombe and J. Vossen, Academic Press, New York, 18 (1994) 1.

M.A. Lieberman, A.J. Lichtenberg, *Principles of Plasma Discharges and Materials Processing second edition*, John Wiley & Sons Inc., Hoboken, New Jersey (2005).

G. Lucovsky, P.D. Richard, D.V. Tsu, S.Y. Lin, R.J. Markunas, *Deposition of silicon dioxide and silicon nitride by remote plasma enhanced chemical vapor deposition*, J. Vac. Sci. Technol. A, 4 (1986) 681.

G. Lucovsky, D.V. Tsu, *Plasma enhanced chemical vapor deposition: Differences between direct and remote plasma excitation*, J. Vac. Sci. Technol. A, 5 (1987) 2231.

M

T.P. Ma, *Making silicon Nitride Film a Viable Gate Dielectric*, IEEE Transactions on Electron Devices, 45 (1998) 680.

W.A. MacDonald, *Engineered films for display technologies*, J. Mater. Chem., 14 (2004) 4.

L. Martinu, D. Poitras, *Plasma deposition of optical films and coatings: A review*, J. Vac. Sci. Technol. A, 18 (2000) 2619.

P. Masini, M. Bernasconi, *Ab initio simulations of hydroxylation and dehydroxylation reactions at surfaces: amorphous silica and brucite*, J. Phys.: Condens. Matter, 14 (2002) 4133.

S. Matsuo, M. Kiuchi, *Low Temperature Chemical Vapor Deposition Method Utilizing an Electron Cyclotron Resonance Plasma*, Jpn. J. Appl. Phys. 22 (1983) L210.

Don Mattox, *handbook of physical vapor deposition processing*, Willam Andrew Applied Science Publishers, Austin (1998).

E. Meeks, R.S. Larson, P. Ho, C. Apblett, S.M. Han E. Edelberg, E.S. Aydil, *Modeling of SiO_2 deposition in high density plasma reactors and comparisons*

of model predictions with experimental measurements, J. Vac. Sci. Technol. A, 16 (1998) 544.

S.A. Moshkalyov, J.A. Diniz, J.W. Swart, P.J. Tatsch, M. Machida, *Deposition of silicon nitride by low-pressure electron cyclotron resonance plasma enhanced chemical vapor deposition in N_2/Ar/SiH_4*, J. Vac. Sci. Technol. B, 15 (1997) 2682.

N

S.V. Nguyen, *High-density plasma chemical vapor deposition of silicon-based dielectric films for integrated circuits*, IBM J. Res. Develop., 43 (1999) 109.

O

M. Ohring, *Materials science of thin films: Deposition and structure*, Academic Press, San Diego (2002).

M. Ohring, *Materials science of thin films: Deposition and structure, second edition*, Elsevier Academic Press, Hoboken, New Jersey (2002).

Onix systems Inc., *VGQ operations manual* (1998).

E.S. Oran, C.K. Oh, B.Z. Cybyk, *Direct Simulation Monte Carlo: Recent Advance and Applications*, Ann. Rev. Fluid Mech., 30 (1998) 403.

M. Orfert, K. Richter, *Plasma enhanced chemical vapor deposition of SiN-films for passivation of three-dimensional substrates*, Surf. Coat. Technol., 116-119 (1999) 622.

P

T.C. Paulick, *Guidelines for construction of low-pressure gas manifolds*, J. Vac. Sci. Technol. A, 21 (1982) 1032.

J. Pelletier, Y. Arnal, O. Joubert, *Etching mechanisms of polymers in oxygen microwave multipolar plasmas*, Appl. Phys. Lett., 53 (1988) 1914.

S. T. Picraux, E. Chason, T. M. Mayer, *Ion-assisted surface processing of electronic materials*, MRS Bulletin, XVII (June, 1992) 52.

F. Plais, B. Aguis, F. Abel, J. Siejka, Puech, G. Ravel, P. Alnot, N. Proust, *Low Temperature Deposition of SiO_2 by Distributed Electron Cyclotron Resonance Plasma-Enhanced Chemical Vapor Deposition*, J. Electrochem. Soc., 139 (1992) 1492.

W.A. Pliskin, *Comparison of properties of dielectric films deposited by various methods*, J. Vac. Sci. Technol. A, 5 (1977) 1064.

D. Poelman, P.F. Smet, *Methods for the determination of the optical constants of thin films from single transmission measurements: a critical review*, J. Phys. D: Appl. Phys., 36 (2003) 1850.

P.S. Prasanth, J.K. Kakkassery, *Direct simulation Monte Carlo (DSMC): A numerical method for transition-regime flows – A review*, J. Indian Inst. Sci., 86 (2006) 169.

R

A.K. Rebrov, *Free jets in vacuum technologies*, J. Vac. Sci. Technol. A, 19 (2001) 1679.

M. Reira, J.A. Rodríguez, J. Barreto, C. Domínguez, *Modeling of non-stoichiometric silicon oxides obtained by plasma enhanced chemical vapour deposition process*, Thin Solid Films, 515 (2007) 3380.

J.R. Roberts, *Optical emission spectroscopy on the Gaseous Reference Cell*, J. Res. Nat. Inst. Std & Technol., 100 (1995) 353.

R. Robertson, D. Hils, H. Chatham, A. Gallagher, *Radical species in argon-silane discharges*, Appl. Phys. Lett., 43 (1983) 544.

P. Roca i Cabarrocas, P. Bulkin, D. Daineka, T.H. Dao, P. Leempoel, P. Descamps, T. Kervyn de Meerendré, J. Charliac, *Advances in the deposition of microcrystalline silicon at high rate by distributed electron cyclotron resonance*, Thin Solid Films, 516 (2008) 6834.

S. Rojas, A. Modelli, W.S. Wu, A. Borghesi, B. Pivac, *Properties of silicon dioxide films prepared by low-pressure chemical vapor deposition from tetraethylorthosilicate*, J. Vac. Sci. Technol. B, 8 (1990) 1177.

H. M. Rosenstock, K. Draxl, B. W. Steiner, J. T. Herron, *Energetics of Gaseous Ions*, J. Phys. Chem. Ref. Data, Suppl. 1, 6 (1977) 1.

T. Roschuk, J. Wojcik, X. Tan, J.A. Davies, P. Mascher, *Optical and compositional characterization of SiO_xN_y and SiO_x thin films deposited by electron cyclotron resonance plasma enhanced chemical vapor deposition*, J. Vac. Sci. Technol. A, 22 (2004) 883.

A. Rousseau, *Discharge physics: Energy deposition, reactivity*, CIP'2007 Short courses, 16th international colloquium on plasma processes, Toulouse, France (2007).

S

B.S. Sahu, O.P. Agnihotri, S.C. Jain, R. Mertens, I. Kato, *Influence of hydrogen on losses in silicon oxynitride planar optical waveguides*, Semicond. Sci. Technol., 15 (2000) L11.

K. L. Seaward, J.E. Turner, K. Nauka, A.M.E. Nel, *Role of ions in electron cyclotron resonance plasma-enhanced chemical vapor deposition of silicon dioxide*, J. Vac. Sci. Technol. B, 13 (1995) 118.

T. Schmauder, K.-D. Nauenburg, K. Kruse, G. Ickes, *Hard coatings by plasma CVD on polycarbonate for automotive and optical applications*, Thin Solid Films, 502 (2006) 270.

P.K. Shufflebotham, T.J. Bartel, B. Berney, *Experimental validation of a direct simulation by Monte Carlo molecular gas flow model*, J. Vac. Sci. Technol. B, 13 (1995) 1862.

S.P. Shufflebotham, M. Weise, D. Pirkle, D. Denison, *Biased Electron Cyclotron Resonance Chemical-Vapor Deposition of Silicon Dioxide Inter-Metal Dielectric Thin Films*, Materials Sci. Forum, 140-142 (1993) 255.

W. Stoffels, *Plasma diagnostics: Absorption and mass spectrometry, European summer school on Low Temperature Plasma Physics*, Bad Honnef, Germany (October 2006).

S.-M. Suh, .R. Zachariah, S.L. Girshick, *Modeling particle formation during low-pressure silane oxidation: Detailed chemical kintetics and aerosol dynamics*, J. Vac. Sci. Technol. A, 19 (2001) 940.

T

M. Tadokoro, A. Itoh, N. Nakano, Z. Lj. Petrovic, T. Makabe, *Diagnostics of an inductively coupled plasma in oxygen*, IEEE Trans. Plasma Sci., 26 (1998) 1724.

K. Takechi, S. Otsuki, *Simulations for the Effect of Chamber Geometry on Oxygen Plasma Characteristics for Very Large Plasma Sources*, IEEE Trans. Semicond. Man., 19 (2006) 286.

J. Tauc, *Optical Properties of Solids*, p. 123, Plenum, New York (1969).

J.A. Theil, *Gas distribution through injection manifolds in vacuum systems*, J. Vac. Sci. Technol. A, 13 (1995) 442.

J.C. Thomaz, J. Amorim, C.F. Souza, *Validity of actinometry to measure N and H atom concentration in N_2-H_2 direct current glow discharges*, J. Phys. D: Appl. Phys., 32 (1999) 3208.

Towne Technologies, Inc., http://townetech.com/shipley.htm

U

J. Ubrig, S. Martin, S. Cros, J.-E. Bourée, *Interface phenomena in multilayers deposited by PECVD for encapsulation of lithium microbatteries*, J. Physics : Conf. Series, 100 (2008) 082030.

V

S. Varoutis, D. Valougeorgis, O. Sazhin, F. Sharipov, *Rarefied gas flow through short tubes into vacuum*, J. Vac. Sci. Technol. A, 26 (2008) 228.

W

A. Wiersch, C. Heedt, S. Schneiders, R. Tilders, F. Buchali, W. Kuebart, W. Prost, F.J. Tegude, *Room-temperature deposition of SiN_x using ECR-PECVD for III/V semiconductor microelectronics in lift-off technique*, J. Non-Cryst. Solids, 187 (1995) 334.

K.M. Welch, *Sticking coefficients*, Vac. Technol. Coat. (2006) 26.

Y

S.F. Yoon, K.H. Tan, Q. Zhang, M. Rusli, J. Ahn, L. Valeri, *Effect of microwave power on the electron energy in an electron cyclotron resonance plasma*, Vacuum, 61 (2001) 29.

Appendix A

Dispersion models

A-1 The Lorentz Classical Oscillator Model

The classical Lorentz oscillator[1,2] is a widely used approximation for the modeling of the wavelength-dependent complex refractive index of amorphous materials in spectroscopic ellipsometry. It can be described by the following two equations[3]:

$$n^2 - k^2 = 1 + \frac{A\lambda^2}{\lambda^2 - {\lambda_0}^2 + g\lambda^2/(\lambda^2 - {\lambda_0}^2)}$$

$$2nk = \frac{A\sqrt{g}\lambda^3}{(\lambda^2 - {\lambda_0}^2)^2 + g\lambda^2} \qquad \textit{(A-1)}$$

λ_0 is the oscillator central wavelength, g the damping factor, A the oscillator strength and n,k the the refractive index real and complex parts. This set of coupled equations for n and k is consistent with the Kramers-Kronig relations*.

The right hand side of the first equation is the dielectric function at infinite energy (zero wavelength).A fitting parameter ε_∞ is usually used in its place to represent the dielectric function at smaller wavelengths than measured. The classical Lorentz oscillator model looks as follows in the Delta-Psi software that was used to fit the spectroscopic ellipsometry data:

$$\varepsilon = \varepsilon_\infty + \frac{(\varepsilon_s - \varepsilon_\infty){\omega_t}^2}{{\omega_t}^2 - \omega^2 + i\Gamma_0\omega} + \frac{{\omega_p}^2}{-\omega^2 + i\Gamma_D\omega} + \sum_{j=1}^{2}\frac{f_j\omega_{0j}^2}{\omega_{0j}^2 - \omega^2 + i\gamma_j\omega} \qquad \textit{(A-2)}$$

* The Kramers-Kronig relations relate the real part of an analytical complex function to an integral containing the imaginary part of the function, and vice versa.

A-2 The Tauc-Lorentz Model

Jellison et al.[4] implemented the Tauc-Lorentz model in ellipsometry. As with the Lorentz oscillator model, it is Kramers-Kronig consistent [5]. The Tauc expression for the imaginary part of the dielectric function near the band edge, is given by [6]:

$$\varepsilon_2(E) = A_T \frac{(E - E_g)^2}{E^2} \Theta(E - E_g) \qquad \textit{(A-3)}$$

Here E_g represents the band gap of the material and Θ the Heaviside function, with $\Theta(E<0) = 0$ and $\Theta(E \geq 0) = 1$. We can obtain the Tauc-Lorentz expression for the imaginary part of the complex dielectric function by multiplying this function with the complex dielectric function for a Lorentz oscillator:

$$\varepsilon_2(E) = \frac{aE_0\Gamma(E - E_g)^2}{E[(E^2 - {E_0}^2)^2 + \Gamma^2 E^2]} \Theta(E - E_g) \qquad \textit{(A-4)}$$

E_0 is the peak in the joint density of states, Γ the broadening parameter and a the pre-factor. Performing Kramers-Kronig integration on the above equation, the Tauc-Lorentz dielectric function's real part can be obtained:

$$\varepsilon_1(E) = \varepsilon 1(x) + \frac{2}{\pi} P_{E_g}^{x} \frac{\xi \varepsilon_2(E)}{\xi^2 - E^2} d\xi \qquad \textit{(A-5)}$$

Here, P is the Cauchy principle part of the integral and $\varepsilon_1(\infty) = 1$.

References

[1] F.A. Jenkins, H.E. White, *Fundamentals of Optics*, McGraw-Hill, Auckland (1981) 482.

[2] E. Hecht, *Optics*, Fourth Edition, *Chapter 3*, Addison-Wesley, San Francisco (2002).

[3] D. Poelman, P.F. Smet, J. Phys. D: Appl. Phys., 36 (2003) 1850.

[4] G.E. Jellison Jr., F.A. Modine, Appl. Phys. Lett., 69 (1996) 371 (Errata 69 (1996) 2137).

[5] G.E. Jellison Jr., V.I. Merkulov, A.A. Puretzky, D.B. Geohegan, G. Eras, D.H. Lowndes, J.B. Caughman, Thin Solid Films, 377 – 378 (2000) 68.

[6] J. Tauc, *Optical Properties of Solids*, p. 123, Plenum, New York (1969).

Dedicated to:

Pi

Baby Elephant Walk

and

The Fool